miRNAs detection for non-small cell lung cancer diagnosis

Bernardo Ferreira Pires Teixeira

Dissertação para obtenção do Grau de Mestre em
Biotecnologia
(2º ciclo de estudos)

Orientadora: Prof. Doutora Carla Cruz

outubro de 2021

“A pack achievement, because I never was alone”

To my mom Beatriz.

Acknowledgements

Ao iniciar a escrita desta secção, ocorrem-me quase de forma instantânea inúmeras lembranças dos meus primeiros dias de universidade. Uma experiência única que acima de todas as memórias e momentos que proporcionou, me deu a oportunidade de me cruzar com inúmeras pessoas incríveis que tornaram esta jornada realmente memorável. A entrega da minha dissertação de mestrado marca a chegada a uma meta que não conseguiria alcançar sozinho.

O meu primeiro agradecimento é direcionado à minha orientadora, a professora Carla Cruz. Foi durante a licenciatura que comecei a trabalhar com a professora, no entanto não esperava vir a ter a oportunidade de fazer parte de um projeto tão inovador, que para além de me ter permitido aprender mais em áreas científicas do meu interesse, levou-me a crescer imenso a nível pessoal. Muito obrigado por ter aceitado orientar-me, pela confiança, mas cima de tudo por toda a ajuda durante este último ano.

O próximo agradecimento é feito à pessoa que esteve lá sempre e me acompanhou durante este trabalho, que ensinou "às minhas mãos" como fazer investigação e guiou os meus primeiros passos no laboratório, mas que sobretudo tornou-se numa pessoa enorme que tive a chance de conhecer. O nome desta pessoa é Daniela, e sem ela não teria chegado até aqui. Obrigado Dani por tornares isto possível.

*Um agradecimento também a todos os meus colegas de laboratório que me ajudaram ao longo deste percurso. Obrigado pela disponibilidade que sempre tiveram, e por todo o conhecimento que me transmitiram. Levo amigos com os quais sei que posso contar.

Um muito obrigado a todos os meus amigos que me foram acompanhando até hoje. Felizmente tenho a sorte de ter a meu lado pessoas incríveis que representam um pilar importantíssimo na minha vida. Um obrigado também à minha família, em especial ao meu tio Basílio por todo o apoio dado ao longo deste percurso, e à minha prima Lota por toda a ajuda, suporte, e por me ter sempre impulsionado a descobrir mais sobre o que este mundo tem para oferecer.

Finalmente, o meu maior agradecimento, o meu maior obrigado, é para a pessoa que me trouxe ao mundo e a quem eu também dedico esta dissertação, a minha **mãe**. Na verdade, se eu estou aqui foi por ti, porque sempre deste o teu melhor para que eu conseguisse. Hoje consegui, e sei após esta etapa o futuro só vai ser melhor. Obrigado mãe, por tudo.

Resumo

O cancro do pulmão é considerado um dos mais severos e prevalentes a nível mundial. Em 2020 foi responsável por cerca de dois milhões de novos casos, assim como teve a mais elevada taxa de mortalidade. O cancro do pulmão de não-pequenas células (CPNPC) é o subtipo de cancro do pulmão mais comum, sendo geralmente diagnosticado em estadios avançados. A procura por novas metodologias para o diagnóstico do CPNPC que possam reforçar os procedimentos já praticados é crucial para um diagnóstico precoce e caraterização mais precisa do cancro. Recentemente, novos biomarcadores moleculares estão a surgir como potenciais alvos para o diagnóstico precoce e não-invasivo do CPNPC, nos quais se enquadram múltiplos microRNAs (miRNAs) com expressão alterada. Adicionalmente, o perfil de expressão de miRNAs em plasma e células mononucleares do sangue periférico está conectado com o diagnóstico e estadio do CPNPC. Sondas moleculares são sequências de oligonucleótidos com uma configuração estrutural em stem-loop que lhes permite detetar sequências específicas de ácidos nucleicos através de um sinal fluorescente. O trabalho apresentado estudou o desenvolvimento de uma abordagem *in situ* baseada em sondas moleculares para a deteção de miRNAs em amostras biológicas para o diagnóstico do CPNPC.

O perfil de expressão de miRNAs foi analisado em células mononucleares do sangue periférico através da técnica de RT-qPCR, e posteriormente foram desenhadas sondas moleculares direcionadas para os miRNAs selecionados. Os resultados obtidos mostraram um perfil sob expresso para o microRNA 21-3p (miR-21-3p), miR-21-5p, miR-155-3p e miR-3662 em células mononucleares do sangue periférico de CPNPC, nas quais o miR-92b-5p, miR-150-3p, miR-155-3p e o miR-181a-5p apresentaram uma expressão reduzida relativamente aos controlos. Consequentemente, uma abordagem *in situ* envolvendo sondas moleculares foi desenvolvida, a qual mostrou potencial para a deteção do miR-21 em RNA total de células mononucleares do sangue periférico para o diagnóstico de CPNPC.

Palavras-chave

Cancro do pulmão de não-pequenas células;diagnóstico;microRNAs;células mononucleares do sangue perifério;sondas moleculares;deteção *in situ*

Resumo alargado

O cancro do pulmão é considerado um dos mais severos e prevalentes a nível mundial. Em 2020 foi responsável por cerca de dois milhões de novos casos, assim como apresentou elevadas taxas de mortalidade. O CPNPC é o subtipo de cancro do pulmão mais comum, sendo geralmente diagnosticado em estadios avançados. O diagnóstico precoce do CPNPC está associado a um melhor prognóstico e maiores hipóteses de sobrevivência. As metodologias atuais para o seu diagnóstico apresentam fraca sensibilidade e especificidade, assim como em muitos dos casos geram falsos negativos e positivos. Ademais, os métodos mais precisos para o diagnóstico do CPNPC incluem procedimentos invasivos e por vezes perigosos para os pacientes, tal como biópsias. A procura por novas metodologias para o diagnóstico do CPNPC que possam reforçar os procedimentos já praticados é crucial para um diagnóstico precoce e caraterização mais precisa do cancro.

Recentemente, novos biomarcadores moleculares estão a surgir como potenciais alvos para o diagnóstico precoce e não-invasivo do CPNPC, nos quais se enquadram múltiplos miRNAs com expressão alterada. Adicionalmente, o perfil de expressão de miRNAs em plasma e células mononucleares do sangue periférico está conectado com o diagnóstico e estadio do CPNPC. Sondas moleculares são sequências de oligonucleótidos com uma configuração estrutural em stem-loop que lhes permite detetar sequências específicas de ácidos nucleicos através de um sinal fluorescente. O trabalho apresentado estudou o desenvolvimento de uma abordagem *in situ* baseada em sondas moleculares para a deteção de miRNAs em amostras biológicas para o diagnóstico do CPNPC.

Inicialmente, foram isolados plasma e células mononucleares do sangue periférico de amostras de sangue de doentes de CPNPC e indivíduos saudáveis. O perfil de expressão de miRNAs foi analisado em células mononucleares do sangue periférico através da técnica de RT-qPCR, e posteriormente foram desenhadas sondas moleculares direcionadas para os miRNAs selecionados. Os resultados obtidos mostraram um perfil sob expresso para o miR-21-3p, miR-21-5p, miR-155-3p e miR-3662 em células mononucleares do sangue periférico de CPNPC, nas quais o miR-92b-5p, miR-150-3p, miR-155-3p e o miR-181a-5p apresentaram uma expressão reduzida relativamente aos controlos.

Três sondas moleculares (MB1, MB2 e MB3 21-3p) foram desenhadas e caraterizadas para a deteção do miR-21-3p. Ensaios de interação entre as sondas moleculares e a sequência sintética relativa ao miR-21-3p demonstraram que estas sondas não tinham capacidade de hibridizar com o miR-21-3p. Esta inaptidão resulta de uma correspondência dos nucleótidos da região loop entre si, na qual se encontra a sequência complementar ao miR-21-3p. O acoplamento de nucleótidos da região loop dá origem a uma stem com cerca de 13 pares, resultando numa sonda com uma estrutura altamente estável, inviabilizando a hibridização com o alvo. Posteriormente, foi desenhada a sonda (MB1 21-5p) para a deteção do miR-21-5p. Esta sonda mostrou capacidade para hibridizar com o miR-21-5p, emitindo um sinal fluorescente proporcional à presença deste. Nesta sonda molecular, a região loop encontra-se aberta e permite a hibridização com o miR-21-5p correspondente. Posteriormente, uma abordagem *in situ* envolvendo a deteção do miR-21-5p em células mononucleares do sangue periférico recorrendo à sonda MB1 21-5p foi desenvolvida e otimizada.

Os resultados demonstraram o potencial da sonda MB1 21-5p para a deteção do miR-21-5p em RNA total de células mononucleares do sangue periférico para o diagnóstico do CPNPC.

Abstract

Lung cancer is one of the most severe and prevalent cancers worldwide. Last year, it was responsible for around two million new cases, and represented the leading cancer regarding mortality. Lung cancer subtype non-small cell lung cancer (NSCLC) constitutes the majority of total lung cancer cases, getting generally diagnosed in advanced stages. Current NSCLC diagnosis approaches lack of sensitivity and specificity. Moreover, most accurate NSCLC diagnosis comprises risky patient-invasive procedures like biopsies. The forward-looking demand for new innovative NSCLC diagnosis approaches that could reinforce ongoing procedures is crucial for an even more precise NSCLC staging and early diagnosis.

Recently, new molecular biomarkers are emerging as potential non-invasive diagnostic agents for early-stage NSCLC screening, including multiple miRNAs that display an unusual expression profile in NSCLC. Furthermore, plasma and peripheral blood mononuclear cells (PBMCs) miRNA profile could relate to NSCLC diagnosis. Molecular beacons (MBs) are oligonucleotide probes with a stem-loop structural configuration capable of detect specific nucleic acid sequences throughout fluorescence. The following work studied the development of an *in situ* MB-based strategy for miRNA detection in NSCLC biological samples.

Initially, plasma and PBMCs were isolated from whole blood samples from NSCLC and healthy individuals. miRNA expression profile was screened in PBMCs by RT-qPCR analysis, and further MBs were designed targeting selected miRNAs. Obtained results revealed an up-regulated expression of miR-21-3p, miR-21-5p, miR-155-3p and miR-3662 in NSCLC PBMCs, whereas levels of miR-92b-5p, miR-150-3p, miR-155-5p and miR-181a-5p were reduced. Therefore, an *in situ* method involving miR-21 detection in PBMCs via MBs was shaped and optimized. Accomplished results demonstrated the developed MB approach potential towards miR-21 detection in PBMCs for NSCLC diagnosis.

Keywords

Non-small cell lung cancer, diagnosis, microRNAs, peripheral blood mononuclear cells, molecular beacons, *in situ* detection.

Index

CHAPTER 1 - Introduction 1
1. Introduction 2
1.1 The Lungs 2
  1.1.1 Lung anatomy and function 2
  1.1.2 Pulmonary diseases 4
  1.1.3 Lung cancer 6
1.2 NSCLC Diagnosis 8
  1.2.1 Current diagnosis and limitations 8
  1.2.2 New approaches 9
1.3 MicroRNAs (miRNAs) 10
  1.3.1 Pri, pre and mature miRNAs 10
  1.3.2 miRNAs in NSCLC 11
  1.3.3 NSCLC miRNAs in study 13
  1.3.4 miRNA profiling 15
1.4 Molecular Beacons 17
  1.4.1 Structure and features 17
  1.4.2 Applications 18
1.5 Biophysical characterization 18
  1.5.1 Förster resonance energy transfer (FRET) 18
  1.5.2 Circular dichroism (CD) 20
  1.5.3 Nuclear magnetic resonance (NMR) 20
  1.5.4 Fluorescence spectroscopy 21
1.6 *In situ* MB miRNA detection 21
  1.6.1 MB hybridization assays 21
  1.6.2 Condition screening and biological samples 22
CHAPTER 2 – Aims of Work 25
2. Aims of Work 26
CHAPTER 3 – Materials and Methods 27
3. Materials and Methods 28
3.1 Materials 28
3.2 Methods 29
  3.2.1 miRNA profiling in NSCLC samples 29
    3.2.1.1 Human blood sample collection 29
    3.2.1.2 Plasma isolation 30

3.2.1.3 PBMCs and cell lines isolation 30
3.2.1.4 Total RNA extraction and quantification 31
3.2.1.5 Agarose gel electrophoresis 32
3.2.1.6 Reverse transcriptase quantitative PCR (RT-qPCR) 32
3.2.2 MB characterization and interaction studies 34
3.2.2.1 MB design 34
3.2.2.2 Synthetic sequences preparation 35
3.2.2.3 FRET-melting experiments 35
3.2.2.4 CD Spectroscopy 36
3.2.2.5 NMR Spectroscopy 36
3.2.2.6 SDS-PAGE electrophoresis 37
3.2.2.7 Fluorescence assays 37
3.2.3 Statistical analysis 38
CHAPTER 4 – Results and Discussion 39
4. Results and Discussion 40
4.1 Biological samples processing 40
4.1.1 NSCLC and healthy population 40
4.1.2 Plasma hemolysis 41
4.1.3 PBMC count 42
4.2 NSCLC miRNA profiling 43
4.2.1 RNA yield and quality 43
4.2.2 RT-qPCR 46
4.2.3 Clinical analysis 55
4.3 Designed MB dynamics 58
4.4 MB1 21-3p study 60
4.4.1 Biophysical characterization 60
4.4.1.1 FRET / Reverse FRET melting 61
4.4.1.2 Circular dichroism (CD) 62
4.4.1.3 Nuclear magnetic resonance (NMR) 64
4.4.2 Interaction studies 65
4.4.2.1 MB1 21-3p hybridization assays optimization 65
4.4.2.2 FRET / Reverse FRET melting 69
4.4.2.3 SDS-PAGE electrophoresis 70
4.4.2.4 *In situ* MB1 21-3p - miRNA detection 71
4.5 MB2 and MB3 21-3p study 74
4.5.1 Biophysical characterization 75
4.5.1.1 FRET / Reverse FRET melting 75

4.5.1.2 Circular dichroism (CD) 77
4.5.2 Interaction studies 78
4.5.2.1 MB2 / MB3 21-3p hybridization assays optimization 78
4.5.2.2 Fluorometric assays 79
4.5.2.3 *In situ* MB2 / MB3 21-3p - miRNA detection 80
4.6 MB1 21-5p study 83
4.6.1 Biophysical characterization 83
4.6.1.1 FRET / Reverse FRET melting 83
4.6.1.2 Circular dichroism (CD) 85
4.6.1.3 Nuclear magnetic resonance (NMR) 86
4.6.2 Interaction studies 87
4.6.2.1 MB1 21-5p hybridization assays optimization 88
4.6.2.2 FRET / Reverse FRET melting 89
4.6.2.3 SDS-PAGE electrophoresis 93
4.6.2.4 NMR spectroscopy 94
4.6.2.5 MB1 21-5p hybridization enhancement 95
4.6.2.6 *In situ* MB1 21-5p - miRNA detection 97
CHAPTER 5 – Conclusions and Future Perspectives 102
5. Conclusions and Future Perspectives 103
CHAPTER 6 – References 105
6. References 106
CHAPTER 7 – Attachments 132
7. Attachments 133
7.1 Attachment 1 - CHUCB Ethics Committee approval for study (ref. 35/2019) to blood sample collection 133
7.2 Attachment 2 - XVI Annual CICS-UBI Symposium 2021 (Short communication) 135

List of Figures

Figure 1. Lung anatomy diagram. A) Conducting zone of the tracheobronchial tree starting at the trachea and ending at the terminal bronchioles. B) Terminal bronchiole and alveoli. Adapted from [8]. 3

Figure 2. Representation of the pulmonary gas exchange process at the alveoli where occurs O_2 and CO_2 diffusion. Taken from [16]. 4

Figure 3. Different lung-related conditions are responsible for several deaths worldwide. COPD and asthma are the most common respiratory diseases. Adapted from [33]. 5

Figure 4. Lung cancer stages. Lung cancer progression lead to tumor increase and metastasis. Created and modified on [53]. 7

Figure 5. miRNAs biogenesis. miRNA genes are transcribed by RNA polymerase II into pri-miRNAs, that are cleaved and generate pre-miRNAs. Mature miRNA sequences result from pre-miRNAs processing by Dicer. Adapted from [117]. 11

Figure 6. miRNA expression dysregulation interplay in NSCLC development and progression. Created and modified from [53]. 12

Figure 7. PCR sequence amplification steps. 1) Denaturation; 2) Annealing; 3) Elongation. Created and modified from [53]. 16

Figure 8. MB representation in the folded stem-loop configuration, and further hybridized with a specific miRNA target. 18

Figure 9. FRET phenomenon representation. At the folded structure no fluorescence is emitted because of FRET. Upon hybridization, FRET phenomenon no longer exists and fluorescence is emitted by fluorophore. Adapted from [203]. 19

Figure 10. MB-miRNA in situ detection approach representation. MB and specific miRNA are placed in a microplate for fluorescence measurement. Higher fluorescence values are proportional to miRNA concentration. 23

Figure 11. Graphical abstract comprising biological samples processing at task 1, miRNA profiling in task 2, MB design and biophysical characterization in task 3, and the miRNA detection via MB in task 4. 24

Figure 12. Predictive base-pairing configuration of designed MBs. **A)** MB for miR-21-3p and **B)** MB for miR-21-5p detection. 34

Figure 13. Statistical schematic on NSCLC and healthy control testing groups of the study. 41

Figure 14. Plasma hemolysis. A) Visual aspect of a non-hemolyzed and a hemolyzed plasma sample. B) Plasma hemolysis measurement results. 41

Figure 15. PBMC count among NSCLC and healthy groups collected samples. Almost every sample had the minimum PBMC number for further RNA extraction. 42

Figure 16. PBMCs and A549 extracted RNA quality. A) Characteristic electrophoresis gel of rRNA 28S/18 profile for extracted RNA from A549 cell line, NSCLC, and control PBMCs, before NSCLC sample collection modifications. B) Characteristic electrophoresis gel rRNA of rRNA 28S/18 profile for extracted RNA from A549 cell line, NSCLC, and control PBMCs after NSCLC sample collection modifications. 45

Figure 17. miRNA selected-panel relative expression in A549 versus NHDF cell line. Housekeeping gene normalization was not applied to cell line qPCR data. A549 miRNA expression values were determined from qPCR assays duplicate measurements, and standardized relativly to NHDF a control expression value 1 (mean ± SE, n=2). 48

Figure 18. Selected-miRNA relative expression in NSCLC and healthy control PBMCs. Data were normalized to housekeeping miRNAs 103a-3p and 191-5p, and further NSCLC miRNA expression calculated relatively to a healthy control expression value of 1 (mean ± SE. *P<0.05). Data population after outliers exclusion for the multiple miRNAs was: 21-3p (control n=11, NSCLC n=20); miR-21-5p (control n=18, NSCLC n=44); miR-92b-5p (control n=12, NSCLC n=23); miR-150-3p (control n=19, NSCLC n=46); miR-155-3p (control n=10, NSCLC n=23); miR-155-5p (control n=10, NSCLC n=21); miR-181a-5p (control n=11, NSCLC n=16); miR-3662 (control n=8, NSCLC n=14). 50

Figure 19. ROC curve analysis on miR-21 RT-qPCR profiling in healthy and NSCLC PBMCs. A) miR-21-3p ROC curve. B) miR-21-5p ROC curve. 51

Figure 20. ROC curve analysis on miRNAs 92b-5p and 150-3p RT-qPCR profiling in healthy and NSCLC PBMCs. A) miR-92b-5p ROC curve. B) miR-150-3p ROC curve. 52

Figure 21. ROC curve analysis on miR-155 RT-qPCR profiling in healthy and NSCLC PBMCs. A) miR-155-3p ROC curve. B) miR-155-5p ROC curve...53

Figure 22. ROC curve analysis on miRNAs 181a-5p and 3662 RT-qPCR profiling in healthy and NSCLC PBMCs. A) miR-181a-5p ROC curve. B) miR-3662 ROC curve.......................54

Figure 23. PBMC miR-21-3p expression among NSCLC stage. IA (n=1); IIB (n=1); IIIA (n=2); IIIB (n=3); IIIC (n=1); IV (n=7); IVA (n=5); IVB (n=3). RT-qPCR data is displayed in fold change (± SE)...55

Figure 24. PBMC miR-21-3p expression among NSCLC mutations and smoking record. A) miR-21-3p expression versus NSCLC mutations. Negative (n=6); EGFR (n=5); ALK (n=3); BRAF (n=2); MET (n=1); RET (n=1). B) miR-21-3p expression versus smoking background. Ex-smoker (n=6); No (n=8); Yes (n=7). RT-qPCR data is displayed in fold change (± SE). .56

Figure 25. PBMC miR-21-5p expression among NSCLC stage. IA (n=3); IB (n=1); IIB (n=1); IIIA (n=3); IIIB (n=5); IIIC (n=2); IV (n=8); IVA (n=12); IVB (n=10); IVC (n=1). RT-qPCR data is displayed in fold change (± SE). 57

Figure 26. PBMC miR-21-5p expression among NSCLC mutations and smoking record. A) miR-21-5p expression versus NSCLC mutations. Negative (n=17); EGFR (n=10); ALK (n=4); KRAS (n=2); ROS-1 (n=2), MET (n=1); BRAF (n=1); RET (n=1). B) miR-21-3p expression versus smoking background. Ex-smoker (n=13); No (n=16); Yes (n=13). RT-qPCR data is displayed in fold change (± SE). 57

Figure 27. Designed MBs folding structure with the respective fluorophore and quencher. MB1 21-3p, MB2 21-4p and MB3 21-3p target miR-21-3p. MB1 21-5p target miR-21-5p............59

Figure 28. MB1 21-3p design and structure with corresponding fluorophore and quencher. Structure image represent MB1 21-3p fold configuration. 60

Figure 29. MB1 21-3p FRET curves and T_m. A) MB1 21-3p FRET melting in 1× PBS. B) MB1 21-3p FRET melting in lithium cacodylate...61

Figure 30. FRET and reverse FRET melting curves of MB1 21-3p. Fluorescence was monitored from 25ºC to 95ºC, returning to 25ºC in reverse FRET melting. 62

Figure 31. MB1 21-3p CD spectra in PBS and lithium cacodylate. CD spectra measurements were obtained at 20ºC in a 200-320 nm range within 4 accumulations. 63

Figure 32. MB1 21-5p NMR spectra with temperature variation. Displayed spectra only comprises the stem region where the MB specific signals are present. 64

Figure 33. MB1 21-3p fluorescence hybridization temperature screening results obtained in Plate reader 2. Displayed data correspond to raw fluorescence values of a single assay (n=1). 66

Figure 34. MB1 21-3p fluorescence hybridization temperature and reading time screening results obtained in plate reader 1. Presented data result from MB + miRNA (with MB 21-3p basal fluorescence subtracted) means fluorescence values of 5 separate assays (n=5). 67

Figure 35. MB1 21-3p incubation time and temperature optimization towards maximum hybridization efficiency. First column represents achieved MB1 21-3p better conditions. Following columns represent condition variation according to MB hybridization studies. Fluorescence data got MB 21-3p basal fluorescence subtracted and was measured in Plate reader 1 (n=1). 68

Figure 36. MB1 21-3p with miR-21-3p (0.2, 0.4 and 0.8 μM) FRET and reverse FRET melting curves. 69

Figure 37. MB1 21-3p hybridization SDS-PAGE electrophoresis gel results. M: Weight marker; A: 25ºC incubation sample set; B: 40ºC incubation sample set; C: 60ºC incubation sample set; 1: miR-21-3p (10 μM); 2: MB1 21-3p (10 μM); 3: MB1 21-3p (10 μM) + miR-21-3p (10 μM); 4: MB1 21-3p (10 μM) + miR-21-3p (20 μM). 70

Figure 38. MB1 21-3p NSCLC and control PBMC total RNA hybridization assay. Fluorescence data was measured in Plate reader 1 and is represented as total fluorescence mean results from tested control (n=3) and NSCLC (n=5) groups (± SE). 72

Figure 39. MB1 21-3p RT-qPCR product hybridization assays. A) Total fluorescence results were acquired in Plate reader 1 within control (n=5) and NSCLC (n=8) RT-qPCR products (± SE). B) Total fluorescence results were acquired in Plate reader 2 comprising a RT-qPCR no template control (NTC), healthy control (n=2) and NSCLC (n=3) RT-qPCR products (± SE). 73

Figure 40. MB2 21-3p and MB3 21-3p design and structure with corresponding fluorophore and quencher. Structure image represent MB2 and MB3 21-3p fold configuration. 75

Figure 41. FRET and reverse FRET melting curves of MB2 and MB3 21-3p. A) FRET and reverse FRET melting results for MB2 21-3p. B) FRET and reverse FRET melting results for MB3 21-3p. Fluorescence was monitored from 25ºC to 95ºC, returning to 25ºC in reverse FRET melting. 76

Figure 42. MB2 and MB3 21-3p CD spectra. A) CD spectra of MB2 21-3p in PBS. B) CD spectra of MB3 21-3p in PBS. CD spectra measurements were obtained at 20ºC in a 200-320 nm range within 4 accumulations. 77

Figure 43. MB2 and MB3 21-3p hybridization temperature screening assays. Fluorescence data was aquired in Plate reader 1 and got respective MB2 and MB3 21-3p basal fluorescence discounted (n=3). 78

Figure 44. Fluorometric MB2 21-3p single and with synthetic miR-21-3p results. Both assays fluorescence was monitored from 25ºC to 90ºC at the correspondent HEX excitation and emission wavelengths, and further normalized. 79

Figure 45. MB2 and MB3 hybridization assays with RT-qPCR products. Fluorescence data was measured in Plate reader 1 and is represented in total values regarding MB2 and MB3 21-3p hybridization with two miR-21-3p representative RT-qPCR products (n=2). 81

Figure 46. MB2 21-3p NHDF and A549 RT-qPCR products hybridization assays. MB: MB2 21-3p; miR-21-3p: MB2 21-3p + synthetic miR-21-3p; NHDF: MB2 21-3p + NHDF RT-qPCR product; A549: MB2 21-3p + A549 RT-qPCR product (n=1). A) Total fluorescence results were acquired in Plate reader 1. B) Total fluorescence results were acquired in Plate reader 2. 81

Figure 47. MB1 21-5p design and structure with corresponding fluorophore and quencher. Structure image represent MB1 21-5p fold configuration. 83

Figure 48. MB1 21-5p FRET curves and T_m. A) MB1 21-5p FRET melting in 1×PBS. B) MB1 21-5p FRET melting in lithium cacodylate. 84

Figure 49. FRET and reverse FRET melting curves of MB1 21-5p. Fluorescence was monitored from 25ºC to 95ºC, returning to 25ºC in reverse FRET melting. 85

Figure 50. MB1 21-5p CD spectra in PBS. CD spectra measurements were obtained at 20ºC in a 200-320 nm range within 4 accumulations. 86

Figure 51. MB1 21-5p NMR spectra with temperature variation. Displayed spectra only comprises the stem region where the MB specific signals are present. 87

Figure 52. MB1 21-5p hybridization temperature screening assays. A) MB1 21-5p fluorescence reading in Plate reader 1. B) MB1 21-5p fluorescence reading in Plate reader 2. Fluorescence data got MB1 21-5p basal fluorescence discounted (n=1). 88

Figure 53. MB1 21-5p hybridization with miR-21-5p and non-specific miR-21-3p. Fluorescence is represented in total values measured in Plate reader 1, regarding MB: MB1 21-5p basal fluorescence, MB1 21-5p + miR-21-3p and MB1 21-5p + miR-21-5p (n=1). 89

Figure 54. MB1 21-5p with miR-21-5p (0.2 and 0.4 μM) FRET and reverse FRET melting results. A) MB1 21-5p FRET melting curve with miR-21-5p. B) MB1 21-5p reverse FRET melting curve with miR-21-5p. Fluorescence was monitored from 25ºC to 95ºC, returning to 25ºC in reverse FRET melting. 90

Figure 55. FRET and reverse FRET melting curves for MB1 21-5p with miR-21-5p (0.2 μM) and a non-specific miR-21-3p (0.2 μM) target. 91

Figure 56. MB1 21-5p hybridization SDS-PAGE electrophoresis gel results. M: Weight marker; A: 25ºC incubation sample set; B: 40ºC incubation sample set; C: 60ºC incubation sample set; 1: miR-21-5p (10 μM); 2: MB1 21-5p (10 μM); 3: MB1 21-5p (10 μM) + miR-21-5p (10 μM); 4: MB1 21-5p (10 μM) + miR-21-5p (20 μM). 93

Figure 57. MB1 21-5p NMR spectra with miR-21-5p. Spectra acquisition was performed at 40ºC with single MB1 21-5p, and with MB + 1.5 and 2 equivalents of miR-21-5p. Displayed spectra only comprises the stem-loop region where the MB specific signals are present. 95

Figure 58. MB1 21-5p hybridization optimization assays. A) MB1 21-5p fluorescence data over temperature variation. B) MB1 21-5p fluorescence data over time after reaching 45ºC. MB1 21-5p basal fluorescence values were deducted from presented fluorescence data measured in Plate reader 1. 96

Figure 59. MB1 21-5p control and NSCLC RT-qPCR products hybridization assays. MB: MB1 21-5p; NTC: MB1 21-5p + NTC RT-qPCR product; Control: MB1 21-5p + control RT-qPCR product (n=9); NSCLC: MB1 21-5p + NSCLC RT-qPCR product (n=15). Total fluorescence results were aquired in Plate reader 2 (± SE). 97

Figure 60. MB1 21-5p hybridization assays at different NHDF RNA concentrations. Fluorescence data is represented as total fluorescence measured values in the Plate reader 2 (n=1). 98

Figure 61. MB1 21-5p NHDF and A549 RNA hybridization assays. Fluorescence data is represented as total fluorescence measured values in Plate reader 1 (n=3, ± SE). 99

Figure 62. MB1 21-5p hybridization assays with RNA from NSCLC and healthy control PBMCs. Fluorescence levels were measured in the Plate reader 1, further got MB1 21-5p basal fluorescence deducted, and were normalized to 1. Samples in study comprised: healthy control group (n=9); NSCLC group (n=19). 100

List of Tables

Table 1. miRCURY LNA miRNA PCR assay primers for RT-qPCR miRNA screening...... 28

Table 2. MB and miRNA oligonucleotide synthetic sequences 29

Table 3. NSCLC and healthy control testing groups of the study 40

Table 4. Average RNA extraction results in plasma, PBMCs, and A549 / NHDF cell lines. 44

Table 5. RT-qPCR non-normalized mean miRNA amplification values in NHDF and A549 cell lines 48

Table 6. RT-qPCR mean miRNA amplification values in control and NSCLC groups......... 49

Table 7. MBs T_m and ΔG software predictions... 59

List of Acronyms

$A_{260/230}$	Absorbance ratio at 260 and 230 nm
$A_{260/280}$	Absorbance ratio at 260 and 280 nm
A549	Adenocarcinomic human alveolar basal epithelial cells
AGO	Argonaute protein
AKT	Protein kinase B
ALK	Anaplastic lymphoma kinase
AUC	Area under the curve
b-Myb	MYB proto-oncogene
Bcl-2	B-cell lymphoma 2
BHQ1	Black-hole quencher 1
BHQ2	Black-hole quencher 2
BRAF	B-Raf proto-oncogene
c-Myc	MYC proto-oncogene
CD	Circular dichroism
CDK1	Cyclin-dependent kinase 1
cDNA	Complementary DNA
CHUCB	Centro Hospitalar Cova da Beira
CO_2	Carbon dioxide
COPD	Chronic obstructive pulmonary disease
COVID-19	Coronavirus disease 2019
CPNPC	Cancro do pulmão de não-pequenas células
CT	Computed tomography
Ct	Cycle threshold
D_2O	Heavy water
dabcyl	4-(dimethylaminoazo) benzene-4-carboxylic acid
DEPC	Diethyl pyrocarbonate
DGCR8	DiGeorge syndrome critical region gene 8
DICER	RNase II endonuclease Dicer
DNA	Deoxyribonucleic acid
dNTPs	Deoxyribonucleotide triphosphates
DROSHA	Double-stranded RNA-specific endoribonuclease
EDTA	Ethylenediaminetetraacetic acid
EGFR	Epidermal growth factor receptor
ELM4	Echinoderm microtubule-associated protein-like 4
FAM	Fluorescien
FOXO1	Forkhead box protein O1
FOXO4	Forkhead box protein O4
FRET	Förster resonance energy transfer
G4	G-quadruplex
GC	Guanine-cytosine
GTP	Guanosine triphosphate
HCC827	Cellosaurus cell line HCC827
HEX	Hexachloro-fluorescein
HK2	Hexokinase 2

HMGA2	AT-hook 2
HPLC	High performance liquid chromatography
KRAS	Kirsten rat sarcoma virus
LNA	Locked nucleic acid
LRIs	Lower respiratory tract infections
M	Metastasis
MAB	Molecular aptamer beacon
MALDI-TOF	Matrix-assisted laser desorption ionization
MAPK	Mitogen-activated protein kinase
MB	Molecular beacon
miR	microRNA
miRNA	microRNA
MRI	Magnetic resonance imaging
mRNA	Messenger RNA
N	Node
ncRNA	Non-coding RNA
NF-kB	Nuclear factor kappa-light-chain-enhancer of activated B cells
NHDF	Normal human dermal fibroblasts
NMR	Nuclear magnetic resonance
NSCLC	Non-small cell lung cancer
NTC	Non-template control
O_2	Oxygen
onco-miR	Oncogenic microRNA
P53	Tumor protein 53
PBMC	Peripheral blood mononuclear cell
PBS	Phosphate-buffered saline
PDCD4	Programmed cell death 4
PET	Position emission tomography
PI3k	Phosphoinositide 3-kinase
pre-miRNA	Percursor miRNA
pri-miRNA	Primary miRNA
PTEN	Phosphatase and tensin homolog
RanGTP	GTP-binding nuclear protein Ran
RBC	Red blood cell
RECK	Reversion-inducing-cysteine-rich protein
RF	Radiofrequency
RISC	RNA-induced silencing complex
RNA	Ribonucleic acid
ROC	Receiver operating characteristic
ROS	Reactive oxygen species
rpm	Rotations per minute
rRNA	Ribosomal RNA
RT-qPCR	Reverse transcriptase quantitative polymerase chain reaction
SARS-CoV-2	Severe acute respiratory syndrome coronavirus 2
SCLC	Small cell lung cancer
SDS-PAGE	Sodium dodecyl sulphate-polyacrylamide gel electrophoresis
SIRT2	Sirtuin 2
SOCS1	Suppressor of cytokine signaling 1
SOCS6	Suppressor of cytokine signaling 6

STK	Serine/threonine protein kinase
T	Tumor
TAMRA	Tetramethylrhodamine
TKI	Tyrosine kinase inhibitor
T_m	Melting temperature
TNM	Classification of Malignant Tumors
TSG	Tumor suppressor gene
URIs	Upper respiratory tract infections
UV	Ultraviolet

List of Publications

Accepted manuscripts

1) Figueiredo, J. ; Santos, T. ; Miranda, A. ; Alexandre, D. ; Teixeira, B. ; Simões, P. ; Lopes-Nunes, J. ; Cruz, C. “Ligands as Stabilizers of G-Quadruplexes in Non-Coding RNAs”, *Molecules* **2021**, 26.

Conferences presentations

1) Teixeira, B. ; Alexandre, D. ; Rico, A. ; Cruz, C. “miRNAs detection for non-small cell lung cancer diagnosis”. XVI Annual CICS-UBI Symposium (30/09/2021).

CHAPTER 1 - Introduction

1. Introduction

Chapter 1 - Introduction provides fundamental knowledge and multiple theoretical concepts from literature revision on the current state of art. Essential understanding of key subjects encompasses lung cancer, particularly non-small-cell lung cancer (NSCLC), actual diagnosis strategies and promising research findings.

The developed work consists of an avant-garde method for NSCLC diagnosis, relying on NSCLC-specific microRNAs (miRNAs), alongside with their detection via molecular beacons (MBs). Information on previous topics, as well as in all applied techniques, is followingly reported.

1.1 The Lungs

1.1.1 Lung anatomy and function

Italian author Giovanni Papini left written, “Breathing is the greatest pleasure in life”, but in fact, this vital process for human beings only happens thanks to the primary organs of the respiratory system, the lungs [1].

Lungs are located around the chest area, inside the thoracic cage. Each people has two lungs, the right lung divided into three lobes (upper, middle and lower), and the left lung formed by two lobes (upper and lower), which is slightly smaller than the right one [2]. Both lungs are coated by the pleura, a combination between the visceral and parietal pleura, two membranes that allow the lung to move dynamically and protect from potential infections. Furthermore, the pleura can accumulate pigments over the years related to exposure to particle pollution [2], [3].

The respiratory tract is responsible for delivering inhaled air to the lungs, and it can be separated into four regions. The naso-oropharynx includes both nose and mouth airways, pharynx and larynx. Moreover, this section is capable of filtering larger particles [4], [5]. The following sector is the conducting airways, starting by the trachea that bifurcates into two main bronchus, which subsequently ramifies across the lung [4]–[6]. The respiratory bronchioles constitute the third part of the respiratory tract that leads to the alveoli. Here, smaller particles are captured and immune cells have activity against pathogens. At last, alveoli receive the air for gas exchanges with the organism through a capillary network [4], [5], [7]. Figure 1 illustrates a detailed diagram of the lung anatomy.

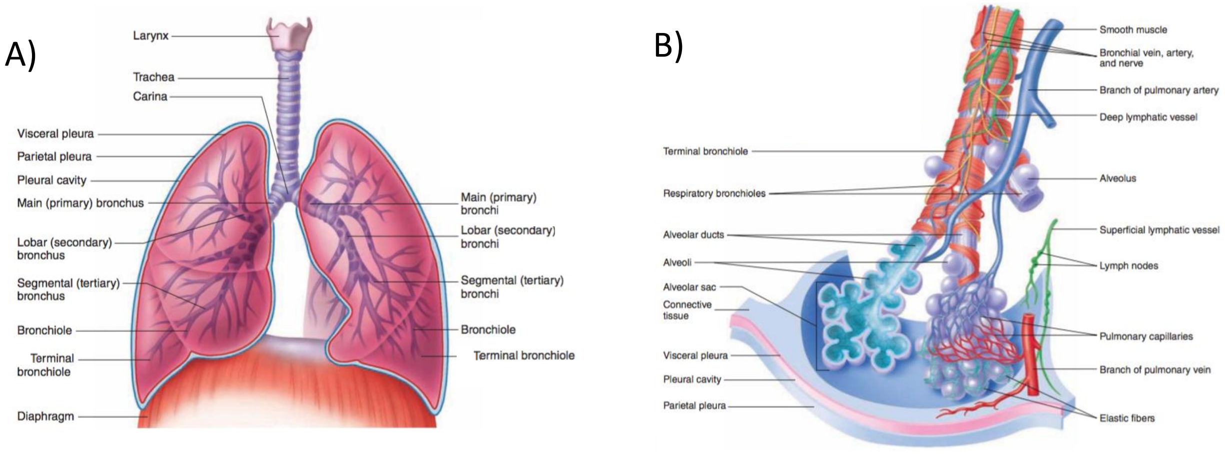

Figure 1. Lung anatomy diagram. A) Conducting zone of the tracheobronchial tree starting at the trachea and ending at the terminal bronchioles. B) Terminal bronchiole and alveoli. Adapted from [8].

Lung epithelium cells influence the respiratory airway and healthy lung performance. Besides representing a physical barrier to several agents, these cells also present particle removal mechanisms and maintain the normal moisture levels [2], [9], [10]. Ciliated cells are found in the bronchus and their rhythmic movement generates an efficient mucociliary clearance of particles and toxicants [2], [11]. Along larger and smaller bronchus are the goblet cells, capable of mucous production through the secretion of mucin to hydrate and protect near tissues [2], [12]. The basal bronchus cells have the potential to differentiate into ciliated or non-ciliated cells from the bronchial mucosa [2], [13]. Clara cells replace the missing goblet cells in the bronchioles. They synthesize and release a mucous material to keep small lung channels open, and additionally, have a restorative function just like basal cells [2], [12]. In the alveoli, there are type I and II epithelial cells. Type I epithelial cells are thin, high permeable to gases, and coat the majority of the alveoli surface. On the other side, type II epithelial cells are most numerous in the alveoli core, presenting secretory units in charge of generating a surfactant that reduces surface tension [2], [7].

The pulmonary gas exchange process occurs in the lungs, more precisely in alveoli. Inhaled air reaches out the alveoli, making them expand and subsequently, increasing the surface area in contact with the capillary network. Alveoli and capillary membranes connection create a respiratory membrane that promotes air diffusion [14]. Deoxygenated blood is supplied to the capillary network, and as soon as it meets the alveoli, oxygen (O_2) and carbon dioxide (CO_2) trades are made among blood and inhaled air through the respiratory membrane. The higher concentration of O_2 in alveoli in comparison with capillary blood develops a partial O_2 pressure difference, which is strong enough to lead to oxygen transfer through blood. Similar differences arise for CO_2. Considering its higher concentration in capillary blood, the formed partial pressure will allow the diffusion of CO_2 over to the alveoli [14], [15]. A schematic on pulmonary gas exchange is displayed in Figure 2.

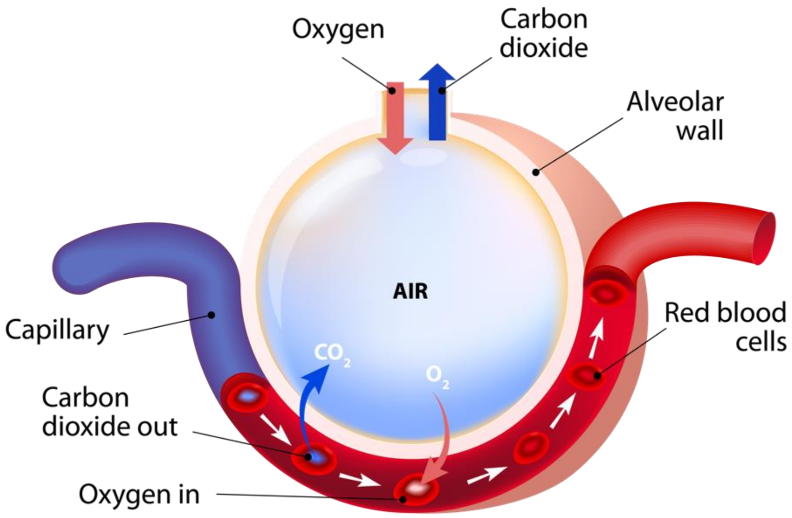

Figure 2. Representation of the pulmonary gas exchange process at the alveoli where occurs O_2 and CO_2 diffusion. Taken from [16].

1.1.2 Pulmonary diseases

Pulmonary diseases have a high impact on society's health worldwide. These conditions affect both organs and tissues from the respiratory tract, bringing difficulties for human breathing activity [17], [18].

Obstructive lung diseases are described as disorders that conduce to airflow obstruction, like chronic obstructive pulmonary disease (COPD), asthma and bronchiectasis [19]. In COPD, exposure to tobacco smoke and air pollution leads to an inflammatory response, resulting in progressive small airways constriction and lung tissue damage [19]–[21]. Asthma is a chronic inflammation in lung airways, where an allergen or a pollutant can trigger a response that brings breathing difficulties for susceptible individuals [19], [22]. Furthermore, environmental factors and genetic components play a role in one of the most common and increasing health conditions in the 21st century [22], [23]. Bronchiectasis refers to a chronic inflammation correlated with permanent dilatation of airways in the bronchial region, and subsequently, adjacent bronchial tissue injury [19], [24].

Restrictive lung diseases assemble a group of pulmonary disorders characterized by lung expansion compromising and lung capacity reduction. Moreover, restrictive lung diseases differ from obstructive ones due to their connection with the loss of lung compliance, and not respiratory tract obstruction [25], [26].

Several infections can affect both the upper and lower respiratory tract. In upper respiratory tract infections (URIs), the pathogen invades the upper airway, leading to a common cold or a more specific area-oriented infection like rhinitis, pharyngitis and laryngitis. Most commonly virus connected to URIs are rhinovirus, influenza virus, adenovirus and enterovirus [27], [28]. On the other hand, lower respiratory tract infections (LRIs) occur in a lower area, below the larynx [29]. Among LRIs, bronchitis concern the inflammation of the bronchi, however in pneumonia, the infection happens in the alveoli [30], [31]. Tuberculosis is an LRI caused by *Mycobacterium tuberculosis* that generally affects the lungs, but it can also spread to other parts of the body [32]. Figure 3 exhibit multiple lung conditions.

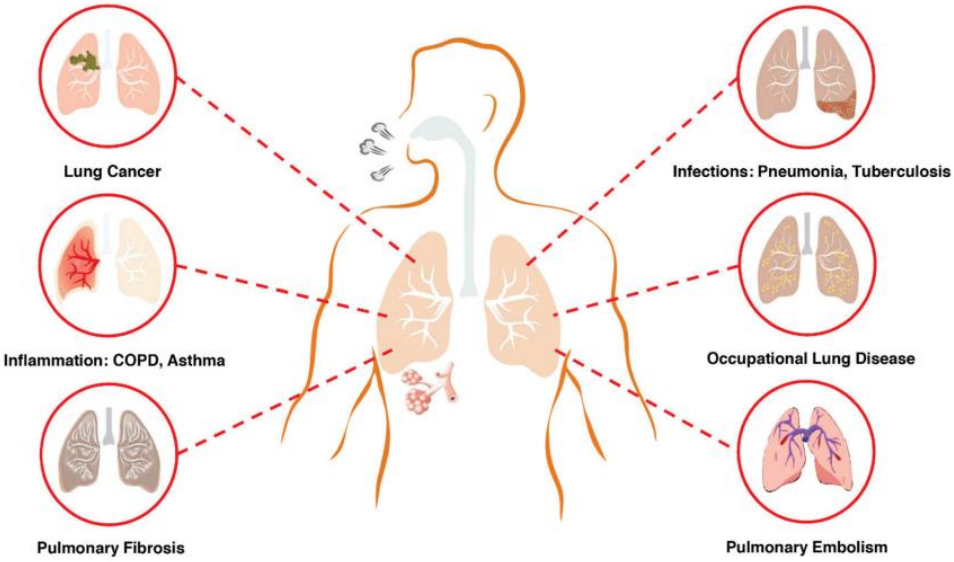

Figure 3. Different lung-related conditions are responsible for several deaths worldwide. COPD and asthma are the most common respiratory diseases. Adapted from [33].

Most recently, the emergence of coronavirus disease 2019 (COVID-19) pandemic caused by the infectious severe acute respiratory syndrome coronavirus 2 (SARS-CoV-2), along with this disease potential to develop symptoms such as fever and some breathing problems, up to pneumonia or even respiratory failure, brought one of the biggest and most difficult challenges that our society and the medical field ever faced [34], [35].

1.1.3 Lung cancer

Earliest abnormal cell growth tumor reports go back to 1600 BC, and since then our world started a long-term battle against what had turned to be a major health problem amongst the global population [36]. In the last three centuries, research efforts from all over the world provided a significant advance in cancer knowledge and new approaches for diagnosis and therapy [37].

According to GLOBOCAN 2020 estimates, cancer prevails as a principal cause of death worldwide, as well as premature death, ranking first and second place in death causes before the age of 70 in 112 countries [38]. Lung cancer presents a high impact on cancer incidence and mortality over the past years, representing in 2020 the second most incident cancer with 2.206.771 million new cases (11.4% total cancer cases), and the leading one in mortality with 1.796.144 million new deaths (18% total cancer deaths) globally, which equals more than two times breast cancer value, the second most deathly cancer with 684.996 new deaths (6.9% total cancer deaths) [38]–[40].

Lung cancer is a malignant tumor in the lungs defined by an unregulated cell growth resulting from anomalies in cell standard functions [41], [42]. This uncontrolled cell growth origin a group of cells designated by tumor, and in case of being malignant, these cells can diffuse over the body through metastasis [43].

Most usual lung cancer symptoms involve cough, weight loss, dyspnea, hemoptysis and chest plus bone pain [44]. Numerous factors can contribute to lung cancer development, considering that the exposure to multiple specific agents, under the name of mutagens or carcinogens, may stimulate the genetic changes behind lung cancer [45]. Smoking is the principal cause of lung cancer, including tobacco, cannabis and vaping [46]–[48]. Natural inhalation of substances from smoking by passive smokers also significantly-increase lung cancer risk [49]. Diet and alcohol consumption, along with radiation, asbestos and air pollution contact, can additionally prompt lung cancer in healthy individuals [50].

Lung cancer staging follows the Classification of Malignant Tumors (TNM) system, where the T stands for tumor, N for node and M for metastasis. Here, each component is classified, depending on cancer progression, into different stages. Stage I designate a surgically removable tumor with no need for chemotherapy or radiotherapy, while stage IV is related to further developed cancers, often metastasized and corresponding to worse prognosis [51]. Early diagnosis of lung cancer is correlated with higher survival rates, as shown by data statistics, the five-year survival rate for stage I is 47%, stage II 30%, stage III 10% and stage IV 1% [52]. Figure 4 illustrates lung cancer stages.

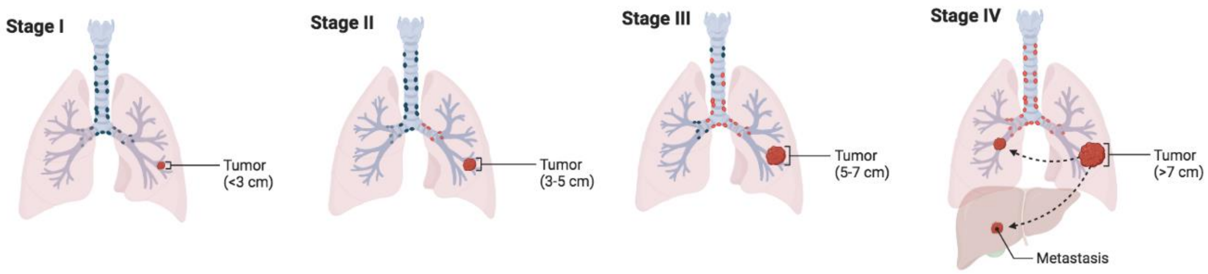

Figure 4. Lung cancer stages. Lung cancer progression lead to tumor increase and metastasis. Created and modified on [53].

Generally, lung cancer is divided into two main types: non-small cell lung cancer (NSCLC) that represents around 75% of the cases, and small cell lung cancer (SCLC) with the remaining 25% [42], [54]. Despite being less predominant, SCLC exhibit a worse prognosis among lung cancer cases, in consequence of a much aggressive profile and early metastization propensity [55]. NSCLC is further distributed in three most common subtypes: adenocarcinoma, squamous cell carcinoma and large cell carcinoma [56]. Adenocarcinoma is the more frequent type of lung cancer, and also the most recurrent in nonsmokers, followed by squamous cell carcinoma which is highly connected with tobacco smoking. Large cell carcinoma represents a smaller fraction of lung cancer cases [57]–[59].

Mutations may occur naturally or be induced via mutagens, triggering genetic modifications responsible for irregularities in cell normal proliferation and apoptosis pathways, which transform normal cells into cancer cells [60]. DNA damage consists of a nucleic acid sequence alteration that can be reverted by DNA natural repair mechanisms. If DNA mismatches undergo further replication, they can create genetic mutations associated with multiple diseases, including cancer [61]–[63]. Gene mutations lead to oncogene activation and tumor suppressor gene (TSG) inactivation, which can have a high influence on cancer growth [64].

Proto-oncogene Kirsten rat sarcoma virus (KRAS) encodes a protein involved in cell proliferation, differentiation and survival mechanisms, which is often mutated in NSCLC, especially among smoking patients [64]–[66]. KRAS mutation is particularly related to superior cancer staging and therapy resistance [67], [68]. Epidermal growth factor receptor (EGFR) alterations are frequent in NSCLC, occurring in about 20% of NSCLC patients, especially in adenocarcinoma and never-smokers EGFR-mutants. EGFR is connected to cell proliferation, apoptosis and metastasis oncogenic functions [64], [65], [69]. TSG are essential negative regulators of cell growth like TP53 and STK53. When inactivated, TSG allows carcinogenesis processes to take over in favor of tumor evolution [64], [70], [71]. Other prevalent oncogene mutations in NSCLC include b-Myb, c-Myc, EML4-ALK and PIK4CA [72]–[75].

Moreover, multiple miRNAs expression in NSCLC is dysregulated, working as oncomiRs or tumor suppressors. miRNAs interplay with messenger RNAs (mRNAs) towards gene expression regulation, which in NSCLC, specific miRNA dysregulation is correlated with oncogenic progress mechanisms [76], [77].

1.2 NSCLC Diagnosis

1.2.1 Current diagnosis and limitations

NSCLC is generally diagnosed in advanced stages, therefore, the demand for new groundbreaking methods for lung cancer diagnosis is crucial. Correct diagnosis and staging of NSCLC in initial stages is linked with better prognosis, alongside with significantly improved survival rates [78], [79].

Current NSCLC diagnosis tests include imaging tests, sputum cytology and tissue sample analysis [80], [81]. However, NSCLC diagnosis is challenging due to lack of sensitivity and specificity from existing approaches for early diagnosis, false negative and positive results, besides most accurate methods are invasive and sometimes risky for patients [81]–[83].

Chest radiography is the standard first step in case of NSCLC suspect. An apparent tumor mass can be found through this method, although this result may constitute another lung condition apart from NSCLC [84], [85]. Regardless of being a simple, cost-effective and little radiation exposure technique, further testing is needed due to chest radiography limitations, just as low precision in early NSCLC diagnosis, false results, and missed diagnosis due to observer error, lesion characteristics and technical considerations [84], [86], [87]. Computed tomography (CT) scan is the following imaging method, showing an improved potential for NSCLC diagnosis in comparison to chest radiography. This methodology uses multiple X-ray scans combined with a contrast medium administration, providing high-quality detailed images [84], [88]. Concerning NSCLC diagnosis, CT scan manages to detect lung nodules, but cannot properly link them to NSCLC, neither distinguish between benign and malignant nodes [84], [89]. CT scans may comprehend about 100 to 1000 the radiation dose of conventional chest radiography, becoming harmful for people [90]. Magnetic resonance imaging (MRI) presents a favorable contribution for NSCLC diagnosis. Contrast agent injection is not required, plus generates imaging results with high definition from lung apices and the diaphragmatic area [84]. The combination of CT with position emission tomography (PET), known as PET-CT scan, allies the anatomic imaging precision of CT with the ability of PET to figure and evaluate metabolic processes via radioactive agents, resulting in more rigorous NSCLC diagnosis and staging [91].

Sputum cytology is a useful tool for NSCLC early diagnosis, essentially in patients with centrally located tumors and who experience hemoptysis [81]. Sputum samples are collected and further examined under microscopy for NSCLC cells search. Simple, non-invasive and cost-effective, sputum cytology requires a large number of examined samples for increased sensitivity. Nonetheless, this method can play an important role in NSCLC diagnosis as a supplementary test [92].

Biopsy remains the terminal procedure for NSCLC diagnosis, taking charge after suspicious results from previous tests. Lung tissue is collected and examined to detect NSCLC-related profile, representing a more precise diagnosis and cancer stage identification [81]. Bronchoscopy is the less invasive biopsy for NSCLC diagnosis, which comprises the insertion of a tube via mouth or nose until reaching lung airways under ultrasound or electromagnetic navigational assistance. Once there, tissue is extracted and further examined [84], [93]. CT-guided transthoracic needle aspiration and biopsy allow the removal of specific lung nodes via needle perforation through the chest. Like this, it is possible to inspect if samples have a benign or malign nature, and also determine NSCLC subtypes [94], [95]. Surgical lung biopsies like thoracoscopy and mediastinoscopy may be an option for lymph nodes collection and forward investigation for NSCLC staging [96]. Despite representing a fundamental role in NSCLC diagnosis and staging, biopsy approaches are extremely invasive, high-priced, and frequently carry risks like pneumothorax, air leakage and hemorrhage [97], [98].

1.2.2 New approaches

NSCLC diagnosis is challenging due to ongoing procedures limitations, reason why a massive research effort is being made forward-looking for new approaches with a potential application, concomitantly with current techniques, for an even more accurate and early NSCLC diagnosis and staging. Recent progress shows promising findings in the NSCLC diagnosis field by employing a multi-modal approach connecting different assays conclusions [99].

Liquid biopsies are raising attention in NSCLC diagnosis area by combining a less invasive sample collection procedure (blood collection), with the possibility of identifying multiple NSCLC related biomarkers such as nucleic acids, proteins and circulating tumor cells. Moreover, volatile components from exhaled breath analysis are also an interesting and non-invasive screening tool for early NSCLC diagnosis [99]–[101].

Biomarkers are biological measurable molecules which expression can be related to certain diseases and conditions, such as cancer. In NSCLC, sundry biomarkers arise as potential diagnostic agents, as well as therapeutic targets [102]. Multiple miRNAs show an unusual expression profile in NSCLC patients, even in early stages [103], [104]. NSCLC specific miRNAs detection based on molecular beacons (MB) fluorescence approaches can represent a powerful tool toward groundbreaking achievements in NSCLC diagnosis field [105], [106].

1.3 MicroRNAs (miRNAs)

1.3.1 Pri, pre and mature miRNAs

Non-coding RNAs (ncRNAs) represent a group of functional RNA sequences that do not advance through the translation process into proteins. miRNAs are single-stranded ncRNAs with about 21-23 nucleotides, which participate in extensive regulatory processes of gene expression via mRNA silencing [107], [108]. Besides their intracellular location and related functions, miRNAs can also be found in extracellular environment, more precisely in biological fluids like plasma and serum. Exosomes, microvesicles and other biological complexes can carry miRNAs and promote inter-cell communication throughout the organism [109].

Canonical miRNA biosynthetic pathway starts in miRNA host genes located along the genome. Multiprotein complex RNA polymerase II transcripts miRNA gene into a primary miRNA (pri-miRNA), which represents a hairpin structured large sequence. Double-stranded RNA-specific endoribonuclease (DROSHA) and DiGeorge syndrome critical region gene 8 (DGCR8) form a microprocessor complex that is responsible for the cleavage of pri-miRNA base strands, generating a shorter intermediate named precursor miRNA (pre-miRNA). pre-miRNAs are transported from the nucleus to cytoplasm via RanGTP-dependent exportin 5, wherein RNase II endonuclease Dicer (DICER) cleaves pre-miRNA's hairpin loop region, releasing a mature miRNA duplex. RNA-induced silencing complex (RISC) integrate the duplex, and whether -5p or -3p strand bind Argonaute (AGO) protein, forming an mRNA-targeted silencing system with only one mature miRNA [108], [110]–[112]. Distinct mature miRNA -3p and 5p strands from the same pre-miRNA can be co-expressed evenly, or exhibit different expression profiles depending on the tissue, connected with distinct functions throughout multiple biological pathways. According to some studies, the fact that one strand plays a certain biological role by aiming a specific target, does not mean that the respective passenger strand aim the same target, or either behave equally [113]–[115]. Furthermore, certain miRNAs are produced over alternative biogenesis pathways (noncanonical). Particular hairpin settings, involving introns per example, may enhance microprocessor complex (DROSHA/DGCR8) translation of pri-miRNAs, defined as "mirtrons", capable of sidestep DROSHA or DICER cleavage [111], [112]. Upon mature miRNA assemble with AGO, miRNA direct RISC to complementary mRNA for post-transcriptional processes suppression. Silencing mechanisms concern mRNA translation inhibition, protein degradation, plus AGO unfavorable influence [108], [116]. miRNAs biogenesis is further schematized in Figure 5.

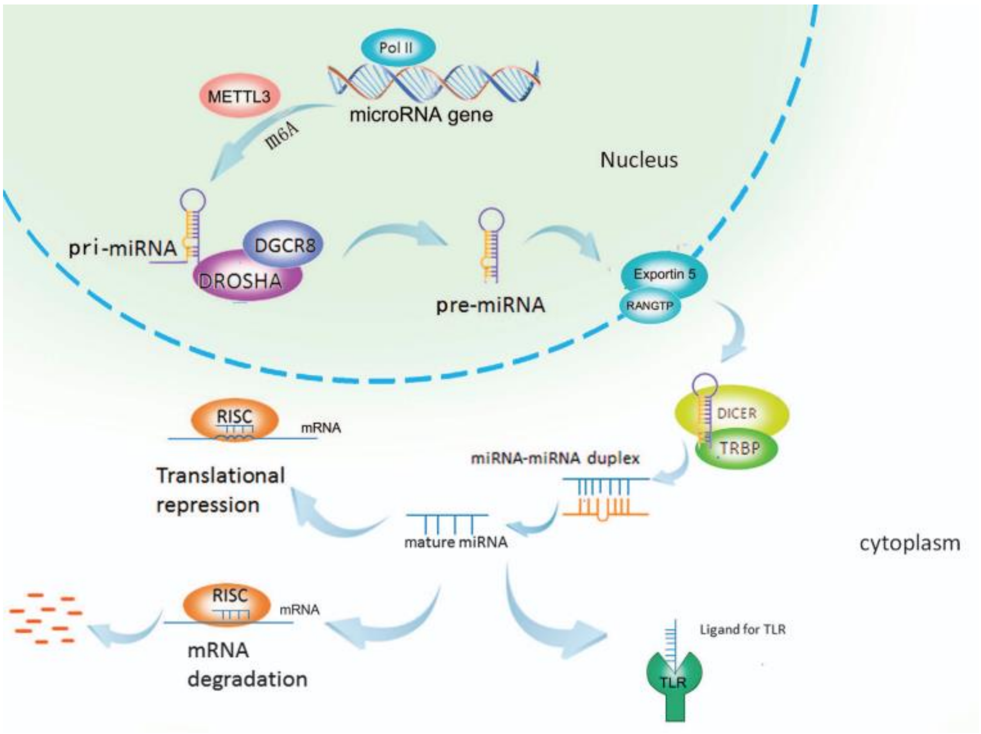

Figure 5. miRNAs biogenesis. miRNA genes are transcribed by RNA polymerase II into pri-miRNAs, that are cleaved and generate pre-miRNAs. Mature miRNA sequences result from pre-miRNAs processing by Dicer. Adapted from [117].

miRNAs are widely reported as significant elements in distinct biological processes, such as cell differentiation, proliferation and apoptosis. Abnormal miRNA expression is correlated with several diseases, and this dysregulation makes them potential biomarkers for disease diagnostic, subsequent progression, and personalized therapeutic strategies. Among a broad range of diseases and conditions, miRNAs have a substantial impact in neurodegenerative, cardiovascular diseases and cancer, including NSCLC [110], [118], [119].

1.3.2 miRNAs in NSCLC

Regarding NSCLC, numerous miRNAs are involved in tumor-related mechanisms, by acting either as tumor suppressor or oncogenic miRNAs. Tumor suppressor miRNAs control cells regular functions by preventing oncogenic mRNAs translation. They are downregulated in NSCLC, leading to oncogenic mechanisms to take over. On the other hand, oncogenic miRNAs are often up-regulated in NSCLC, promoting tumor development [119], [120]. Dysregulated miRNA expression in NSCLC affects regular signaling pathways and enhance oncogenic cascades, setting up a favorable configuration between diverse processes that will lead to cancer progression. Above-mentioned dysregulation could be triggered by genetic alterations concerning gene mutations, genomic amplifications, deletions, and epigenetic changes. Several miRNAs interplay in NSCLC features comprising uncontrolled cell proliferation, replicative immortality, apoptosis resistance and metastasis [119], [121]. Figure 6 shows miRNA dysregulation influence on NSCLC.

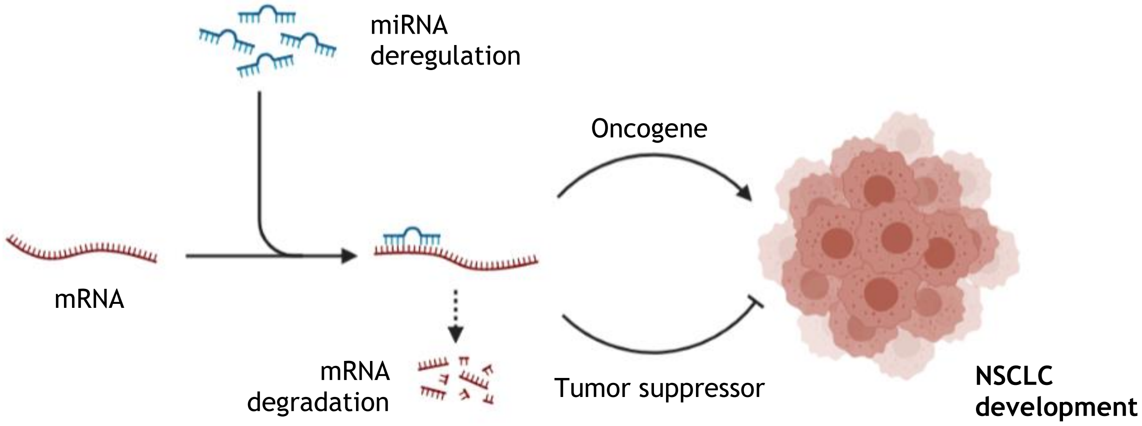

Figure 6. miRNA expression dysregulation interplay in NSCLC development and progression. Created and modified from [53].

Aberrant miRNA expression occurs in many NSCLC-associated biological samples. Malignant NSCLC tissue shows particular dysregulated miRNA profiles in comparison with control counterparts via molecular analysis [122], [123]. NSCLC A549 and HCC827 cell lines are useful NSCLC studies through miRNA sequencing [124]. Plasma, serum and sputum constitute important biological samples for NSCLC-miRNA screening, concerning a less invasive sample collection [125]–[127]. Peripheral blood mononuclear cells (PBMCs) are a population mostly composed of lymphocytes and monocytes, which stimulate immunological responses against NSCLC. PBMCs are arising as a potential source of significant biomarkers, including miRNAs [128]. Recent studies are connecting dissimilarities on PBMC signature miRNA profile in several diseases suchlike cancer, hepatitis C, tuberculosis, rheumatoid arthritis, among multiple other ones [128]–[131]. Differences in PBMCs miRNA expression under NSCLC condition result from initial immune engagement versus cancer malignancy [132].

miRNAs dysregulation opens up an all-new window of opportunities in the NSCLC field. Their potential in NSCLC diagnosis and therapy is extremely relevant for an even more accurate tumor identification, and in new era personalized medicine approaches. From correct diagnostic to prognosis prediction, miRNAs play a critical role in NSCLC, behaving as biological markers capable of differentiating NSCLC subtypes, discriminate between primary and metastatic tumors, and arising as basis of emerging minimally invasive methods [119], [133]. Research in miRNA-specific profile screening in multiple biologic samples is key in future early-precise diagnosis and prognosis of NSCLC [134].

1.3.3 NSCLC miRNAs in study

A NSCLC-related miRNAs were selected for the following research work, comprising miRNAs 21, 92b, 150, 155, 181a and 3662. Previous miRNA profiles were analyzed in plasma and PBMCs NSCLC samples, as well as microRNA 21 (miR-21) profile in A549 cell line.

miR-21 is a widely reported oncogenic miRNA (onco-miR), generally overexpressed in several cancers, including NSCLC [135]. Tumor suppressor PTEN prevents NSCLC progression over PI3K/AKT pathway blockage. PTEN is down-regulated in NSCLC via miR-21 repression, since miR-21 target to PTEN 3'-UTR binding site, leading to uncontrolled cell growth and tumor invasion [136]. miR-21/PTEN expression also influence treatment resistance, focusing chemo- and radiotherapy, plus tyrosine kinase inhibitor (TKI) approaches [137], [138]. Malignant relevant protein p53 is a miR-21 direct target. In NSCLC, p53 relation with miR-21 lead to PI3K/AKT/NF-kB suppression, and further cell apoptosis mechanisms malfunction [139]. Representative miR-21 expression in NSCLC tissue, along with circulating miR-21 levels in plasma and serum, provide an applicable biomarker for NSCLC early diagnosis and prognosis [135], [140].

MicroRNA 92b (miR-92b) expression is dysregulated in NSCLC, due to miR-92b participation in various NSCLC processes. Aberrantly miR-92b expression in NSCLC is linked with cell proliferation control by reversion-inducing-cysteine-rich protein (RECK), metastasis processes via Twist molecular targeting, and chemoresistance mechanisms across PTEN/ATK tract [141]–[144]. Moreover, miR-92b odd expression in NSCLC make it a potential and suitable NSCLC biomarker in new miRNA-based diagnosis methods.

Aberrantly expression of microRNA 150 (miR-150) in NSCLC regulates various malignant mechanisms. Forkhead box protein O4 (FOXO4) is a tumor suppressor that prompt cell cycle hold, apoptosis and DNA repair. miR-150 targets FOXO4, leading to protein suppression and consequent NSCLC cell migration enhancement [145]. miR-150 role in SIRT2/JMJD2A pathway regulation also affects NSCLC cell proliferation and migration [146]. miR-150 binds to 3'UTR of ASPP2, blocking its posterior translation and consequently stimulating cell proliferation and anti-apoptotic activity in NSCLC [147], [148]. Beyond stated miR-150 oncogenic role in NSCLC, Dai *et al.* reported that miR-150-5p prevents NSCLC metastasis and recurrence by targeting high mobility group AT-hook 2 (HMGA2) and β-Catenin signaling pathways, acting as a tumor suppressor in NSCLC [149]. Unusual expression profile of miR-150 in NSCLC tissue, serum and PBMCs suggest its potential as a biomarker for NSCLC early diagnosis and prognosis [150]–[152].

Concerning NSCLC, microRNA 155 (miR-155) is one of the most reported miRNAs, playing a crucial part in a wide variety of tumor processes. miR-155 targets tumor suppressor genes like PTEN, suppressor of cytokine signaling 1 (SOCS1) and 6 (SOCS6). Corresponding repression by up-regulated miR-155 results in worse survival rates and NSCLC further development [153]. Programmed cell death 4 (PDCD4) is under-expressed in NSCLC as a result of miR-155 inhibition, inducing out of control cell proliferation and metastasis in NSCLC [154]. Dysregulated cell growth is also influenced via miR-155 target FOXO1 suppression and sequent reactive oxygen species (ROS) generation [155]. miR-155 high expression is associated with radiotherapy resistance, promoting a proportional increase in hexokinase 2 (HK2) and glycolysis, causing NSCLC radioresistance [156]. Moreover, miR-155 detection in biological samples represents a promising biomarker for NSCLC early diagnosis, besides being useful in its prognosis [157]–[160].

Multi-functional microRNA 181a (miR-181a) is usually down-regulated in NSCLC, and besides the inherent oncogenic profile in multiple cancers, miR-181a mainly act as a tumor suppressor in NSCLC [161], [162]. miR-181a inhibit KRAS, mitogen-activated protein kinase (MAPK), and cyclin-dependent kinase 1 (CDK1) oncogenes in NSCLC by targeting them, and consequently reducing cell proliferation and migration [163]–[165]. Pro-apoptotic mechanisms are also regulated by miR-181a in NSCLC, due to its connection with B-cell lymphoma 2 (Bcl-2) and p53 targets. miR-181a promotes a synergetic function between tumor cells and the surrounding microenvironment, whereupon miR-181a regulation in M2 macrophage-mediated processes hold up NSCLC development. Despite miR-181a common under-expressed profile in NSCLC, miR-181a was up-regulated in NSCLC patients treated with the EFGR inhibitor Gefinitib, exhibiting a relation in NSCLC therapy resistance [163]. Dysregulated miR-181a is an NSCLC biomarker in tissue and serum, having a relationship with NSCLC diagnosis and distinct staging [162], [166].

MicroRNA 3662 (miR-3662) is over-expressed in plasma from NSCLC patients, representing a promising biomarker for early diagnosis [167], [168]. Although miR-3662 function in NSCLC mechanisms needs further study, miR-3662 role as an onco-miR and a tumor suppressor is reported in several malignancies such as hepatocellular carcinoma [169].

1.3.4 miRNA profiling

The miRNA expression profile was studied in plasma and PBMCs samples from NSCLC patients and healthy volunteers (without cancer disease). Plasma and PBMCs were isolated from whole blood samples, followed by RNA extraction. Gel electrophoresis technique was applied for RNA integrity check. RNA is converted in template complementary DNA (cDNA) via reverse transcription reaction, which advances for real-time polymerase chain reaction (qPCR) for individual miRNA profiling for each sample.

Since miRNAs can be present in lower quantities on some biological samples, and due to their RNase degradation sensibility, sample processing for plasma and PBMC isolation was executed using only solutions made with diethyl pyrocarbonate (DEPC) treated water, in order to constrain RNase activity [170]. Plasma hemolysis results from red blood cell (RBC) disruption, leading to RBC content release into blood plasma. RBC contamination in plasma affects several miRNA expression profiles, resulting in misleading miRNA quantification data. According to Muklebust *et al.*, miR-371a-3p and miR-372-3p expression in plasma is directly influenced by hemolysis. Hemolysis can be measured on plasma by hemolysis signature 414 nm absorbance peak analysis, or via miR-23a/miR-451 ratio [171]–[173]. Plasma hemolysis is checked via spectrophotometry, and during PBMCs isolation protocol, biological samples are treated with a RBC lysis buffer, due to RBC contamination and possible impact in miRNA proper screening. RNA extraction from plasma and PBMCs is performed via phenol/guanidine-based lysis. A phenol/guanidine solution is added, inducing sample solubilization under RNA activity inhibition. Chloroform addition separates aqueous and organic layers, and the containing RNA aqueous phase goes into further steps, where ethanol is added to promote binding conditions to the silica-membrane of the column. Extracted RNA is quantified via spectrophotometry, taking in count $A_{260/280}$ ratio and $A_{260/230}$ for protein and organic solvent contamination [174], [175].

In gel electrophoresis, molecules are loaded into the gel and migrate due to electric field application, getting separated based on their size [176]. Ribosomal RNA (rRNA) represent near 80% of total RNA, within the rRNA 28S and 18S being the most predominant species. rRNAs 28S and 18S have around 5 kb and 2 kb, respectively, and their analysis via gel electrophoresis indicate RNA quality and integrity by reflecting mRNA profile. RNA from each sample is loaded into an agarose gel for gel electrophoresis, whereafter RNA sample band profile is analysed by identifying 18S and 28S ribosomal RNA bands directly correlated with extracted RNA integrity [177], [178].

RNA samples follow to cDNA synthesis, where miRNAs go through a polyadenylation step for higher specificity screening, and further reverse transcription by reverse transcriptase enzyme, which is responsible for RNA transformation into cDNA under specific conditions [179], [180]. cDNA template proceeds to qPCR for individual miRNA amplification and quantification. Thermal-stable DNA polymerase amplifies a specific miRNA sequence based on a unique set of primers that is added, allowing the amplification of only one mature miRNA. Initial denaturation step divides the two DNA strands. Thereafter, primers hybridize to respective strands in the annealing step, and later DNA polymerase recognizes primer-strand binding, generating sequence extension. During extension, a binding dye (SYBR Green) intercalates double-stranded DNA, issuing a measurable fluorescent signal for sequence amplification [181], [182]. Cycle threshold (Ct) data from qPCR is processed and quantified relatively to housekeeping gene values via $2^{-\Delta\Delta Ct}$ method [183], [184]. Housekeeping genes work as a control gene, that is overall expressed equally among samples in study [185]. Widely used as a reference in miRNA profiling studies, miR-103a and miR-191 expression profile in healthy and diseased individuals is similar, reason why they are suitable as housekeeping genes for miRNA qPCR data normalization [186]–[189]. PCR steps are further represented in Figure 7.

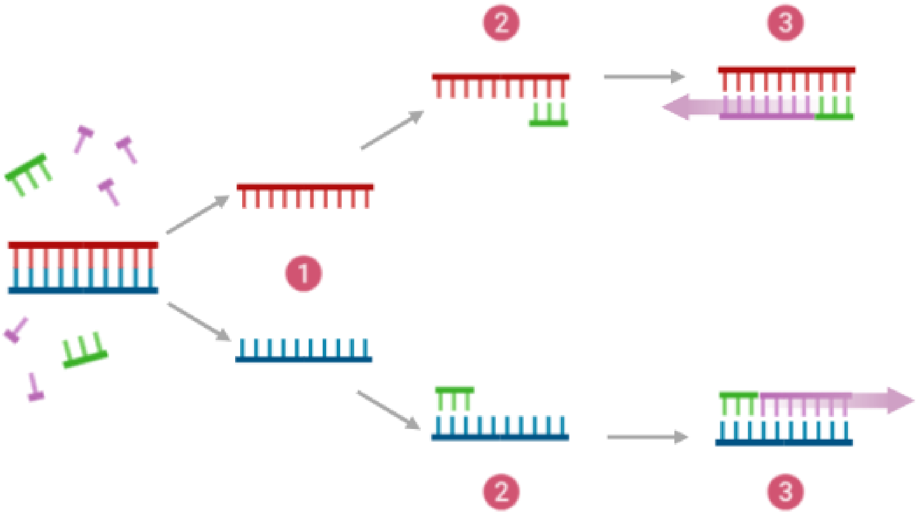

Figure 7. PCR sequence amplification steps. 1) Denaturation; 2) Annealing; 3) Elongation. Created and modified from [53].

1.4 Molecular Beacons

1.4.1 Structure and features

Advances in molecular engineering lead to MB development, consisting of an oligonucleotide DNA probe able to detect specific nucleic acids via fluorescent signal. MBs structure includes a recognition site with a hairpin loop sequence of 15-30 nucleotides, followed by two complementary strands that able the MB to close and form a stem-loop structure. Regarding the opposite strands of the MB stem, at the end of one sequence, there is a fluorophore (donor), and at the end of the complementary, there is a quencher (acceptor). MB stem-loop characteristic structure brings the fluorophore and the quencher together via stem sequence complementarity, resulting in fluorescence quenching due to both the fluorophore and quencher proximity. Target complementary sequences (DNA or RNA) interact with the MB loop region, promoting a strong intermolecular connection and stem split. Upon hybridization, stem sequences separate alongside with the fluorophore and the quencher at the end of each strand, which will guide to fluorescence recovery signal [190], [191].

MB design must rely on MB ability to form a stem-loop structure and on Förster resonance energy transfer (FRET) mechanism. In FRET, there is an energy transfer between the acceptor and the donor, in which the major part of the energy absorbed by the donor is released as heat, and only a small portion correspond to light emission. MB energy-transfer mechanisms are divided into two categories: dynamic and static fluorescence quenching. The dynamic approach is based on FRET phenomenon, where MB hybridization and subsequent donor-acceptor division result in photon release through donor-acceptor separation. Frequently used fluorophores consist of fluorescein (FAM) and tetramethylrhodamine (TAMRA). About quenchers, most reliable options are 4-(dimethylaminoazo) benzene-4-carboxylic acid (dabcyl) and Black-Hole Quenchers BHQ1 and BHQ2 [191], [192].

MBs conformation can differ between target hybridized, free stem-loop and free random coil conformation, having lower free energy in the stem-loop configuration than in the random coil one. MB stem design should find a compromise between length and GC content for the desired purpose. MB selectivity can be improved by stem elongation or GC content increase; however, a lower degree of hybridization is correlated with longer and stable stems. On the other side, short stem MB provides a higher background signal and can present lack of selectivity. Temperature increasing promotes MB structure folding from stem-loop to random coil configuration. For the development of MB for high temperatures applications, more stable stems are crucial for background signal reduction [191], [193]. Figure 8 displays MB stem-loop and hybridized structures.

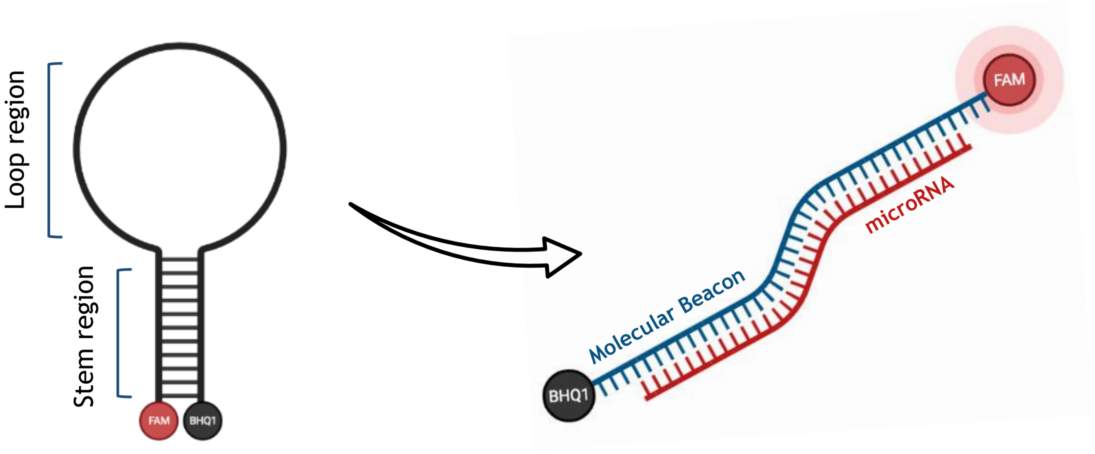

Figure 8. MB representation in the folded stem-loop configuration, and further hybridized with a specific miRNA target.

1.4.2 Applications

MB technology arises as a potential bioanalytical system in the biotechnology field, presenting a wide group of useful features and advantages.

One of the most interesting features of MBs relies on the capacity not only to detect nucleic acids, but also to detect proteins and enzymes. Gene detection techniques such as PCR often use specific designed MBs to hybridize with complementary PCR products. MB hybridization monitor interest gene amplification over the cycles, providing a fluorescent measurable output in qPCR strategies [191], [194]. Biosensors with surface immobilized MBs are trending in molecules screening. For example, a molecular aptamer beacon (MAB) with G-quadruplex (G4) formation capable of integrating a micro-chip surface, showed ability to detect prostate cancer protein nucleolin [191], [195].

Small molecules like miRNAs are also emerging as potential targets for MB detection. Dysregulated miRNA profile among various diseases, along with the aptitude to detect their levels through MB approaches, represent a prominent opportunity in diagnosis, prognosis and therapy in mentioned conditions, including NSCLC [106], [196], [197].

1.5 Biophysical characterization

1.5.1 Förster resonance energy transfer (FRET)

Theodor Förster first introduced FRET as the mechanism where two fluorescent molecules, a donor and an acceptor, transfer energy between themselves. A brief introduction on FRET is above presented in chapter 1.4.1 - Structure and functions, where its connection to MB is explored.

In FRET, two fluorescent-sensitive molecules within a specific proximity start to interact with each other, promoting an energy transfer from the excited donor to the acceptor. The donor is a fluorescent molecule capable of light-signal emission, and the acceptor is a quencher molecule that absorbs such light. Corresponding energy transfer is non-radiative, since dipole-dipole interactions are created amongst the donor and the acceptor [191], [198]. The donor is excited by a photon, that in case of being close to the acceptor, transfers the correspondent exciting energy to the acceptor. Such energy is released as heat, and a small amount as light, due to the acceptor quenching. However, when the donor and the acceptors separate, the quenching effect no longer works, as result of the distance between the quencher and the donor, which will radiate a fluorescent signal [192], [199].

FRET mechanism represents a tool for molecule structure and interaction studies. MB structure and characteristics like melting temperature (T_m) can be studied via fluorescence monitoring in a FRET melting assay, in which donor-acceptor dissociation can be followed through fluorescent signal increase. Interaction studies implying MB and targets are also an option via FRET analysis, placing both MB and the target together by inspecting the fluorescent profile [192], [200]–[202]. Figure 9 exemplifies FRET phenomenon.

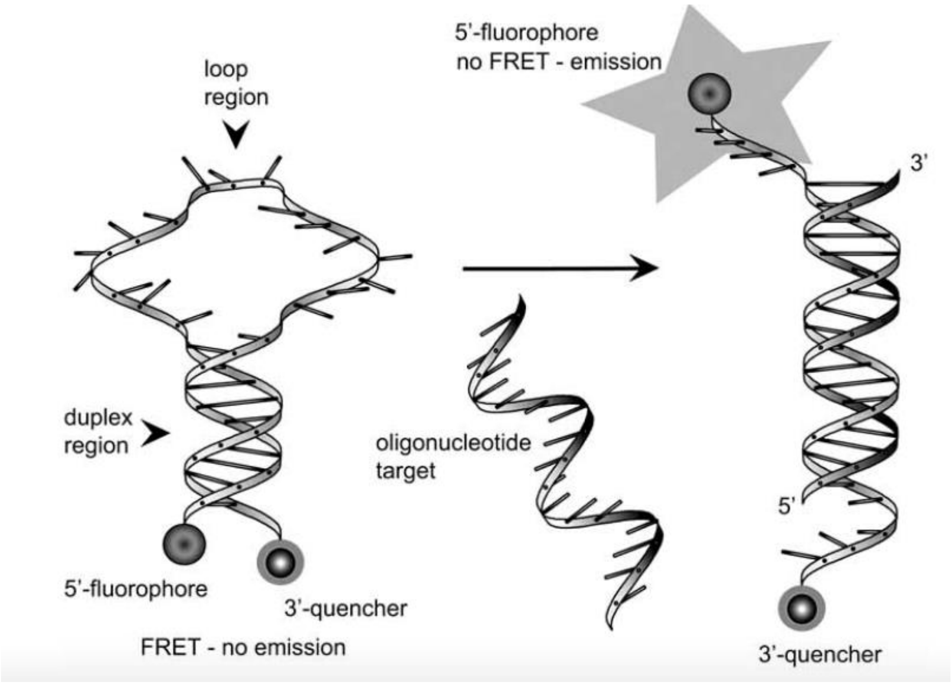

Figure 9. FRET phenomenon representation. At the folded structure no fluorescence is emitted because of FRET. Upon hybridization, FRET phenomenon no longer exists and fluorescence is emitted by fluorophore. Adapted from [203].

FRET-based approaches are in the vanguard of bioanalytical sciences, mostly because of all the application potential in biophysical characterization and specific molecule recognition [198], [204].

1.5.2 Circular dichroism (CD)

Chirality is a property of asymmetry, and biological molecules that present asymmetrical structures are defined as chiral. Chiral molecules interaction with polarized light provide data for molecule structure characterization. Circular dichroism (CD) spectroscopy is able to study molecules structure by their chirality properties, involving the evaluation of different absorption of left-hand and right-hand circularly polarized light, represented as ellipticity [205], [206].

CD spectroscopy has a wide range of applications, focusing secondary structure of proteins and nucleic acids, besides providing some information on the tertiary structure. CD melting involves temperature control upon spectra acquisition, enabling thermal studies and T_m determination. Besides abovementioned applications, CD is useful for folding and unfolding kinetics and thermodynamics analysis, as well as interaction studies between proteins, nucleic acids and ligands [205], [207]–[209].

MB conformational studies, plus T_m determination, can be accomplished via CD. MB stem region is a DNA duplex, which corresponding spectra on CD is represented by a positive long-wavelength band at around 260-280 nm and respective band at 270 nm, and a negative band nearby 245 nm [209]–[211].

1.5.3 Nuclear magnetic resonance (NMR)

Nuclear magnetic resonance (NMR) was found out by Purcell and Bloch and is defined by the interaction of magnetic moments of atoms nuclei via magnetic field oscillation, producing a characteristic electromagnetic signal. Nuclear spin is a form of angular momentum in nuclei correlated with its magnetic moment, which value is defined by a spin number. Nuclei with an even number of protons and neutrons have a zero nuclear spin, however, an odd number of protons and neutrons in nuclei generate a non-zero nuclear spin. Common nuclei in NMR applications are ^{1}H, ^{31}P, ^{13}C and ^{15}N, which have a 1/2 spin number. Magnetic nuclear spins are aligned by applying magnetic field B_0, which are posteriorly perturbed by a low radiofrequency (RF) magnetic field B_1 for a short time. After B_1 short application, tilted magnetization returns to B_0, causing an electromotive force responsible for the NMR signal [212].

NMR spectroscopy provides information on an atomic level, being useful in structural characterization, from molecule topology and kinetics to interaction studies. Thereby, NMR has a huge potential application in several areas, from food to the medical biotechnology field [213], [214].

NMR of nucleic acids allow high-resolution structure determination, dynamics, and interaction studies. Nucleic acids NMR experiments are often done using heavy water (D_2O) as a solvent due to nucleic acid large number of protons [215], [216]. MB study via NMR enables structure configuration, by monitoring NMR DNA duplex and MB hairpin characteristic signal between 12-14 ppm, as well as analysing its behavior at different temperatures and NMR profile changes with the complementary target sequence, and consequent hybridization [217]–[219].

1.5.4 Fluorescence spectroscopy

Fluorescence approaches are in the vanguard of multiple research fields, such as biotechnology and medical diagnosis. Highly sensitive fluorescence detection and its potential application in a wide range of processes, made fluorescent methods arise in current science research [220].

Fluorescence spectroscopy can detect fluorescence levels of a sample. An ultraviolet (UV) light beam is applied to the sample, exciting molecules electrons, which will return to their ground state and emit a photon, measurable by fluorescence spectroscopy. Fluorescence can be measured in a spectrofluorometer, capable of reading individual samples or plates with multiple wells and different conditions [220], [221].

Furthermore, in MBs, fluorescent assays represent a useful tool for structure and interaction studies. Background fluorescent signal of MB in their stem-loop configuration allows quenching efficacy evaluation [220]. By increasing temperature in MB sample, it is possible to monitor the denaturation profile and to determine the MB T_m. Hybridization dynamics can also be studied via fluorescence spectroscopy, just by adding synthetic complementary sequence to MB sample and varying the temperature. Condition screening and biological sample analysis can be carried out in fluorescence-based microplates, enabling condition changing and different biological samples distribution throughout the plate wells [222], [223].

1.6 *In situ* MB miRNA detection

1.6.1 MB hybridization assays

MB methodology and dynamics were previously reported in section 1.4 - Molecular beacons, as well as the used techniques for biophysical and interaction studies in section 1.5 - Biophysical characterization. After MB structure analysis and T_m determination, the hybridization assays were performed in a 96 well fluorescence microplate with MB, synthetic miRNAs, and biological samples. In the first place, condition screening assays with MB and complementary sequence were executed for prime conditions resolution to proceed with biological assays. Sodium dodecyl sulphate-polyacrylamide gel electrophoresis (SDS-PAGE) technique was also applied for MB hybridization studies [224]. Thereafter, biological studies with total RNA and qPCR products were carried to miRNA detection.

In resume, throughout FRET phenomenon, MBs provide a measurable fluorescent signal upon hybridization with the complementary sequence. In the stem-loop configuration, quencher absorbs fluorophore's fluorescence, but when MB hybridize with the corresponding sequence, the MB stem split, resulting in a donor-acceptor separation and consequently donor fluorescent signal [190], [191]. Thus, miRNA detection via MBs approaches is rising in the NSCLC diagnosis and therapy area [106].

Several miRNAs are dysregulated in multiple diseases, representing valuable biomarkers. miRNA detection using MB approaches in biological samples suchlike tissue, plasma and serum, are starting to show up, due to their potential to supply useful information on the diagnosis, prognosis and therapy strategies [105], [225], [226]. MB development targeting miR-21 and miR-155 is reported, considering that they play a critical role in multiple cancers, including NSCLC [227], [228]. A significant effort is being made by the scientific community to determine a specific NSCLC miRNA expression profile, to give an early and precise NSCLC diagnosis, prognosis, and create innovative personalized therapies. Studies on MB-miRNA detection in NSCLC are being carried out recently, showing promising results in specific miRNA screening and new applications for its diagnosis [106], [229]–[231].

1.6.2 Condition screening and biological samples

MB hybridization dynamics need to be studied in order to get effective and precise fluorescence results in biological sample miRNA screening. A set of different conditions need to be optimized regarding MB hybridization assays.

One of the most critical conditions is temperature, bearing in mind that MB hybridization occurs in a particular temperature range. MB T_m is an important reference for hybridization temperature determination, giving a starting point for temperature screening. Hybridization time is also a condition to have in count and should be enough for hybridization reactions to take place. MB and synthetic miRNA-target sequences were tested in different temperature and hybridization time ranges. MB and RNA concentration should be adjusted, considering that MB concentration has to be high enough to detect complementary miRNA sequences, as well as the RNA concentration, since target miRNA level in total RNA can be low and not detectable [226], [227]. Additional concerns in MB hybridization assays consist in after plate preparation; the plate should be light protected because of MB light-sensitivity, plus carefully agitated for sample homogeneity in fluorescence detection upon hybridization [197], [225].

A representative illustration of the developed MB-miRNA *in situ* detection approach is depicted in Figure 10.

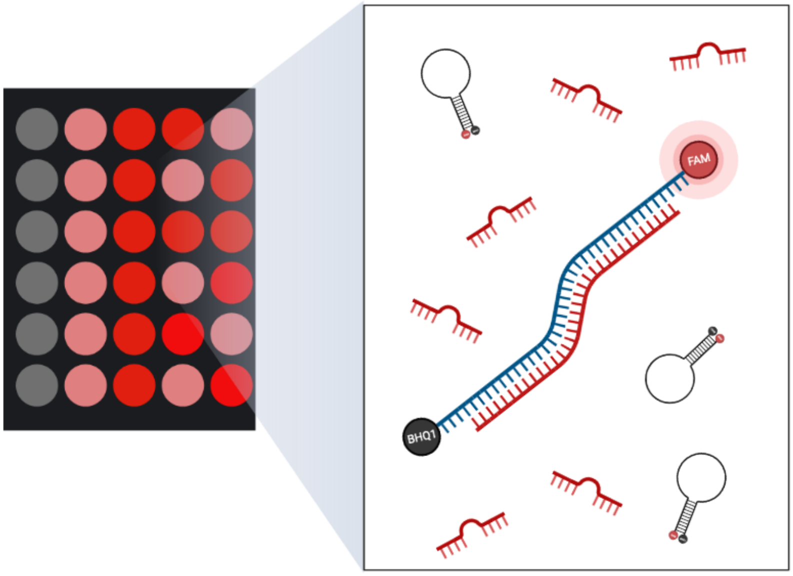

Figure 10. MB-miRNA in situ detection approach representation. MB and specific miRNA are placed in a microplate for fluorescence measurement. Higher fluorescence values are proportional to miRNA concentration.

In this work, NSCLC-miRNAs were profiled in PBMCs and selected for detection in biological samples. MBs were designed targeting miRNAs 21-3p and 21-5p, which were characterized via biophysical techniques like FRET-melting, CD and NMR spectroscopies. Further interaction studies were carried for MB hybridization optimization with synthetic miRNA sequences, comprising structural MB dynamics and hybridization kinetics within FRET-melting, NMR, SDS-PAGE electrophoresis, and *in situ* miRNA detection via fluorescence assays. Optimization screening assays were run with a synthetic miRNA sequence, and posterior biological miRNA screening was done with total RNA from NSCLC cell lines and patient PBMCs [124], [132]. Presented research work tasks and workflow are depicted as a graphical abstract in Figure 11.

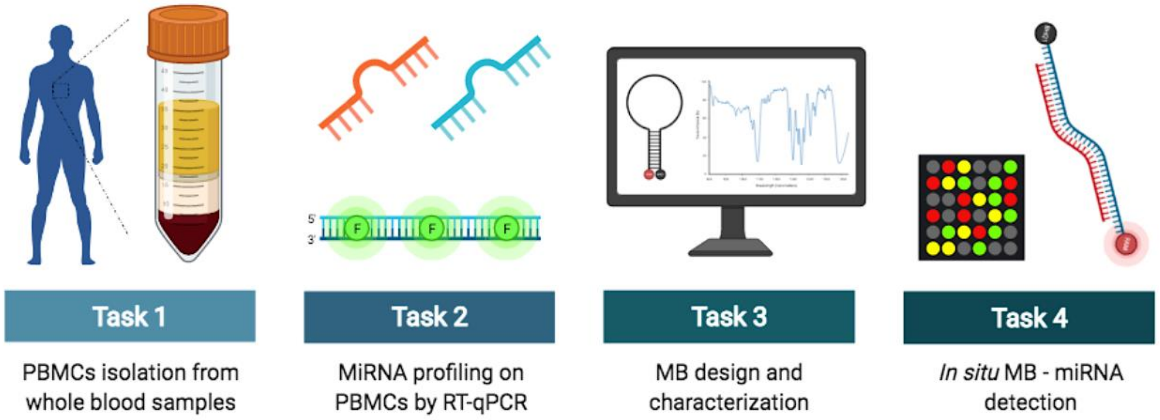

Figure 11. Graphical abstract comprising biological samples processing at task 1, miRNA profiling in task 2, MB design and biophysical characterization in task 3, and the miRNA detection via MB in task 4.

Dissertation further chapters will initially enumerate all the used materials and employed techniques throughout this research work, followed by the obtained results discussion based on literature review. Finally, work major conclusions will be indicated along with future perspectives.

CHAPTER 2 – Aims of Work

2. Aims of Work

The principal objectives are delineated in chapter 2 - Aims of Work. So as to conduct this work and present collected results, within its organization, individual objectives are established. Different tasks comprising several techniques need to be taken to reach purposed goals.

This research work holds two main objectives. The first one is the screening of miRNA study-panel in NSCLC patients' plasma and PBMCs, followed by the development of a MB based-approach for NSCLC diagnosis via dysregulated miRNA detection. Thereby, in order to advance and achieve this study purpose, the following objectives are:

1. Plasma and PBMCs sample-bank storage from NSCLC patients;
2. miRNA profiling in NSCLC biological samples;
3. Design and biophysical characterization of a miRNA targeted MB;
4. MB hybridization optimal conditions screening;
5. *In situ* MB-miRNA detection for NSCLC diagnosis.

CHAPTER 3 – Materials and Methods

3. Materials and Methods

The following section, chapter 3 - Materials and Methods, refers to the distinct components and techniques applied to current research work. Herein, each reagent, solution, and equipment are indicated, together with every protocol described step by step in detail.

3.1 Materials

Every solution used in the following work were prepared with ultrapure grade water obtained from a Mili-Q system from Millipore (Burlington, MA, USA). Solutions for biological sample processing have added DEPC upon preparation, and for cDNA synthesis and qPCR assays, DEPC-treated water from Thermo Fisher Scientific (Waltham, MA, USA) was used.

Blood samples collection from NSCLC patients were carried out in the public hospital Centro Hospitalar Cova da Beira (CHUCB), by dint of a collaboration protocol with Dr. Salete Valente.

RNA extraction for miRNA isolation was performed using miRNeasy Serum/Plasma Kit (Cat. No. / ID:217184, Qiagen, Hilden, Germany) for plasma samples, and miRNeasy Micro Kit (Cat. No. / ID:217084, Qiagen, Hilden, Germany) for PBMCs. For cDNA synthesis, miRCURY LNA RT Kit (Cat. No. / ID:339340, Qiagen, Hilden, Germany) was applied, and succeeding qPCR experiments were carried out via miRCURY LNA SYBR® Green Kit (Cat. No. / ID:339346, Qiagen, Hilden Germany). Specific miRCURY LNA miRNA PCR assay primers for housekeeping miRNAs, along with NSCLC-related miRNAs were employed in qPCR miRNA profiling assays. Table 1 resumes miRCURY LNA miRNA PCR assay primers used in RT-qPCR assays.

Table 1. miRCURY LNA miRNA PCR assay primers for RT-qPCR miRNA screening

Name (miRCURY primers)	Role	miRNA target sequence (from 5´to 3´)
hsa-miR-103a-3p	Housekeeping	AGCAGCAUUGUACAGGGCUAUGA
hsa-miR-191-5p	Housekeeping	CAACGGAAUCCCAAAAGCAGCUG
hsa-miR-21-3p	NSCLC-related	CAACACCAGUCGAUGGGCUGU
hsa-miR-21-5p	NSCLC-related	UAGCUUAUCAGACUGAUGUUGA
hsa-miR-92b-5p	NSCLC-related	AGGGACGGGACGCGGUGCAGUG
hsa-miR-150-3p	NSCLC-related	CUGGUACAGGCCUGGGGGACAG
hsa-miR-155-3p	NSCLC-related	CUCCUACAUAUUAGCAUUAACA
hsa-miR-155-5p	NSCLC-related	UUAAUGCUAAUCGUGAUAGGGGUU
hsa-miR-181a-5p	NSCLC-related	AACAUUCAACGCUGUCGGUGAGU
hsa-miR-3662	NSCLC-related	GAAAAUGAUGAGUAGUGACUGAUG

MBs for miR-21-3p and miR-21-5p recognition were designed and marked with fluorophores FAM and HEX, and quencher BHQ1. Therefore, miR-21-3p synthetic sequence, reverse complementary MB1 21-3p, and reverse MB2 21-3p were purchased from Eurofins (Luxembourg). Additionally, reverse complementary MB3 was obtained from ALS Oligonucleotides (Viseu, Portugal). For miR-21-5p detection, miR-21-5p synthetic sequence and MB1 21-5p arrived from Eurofins (Luxembourg). Acquired MBs and miRNA synthetic sequences are indicated in Table 2 shown below.

Table 2. MB and miRNA oligonucleotide synthetic sequences

Name	Sequence (from 5´to 3´)
miR-21-3p	CAACACCAGUCGAUGGGCUGU
miR-21-5p	UAGCUUAUCAGACUGAUGUUGA
MB1 21-3p	**FAM** - **CCGCGC**ACAGCCCATCGACTGGTGTTG**GCGCGG** - **BHQ1**
MB2 21-3p	**HEX** - **CCGCGC**GTTGTGGTCAGCTACCCGACA**GCGCGG** - **BHQ1**
MB3 21-3p	**HEX** - **CCGCGC**ACAGCCCATCGACTGGTGTTG**GCGCGG** - **BHQ1**
MB1 21-5p	**FAM** - **CCGCGC**TCAACATCAGTCTGATAAGCTA**GCGCGG** - **BHQ1**

3.2 Methods

3.2.1 miRNA profiling in NSCLC samples

3.2.1.1 Human blood sample collection

A partnership between Dr. Carla Cruz from the Health Sciences Research Centre of University of Beira Interior (CICS-UBI) and Dr. Salete Valente in representation of CHUCB hospital was established. The study included 59 patients previously diagnosed with NSCLC at different stages with and without treatment from CHUCB hospital, and the control group involved 22 healthy male and female volunteers with no history of cancer disease. This study was approved by the CHUCB Ethics Committee ref. 35/2019, and was included a written informed consent for each participant.

Fresh human blood collection took place in CHUCB, where 3 mL blood samples from patients were collected in ethylenediaminetetraacetic acid (EDTA) - coated tubes and transported to CICS-UBI laboratories just a few moments after collection, in recommended refrigerated conditions. Upon reaching the laboratory, the tubes are identified according to the patient database, and immediately proceed to further processing. Healthy control group blood collection was carried in CICS-UBI by Dr. Adriana Santos, which followed directly for processing.

3.2.1.2 Plasma isolation

Fresh whole blood containing tubes advanced to a first centrifugation at 3000 rotations per minute (rpm) for 15 min at room temperature, and the maximum amount of plasma was collected by a micropipette into a 2 mL eppendorf tube. Extracted plasma continued to an additional centrifugation step at 14000 rpm for 5 min at 4 °C, for further RBC debris deposition, and then was transferred into a cryovial.

Plasma hemolysis was checked on an Evolution™ 201/220 UV-Visible Spectrophotometer (Thermo Fisher Scientific, USA). Plasma tubes were placed in ice, and then diluted with Mili-Q water in a 1:20 proportion into a quartz cuvette. Each plasma sample absorbance was scanned in an interval between 350 nm and 650 nm, which contain the 414 nm characteristic peak for plasma hemolysis. A reading value for A_{414} higher than 0.2 means that sample was hemolyzed, and subsequently is incapable of undergoing into further miRNA screening assays [171], [172]. Plasma samples were identified and stored at -80°C until further use.

3.2.1.3 PBMCs and cell lines isolation

After plasma isolation, an equal volume of 1× phosphate-buffered saline (PBS) solution was added to the remaining blood samples. Samples were homogenized with a plastic Pasteur pipette, and carefully transferred into a 50 mL polypropylene tube containing an equal volume of Pancoll separating solution (PAN-Biotech, Germany). Falcon tubes were centrifuged at 2200 rpm for 30 min at room temperature, followed by the PBMCs ring extraction with a plastic Pasteur pipette to a new 50 mL polypropylene tube. Then, 1×PBS was added to the PBMCs falcons up to 50 mL, and centrifuged at 1800 rpm for 10 min at 4 °C. The supernatant was discarded, the pellet resuspended in 10 mL of 1× PBS and centrifuged again at 1500 rpm for 10 min at 4°C. After discarding the supernatant, a pre-warmed RBC lysis buffer solution was added to the pellet and the sample was incubated at 37°C under 10 min with homogenization. The sample proceeded to centrifugation at 1500 rpm for 10 min at room temperature, followed by two 1×PBS washing steps suchlike the above-indicated ones, at 1500 rpm for 10 min at room temperature. Finally, the PBMCs were resuspended in 1 mL of 1× PBS, and transferred to a 2 mL Eppendorf tube for cell count.

For cell counting, 10 μL of each PBMCs sample was diluted with trypan blue solution, and then loaded into a hemocytometer that goes under a microscope. Total cells around the four hemocytometer quadrants were counted, and cell concentration was calculated by the equation:

$$Total\ cells/mL = (\frac{Total\ cell\ count}{4}) \times dilution\ factor \times 10^4$$

Then, 1 × 10^6 (million) cells were divided into 1.5 mL eppendorf tubes, which were centrifuged at 14000 rpm for 5 min at 4 °C. The supernatant was discarded, and cells were put in liquid nitrogen for instant sample freeze before stored at -80°C, until using.

A549 lung cancer cell line and normal human dermal fibroblasts (NHDF) cell line were used in this study. Cell lines were cultured in appropriate medium, collected, counted, and washed with 1× PBS solution. Thereafter, cell line samples were separated into 1 million cells followed by abovementioned protocol for PBMCs, culminating in cells liquid nitrogen freeze and storage at -80°C, until further use.

3.2.1.4 Total RNA extraction and quantification

RNA extraction from cell lines, PBMCs and plasma samples was performed based on the protocols provided on the miRNeasy Micro Kit and miRNeasy Serum/Plasma Kit handbooks. The miRNeasy Micro Kit was used on cell lines and PBMCs, and the miRNeasy Serum/Plasma Kit for the plasma. Specified miRNeasy kits were designed for efficient lysis, denature protein complexes, inhibit RNases and eliminate major DNA residues from lysis through organic extraction.

About 1 million cell pellets and PBMCs were thawed by gently flicking the tubes, and 700 µL QIAzol lysis reagent was added to the tubes that were homogenized by pipetting and vortex. Tubes containing the homogenate were incubated at room temperature for 5 min, and then 140 µL of chloroform was added, followed by a tube shaking step for 15 s. Tube was placed on the benchtop at room temperature for 3 min, and therefore centrifuged for 15 min at 12000 x *g* at 4 °C. After centrifugation, the upper aqueous phase containing the RNA was transferred to a new tube, and 525 µL of 100% ethanol was added and well mixed by pipetting up and down. In the coming step, 700 µL of the preceding sample was pipetted into an RNeasy MinElute spin column with a collection tube, that proceeded to centrifugation at 8000 × *g* for 15 seconds for RNA membrane binding. Flow-through was discarded, and the remaining sample was transferred into the spin column until it was over, which was centrifuged in the same conditions as the previous one. Flow-through was again discarded, and two further washing steps comprising the addition of 700 µL of buffer RWT, and subsequent addition of 500 µL of buffer RPE in the spin column were centrifuged in the conditions above-indicated for column sample processing, and the flow-through was discarded at the end. A final membrane washing step was carried out by the addition of 500 µL of 80% ethanol to the column, and posterior centrifugation for 2 min at 8000 × *g*. Attached collection tube was discarded with flow-through, the column was placed in a new one, and centrifuged at full speed for 5 min to fully dry the membrane. Spin column was moved into a new 1.5 mL eppendorf tube and 14 μL of RNase-free water was added directly to the center of the membrane. Column and the collection tube continued to the final centrifugation at full speed for 1 min, for RNA elution.

Plasma samples processing differ from the cell line/PBMCs RNA extraction described protocol in some reagent added volumes. Initially, the volume of starting plasma was 200 μL, QIAzol added volume was 1000 μL, chloroform was 200 μL, and ethanol 100% in the sample addition step was 900 μL. Besides reagent volumes, the protocol for RNA extraction from plasma was performed correspondingly as the above described for cell lines and PBMCs samples.

Upon RNA elution, the samples were immediately placed on ice and the RNA concentration was measured in the Nano Photometer (IMPLEN, United Kingdom). $A_{260/280}$ ratio represent protein contamination, wherein values superior to 1.7 are good and relate with no protein contamination [174], [175]. RNA extracted samples could be stored at -80ºC until further use.

3.2.1.5 Agarose gel electrophoresis

Gel electrophoresis technique allows nucleic acids fragments separation based on their respective length, and thereby enable extracted RNA integrity analysis.

Firstly, gel electrophoresis apparatus was set up and gel was prepared with an agarose concentration appropriate. A solution of 40 mL 1× tris-acetate-EDTA (TAE) buffer with 1% agarose was mixed and heated up until agarose dissolution. Solution containing flask was carefully cooled under running water, 2 μL of Xpert Green DNA Stain 20000× (GRiSP, Portugal) was added to the mix and placed into the gel tray and wait up to polymerization. RNA samples for gel electrophoresis were prepared with 200 ng of extracted RNA, 2 μL of 10× loading buffer (Takara, Japan) and volume was adjusted to 10 μL with Mili-Q water. In first place, 4 μL of molecular weight GRS Ladder 1kb (GRiSP, Portugal) and 10 μL of the RNA samples are loaded into the sample wells, and the gel runs at 120 V for 40 min. Gel was further visualized using UV light exposure in UVITEC Cambridge UV chamber (UVITEC Cambridge, United Kingdom).

RNA integrity was analysed by the identification of 18S and 28S ribosomal RNA bands in each RNA sample profile [178].

3.2.1.6 Reverse transcriptase quantitative PCR (RT-qPCR)

First-Strand cDNA synthesis and qPCR assays were performed with miRCURY LNA RT Kit and miRCURY LNA SYBR® Green Kit, respectively. Appropriate primers belonging to miRCURY LNA miRNA PCR assay was applied into qPCR assays, and the experiments proceeded based on the protocols and information present on corresponding kit handbooks. The miRCURY LNA PCR kits use a locked nucleic acid (LNA) technology, in which RNA analogues have their ribose ring in an ideal configuration for Watson-Crick binding. This technology provides high thermal stability upon hybridization with complementary strands, and also a more sensitive and specific miRNA detection. Signature miRCURY qPCR QuantiNova DNA polymerase has a hot-start antibody mediated mechanism that allows enzyme activation only at certain temperatures, preventing nonspecific qPCR products and primer-dimers, for a more accurate quantification.

For PBMCs extracted RNA, 200 ng of total RNA was used for cDNA synthesis, however, in the case of plasma extracted RNA, 0.56 μL of RNA sample was used due to low RNA concentration in plasma. Reverse transcription reactions for each sample were prepared in a 0,2 mL PCR tube on ice, comprising 1 μL of 10× miRCURY RT enzyme mix with reverse transcriptase and poly(A) polymerase enzymes, 2 μL of 5× miRCURY SYBR® Green RT reaction buffer containing reverse transcription primers, Mg^{2+} and deoxyribonucleotide triphosphates (dNTPs), corresponding volume for 200 ng RNA for PBMC, or 0.56 μL for plasma RNA, and finally RNase-free water is added until solution made up to 10 μL. Samples were placed in the T100 Thermal Cycler (Bio-Rad, USA), where initially incubated at 42 ºC for 60 min for the reverse-transcription step, followed by a 5 min 95 ºC step for reaction inactivation, and finally 4 ºC for storage. cDNA samples could directly advance to qPCR or be stored at -20 ºC.

In qPCR assay preparation, total RNA from PBMCs was diluted 1:60/1:30/1:15 with RNase-free water, although total RNA from plasma was diluted 1:30/1:15/1:5/pure with RNase-free water as well. Multiple master mixes were prepared comprising the different primers in study, and each sample included 5 μL of 2× miRCURY SYBR® Green Master Mix containing QuantiNova DNA polymerase, reaction buffer and dNTPs, 1 μL of specific primer mix, 3 μL of template cDNA, and RNase-free water until reaching a 10 μL total. Sample setup was prepared in a 96-well PCR plate according to the pre-designed template, including non-template controls (NTC). Each sample was made in duplicate and tested for two housekeeping miRNAs (miR-103a-3p and miR-191-5p), as well as for the chosen NSCLC related miRNAs (miR-21-3p, miR-21-5p, miR-92b-5p, miR-150-3p, miR-155-3p, miR-155-5p, miR-181a-5p and miR-3662). After PCR plate set up, the plate was centrifuged at 1500 rpm for 1 min and positioned in a CFX Connected Real-Time PCR Detection System (Bio-Rad, USA). Cycling conditions for qPCR involved an initial reaction heat activation for 2 min at 95ºC, followed by 2-step cycling comprising a denaturation during 10 sat 95ºC and a further annealing/extension for 60 s at 56ºC. Previous steps were repeated for 40 cycles, and the corresponding software was used for data collection and subsequent analysis.

Later, qPCR data results were treated via $2^{-\Delta\Delta Ct}$ method for analysis of miRNA expression in NSCLC samples relatively to a healthy sample. In the stated equation, $\Delta\Delta Ct$ represents:

$$\Delta\Delta Ct = (Ct_{miRNA} - Ct_{housekeeping\ miRNA})_{NSCLC} - (Ct_{miRNA} - Ct_{housekeeping\ miRNA})_{Healthy}$$

Through $2^{-\Delta\Delta Ct}$ method, samples were normalized to housekeeping results and afterwards, compared between NSCLC samples and healthy ones.

3.2.2 MB characterization and interaction studies

3.2.2.1 MB design

MBs were designed for the targeting of miR-21-3p and miR-21-5p. As explained in chapters 1.4.1 - Structure and features and in 1.5.1 - Förster resonance energy transfer (FRET), MB miRNA-based detection approaches use FRET phenomenon to give a fluorescent signal upon MB hybridization with specific miRNA, due to donor and acceptor separation.

To the equivalent miR-21-3p and miR-21-5p DNA sequences, were added to each 5' and 3' ends six nucleotide CG rich sequences, in order to form a stable duplex stem that closes the loop region, and subsequently form the MB characteristic configuration.

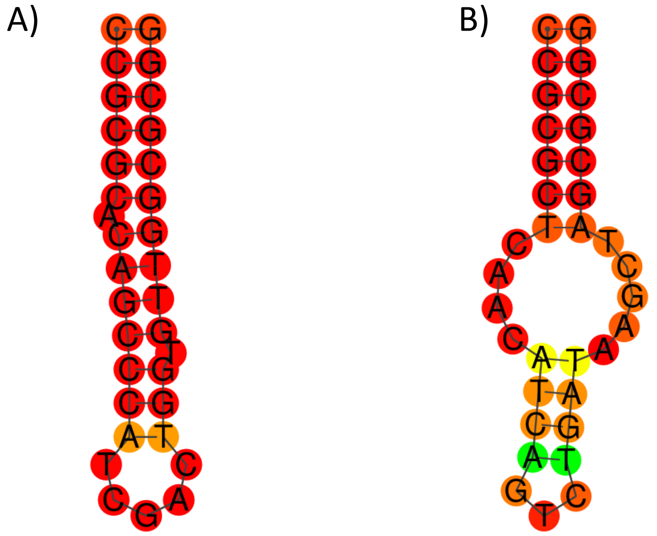

Figure 12. Predictive base-pairing configuration of designed MBs. **A)** MB for miR-21-3p and **B)** MB for miR-21-5p detection.

Figure 12 shows a computational structure prediction for MBs targeting miR-21-3p and miR-21-5p. At the end of each MB stem strand was paired a donor (fluorophore) and an acceptor (quencher). The fluorophores used were FAM with excitation (λ_{ex}) and emission (λ_{em})

wavelengths at 495 nm and 520 nm, respectively, and HEX with λ_{ex} = 535 nm and λ_{em} = 556 nm. All designed MBs had included the BHQ1 quencher.

3.2.2.2 Synthetic sequences preparation

Previous MBs and miRNA synthetic sequences in chapters 3.1 - Materials described in Table 2 were acquired from Eurofins (Eurofins Genomics, Luxembourg) and ALS Oligonucleotides (Viseu, Portugal). All the oligonucleotides were acquired with purification through high performance liquid chromatography (HPLC), and quality ensured via optical density (OD) measurement by matrix-assisted laser desorption ionization - time-of-flight (MALDI-TOF) mass spectrometry.

MBs and miRNA synthetic sequences arrived in lyophilized format, whereupon MB sequences were resuspended in 100 μL of Mili-Q water, and miRNA ones were diluted in DEPC-treated water. Sequence concentration were determined by absorbance in the Evolution™ 201/220 UV-Visible Spectrophotometer (Thermo Fisher Scientific, USA). A 1 mL solution with 1:1000 dilution of the sequence was prepared and moved into a quartz cuvette. Absorbance was scanned from 200 nm to 400 nm, and the value of 260 nm band was applied for sample concentration determination through the equation:

$$A_{260} = \varepsilon \times l \times c$$

The described equation enunciates Beer's law, where A_{260} is the absorbance value for the 260 nm peak, ε is the extinction coefficient from the sample, l represents the cells path length, and c is the concentration. After concentration values were calculated, MB and miRNA samples were stored at -20ºC until further experiments.

3.2.2.3 FRET-melting experiments

FRET principles are above explained in chapter 1.5.1 - Förster resonance energy transfer (FRET). Furthermore, FRET-melting and reverse FRET-melting assays allowed MB structure and dynamics study, via fluorescence monitoring associated with temperature variation.

For MB T_m determination, two solutions of 0.2 μM MB were prepared, one in 1× PBS and the other in 10 mM lithium cacodylate at pH 7.2. Firstly, MB solutions were incubated for 3 min at 95 ºC and then cooled down at room temperature. Described annealing step is important for MB folding into their native structure, by disuniting unfavorable intermolecular interactions and potential MB aggregates. 25 μL of annealed MB solutions were added, in duplicate, on each well of a 96-well PCR plate, which were placed in the CFX Connected Real-

Time PCR Detection System (Bio-Rad, USA), equipped with a FAM (λ_{ex} = 495 nm; λ_{em} = 520 nm) and a HEX (λ_{ex} = 535 nm; λ_{em} = 556 nm). MB samples were heated up to 95ºC and further cooled down to 25 ºC in the following reverse FRET-melting step, wherein fluorescence was measured during the entire assay. Fluorescence output data were normalized and fitted to Boltzmann distribution using OriginPro2016. MB T_m was calculated based on the corresponding temperature value to half of the total reached fluorescence [200].

Interaction studies between MBs and synthetic miRNAs sequences were also carried out by FRET and reverse FRET-melting assays. MB structure profile was studied in presence of their corresponding miRNAs, as well as for mismatching miRNAs. Solutions containing MB and the specific miRNA were prepared in a broad range of different concentrations and MB/miRNA ratios, and then run in the thermocycler for posterior MB melting curve analysis.

3.2.2.4 CD Spectroscopy

CD spectroscopy was applied to explore the conformational isomerization and structure characterization of DNA MBs. MB1 21-3p and MB1 21-5p solutions were prepared at a concentration of 10 μM in 1× PBS and 10 mM lithium cacodylate, along with MB2 21-3p and MB3 21-3p were prepared at the same concentration in 1× PBS.

The MB samples were annealed as previously described, and further transferred to a 1-mm path-length quartz cuvette which was placed in a Jasco J-815 spectropolarimeter (Jasco, USA), using a Peltier-type temperature control system (model CDF-426S/15). CD spectra acquisitions were performed at 20 ºC with a 200-340 nm spectral scan range, scan speed of 200 nm/min, 1 nm bandwidth, and 1s integration time over 4 accumulations. CD-melting assays were also executed for MB denaturation study and ellipticity (dmeg) was analysed from across different temperatures, ranging from 20-100 ºC with a heating rate of 2 °C/min, while monitoring the ellipticity at 274 nm.

Data was converted into fraction folded (θ) plots using the following equation:

$$\theta = \frac{CD - CD_{\lambda}^{min}}{CD_{\lambda}^{max} - CD_{\lambda}^{min}}$$

where CD is the ellipticity of the monitored wavelength at each temperature and CD_{min} and CD_{max} are the lowest and highest ellipticity, respectively. Data was fitted to a Boltzmann distribution (OriginPro 2016) and the T_m was determined.

3.2.2.5 NMR Spectroscopy

MB structural and interaction studies were carried out via NMR spectroscopy. Standard ^1H NMR spectra were recorded on a Bruker Avance III 600 MHz spectrometer equipped with a

QCI CryoProbe at 25 ºC. The NMR zgesgp pulse sequence was used to suppress the water signal. A 200 μL of MB1 21-3p and MB1 21-5p solutions were prepared in Mili-Q water, comprising 50 μM of MB, 10 mM lithium cacodylate, and supplemented with 10% of heavy water (D_2O). Previous solutions were set up in a 3mm NMR tubes and annealed at 95 ºC.

MB1 21-3p NMR spectra were acquired at 25 ºC, 40 ºC and 60 ºC. Posteriorly, NMR titration with Mg^{2+} was performed by adding increasing amounts of $MgCl_2$ to the 3 mm tube, corresponding to the concentrations: 50, 100, 200, 300 and 500 μM. MB1 21-5p spectra were also acquired at the referred temperatures for the MB alone and MB with miR-21-5p synthetic sequence. All spectra were acquired and processed with the software Topspin 3.1.

3.2.2.6 SDS-PAGE electrophoresis

SDS-PAGE electrophoresis procedure was used to study MB-miRNA hybridization through molecular mass separation. MB1 21-3p and MB2 21-5p, were added to their corresponding miRNA sequences, were performed under the referred technique protocol.

Acrylamide gel 15% was prepared and placed in an electrophoresis chamber with a gel holder attached, and further filled with SDS-PAGE running buffer. Before sample loading, the gel ran for 20 min to gel wells cleanup. Three sets of samples were arranged for each MB, involving in each one 10 μM of matching miRNA, 10 μM of MB in study (MB1 21-3p and MB1 21-5p), 10 μM of MB with one equivalent of miRNA (10 μM), and 10 μM of MB with two equivalents of miRNA (20 μM). To the four solutions were added 15 % of sucrose. Thereafter, each set of solutions were incubated at the respective temperatures (25 ºC, 40 ºC and 60 ºC) for 10 min, to allow hybridization between MBs and miRNAs. Upon incubation, 20 μL of each sample were loaded into the gel according to a designed template, followed by the electrophoresis running step at 130 V for 1 h. The gels were carefully removed, dipped in fixing solution for 1 h, and then emerged in staining solution for 20-40 min for sample profile detection. An overnight staining step could be applied for better gel resolution.

3.2.2.7 Fluorescence assays

Fluorescence assays were essential for MB structural studies, hybridization optimal conditions screening, and the development of an *in situ* promising approach for miRNA detection. Additional information on the previous topics was reported in chapter 1.6 - *In situ* MB miRNA detection.

Regarding structural and hybridization dynamics of MB2 21-3p, the fluorescence studies were performed on a FluoroMax 4 fluorometer (HORIBA, Japan). 1 μM of MB2 21-3p was prepared, annealed as previously described, and then loaded into a high-precision quartz suprasil cuvette light path 10 mm × 4 mm (Hellma, Germany). Spectra measurement settings were applied in accordance with fluorophore HEX characteristics (excitation = 535 nm, emission range scan = 540-700), and spectra was acquired in a 25°C-95°C temperature range, and vice versa, with 3 average scans. Thereafter, 1 μM of miR-21-3p synthetic sequence was added and the same procedure was performed.

MBs optimal hybridization conditions were screened before biological assays. MB and MB + miRNA solutions with different MB concentrations were prepared in 0.2 mL PCR tube on ice, using 1×PBS. Samples were placed in a T100 Thermal Cycler (Bio-Rad, USA), where they passed through an initial annealing step at 95°C for 10 min, and a hybridization step involving different temperature and time ranges. Posteriorly, samples were pipetted into a 96 well microplate for fluorescence-based assays, carefully homogenized for 3 min, and fluorescence was measured in a SpectraMax Gemini XPS Microplate Reader (Molecular Devices, USA) and in a GloMax™ Explorer Multimode Microplate Reader (Promega, USA). Templates were designed regarding the different conditions in study, and for each condition, it was set a MB and a MB + miRNA well. Biological assays were performed under optimized conditions from screening experiments. MBs were tested with total RNA from cell lines and NSCLC-PBMCs, and also with qPCR products from the mentioned biological samples. Template designs always included a control sample with only MB. Solutions concerning MB and biological samples were prepared in ice and then loaded into a 96 well microplate for fluorescence-based assays. The plate was homogenized for 3 min, and fluorescence was measured at different temperatures up to 45 °C, until reaching fluorescence peak.

3.2.3 Statistical analysis

Data from assays comprising more than one sample was presented as mean ± standard error (SE). Statistics on quantitative RT-qPCR data for PBMC samples, and final fluorescence results for MB-miRNA detection via MB1 21-5p targeting miR-21-5p with total PBMC RNA, were analyzed in OriginPro2016 by Two sample t Test with standard errors (SE), where significant differences in between NSCLC and healthy populations with a 95% confidence interval ($P<0.05$) were also studied. Additionally, previously mentioned assays strength was examined in the medical statistics software MedCalc via receiver operating characteristic (ROC) curve analysis. This data evaluation allows determination of the ability to identify true NSCLC positive cases (sensitivity), true negatives (specificity), and discrimination robustness via the area under the curve (AUC) value.

CHAPTER 4 – Results and Discussion

4. Results and Discussion

In chapter 4 - Results and Discussion, the data obtained are presented and forwardly discussed. It is divided into separate parts, starting by biological samples processing reports, and thereafter miRNA profile in NSCLC patients versus healthy volunteers, regarding the process from RNA extraction to RT-qPCR data processing. The third part accounts for used MBs biophysical characterization, followed by MB interaction studies with synthetic and biological samples in the final section.

Experiments data is arranged, displayed and further analysed. Results discussion attempt to find and explain the reasons behind each outcome, based on literature review. Thus, the connection between results and exploited paths allows us to logically understand the work sequence.

4.1 Biological samples processing

4.1.1 NSCLC and healthy population

Whole blood samples were collected from a NSCLC group and a healthy control group for plasma and PBMCs isolation. NSCLC group included multiple NSCLC diagnosed patients at stages I-IV from CHUCB hospital. The healthy control group is composed of healthy individuals, with no medical NSCLC associated conditions.

Table 3. NSCLC and healthy control testing groups of the study

	NSCLC cases (n=59)	**Controls (n=22)**
Age	70.12	30.1
Sex		
Female	13	16
Male	46	6

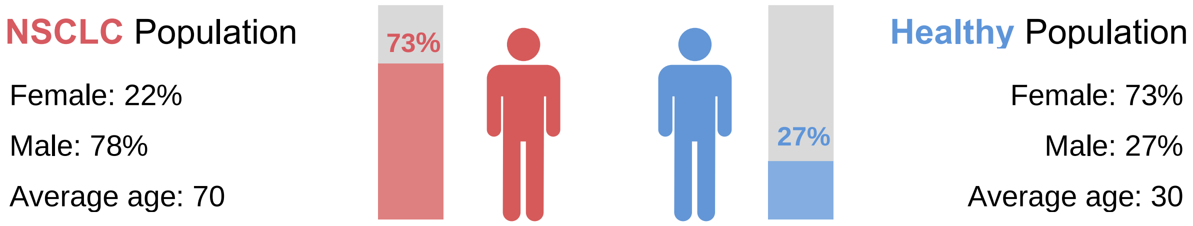

Figure 13. Statistical schematic on NSCLC and healthy control testing groups of the study.

Followingly work involved the participation of 81 individuals. Table 3 and Figure 13 resume participant numbers and statistics regarding this study. NSCLC group had a total of 59 participants (73% of total participants), with an average age of 70 years old, comprising 13 female (22%) and 46 male (78%) individuals. On the other hand, the health control group counted 22 participants, wherein 16 were female (73%), and 6 were male (27%), with an average age of 30 years old. Concerning NSCLC population, adenocarcinoma was the most predominant NSCLC subtype, and the majority of NSCLC cases were already in stage IV. Moreover, multiple NSCLC-characteristic mutations were identified among NSCLC patients, suchlike EFGR, ALK and KRAS, and more than half NSCLC population had smoking history.

4.1.2 Plasma hemolysis

A total of 372 plasma samples were collected among the NSCLC and healthy population. Usually, a single blood collection from an individual resulted in 2 samples of plasma divided in respectively labelled cryovials. Before storage at -80ºC, plasma hemolysis was always checked. Figure 14 show information concerning plasma hemolysis appearance and results.

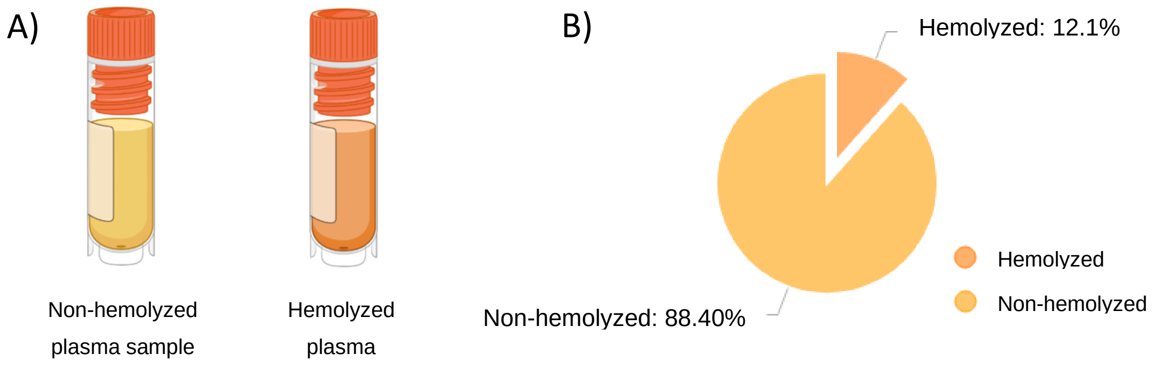

Figure 14. Plasma hemolysis. A) Visual aspect of a non-hemolyzed and a hemolyzed plasma sample. B) Plasma hemolysis measurement results.

Besides some plasma samples exhibited a visual characteristic reddish colour (Figure 14, A), which normally is proportional to hemolysis level, all plasma samples proceeded to hemolysis check through an A_{414} peak analysis. In case of an A_{414} peak superior to 0.2, the sample is considered hemolyzed [171]. Plasma hemolysis can result from incorrect blood collection procedures. The professionals in charge were responsible for the control of good practices in blood collection for plasma hemolysis prevention, accordingly to the Ethics procedure approved by CHUCB Ethical Committee (ref. 35/2019).

From the whole collected plasma samples, 45 displayed an A_{414} peak > 0.2, which means that 12.1% of all the plasma samples are hemolyzed (Figure 14, B), and further not eligible for experiments concerning miRNA profiling and quantification [171], [172].

4.1.3 PBMC count

PBMCs were isolated from whole blood samples from NSCLC and healthy groups. Throughout the separation process, PBMCs samples were treated with RBC lysis buffer for RBC removal, counted, and further divided into 1 million cells. The following Figure 15 presents a bar chart with data for PBMC count among the different groups.

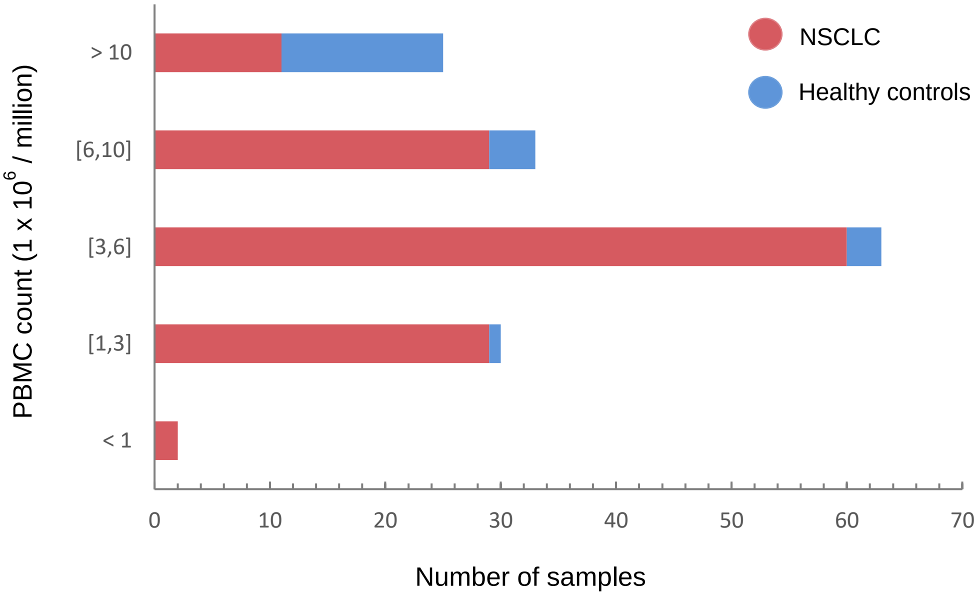

Figure 15. PBMC count among NSCLC and healthy groups collected samples. Almost every sample had the minimum PBMC number for further RNA extraction.

The amount of PBMC samples collected over the presented work was 153, including 22 from healthy individuals and 131 from NSCLC patients. Regarding PBMC isolation from the NSCLC group, the total number of samples include some distinct isolations for the same patient.

By analyzing Figure 15, more samples were collected from NSCLC patients relative to healthy individuals., apart from almost every sample had more than 1 million PBMCs, which is enough for RNA extraction. The majority of PBMC samples count for NSCLC group was between 3 and 6 million, with a considerable number of samples having 1 to 3 million, and 6 to 10 million. However, in the healthy control group, most of the samples had more than 10 million PBMCs. A higher number of PBMCs for the healthy control group in relation to NSCLC group could result from two main aspects. Foremost, the fact that the healthy group had a younger average age (~30 years) than the NSCLC group (~70 years), since elder individuals tend to have lower PBMC ratios due to age-related immune dysfunction. Moreover, besides the NSCLC group older average age, this group was constituted by NSCLC patients that a priori have a weaker immune system [232], [233].

Upon PBMC isolation, it was noticed that some PBMC pellets showed a soft red colour that could result from RBC contamination. In some cases, the RBC lysis buffer could not be that effective, or even the hemolysis level in the sample was quite high. Moreover, some patients demonstrated a red PBMC specific profile. PBMC samples from certain patients, despite the extraction procedure, always displayed a signature blood-red smooth colour. Red PBMC pellets were avoided for RNA extraction assays.

4.2 NSCLC miRNA profiling

4.2.1 RNA yield and quality

Total RNA was extracted from plasma and PBMCs from NSCLC patients and healthy individuals, as well as from A549 lung cancer line and NHDF healthy cell line for comparison purposes. Table 4 compiles RNA extraction results in plasma, PBMCs, and cell lines, wherein average RNA extracted values for plasma were about 12.64 ng/µL, although for PBMCs and cell lines, RNA amounts were considerably higher (78.11 and 968.1 ng/µL, respectively).

Table 4. Average RNA extraction results in plasma, PBMCs, and A549 / NHDF cell lines.

	Plasma	**PBMCs**	**Cell lines (A549 / NHDF)**
RNA concentration (ng/µL)	12.64	78.11	968.1
$A_{260/280}$ ratio		2.02	2.12

In PBMCs, RNA yield average was 78.11 ng/µL, and in cell lines was 968.1 ng/µL. $A_{260/280}$ ratio was also analyzed for extracted RNA samples, which indicated a mean value in PBMCs and cell lines of 2.02 and 2.12, respectively, concluding that RNA samples were not contaminated with protein [174], [175]. An optimization was performed in the RNA extraction protocol, concerning the RNA final elution step, which resulted in slightly higher RNA yields. After the full speed 5 min column centrifugation for membrane drying, the column was placed in the benchtop for 3 min for full membrane dry. Once the 14 µL of RNase-free water were added into the column for RNA elution, the column was placed at the benchtop for 1.5 min for total membrane soak.

Plasma RNA poor yields resulted from the overall low circulating RNA content in blood [234]. Cells RNA extraction efficiency was highly dependent on starting material quantity and characteristics, given that more concentrated or different kinds of pellets resulted in higher yields, but never surpassing the limit of cells (1 million). For example, 1 million cells from a cell line had higher RNA extraction ratios than 1 million of PBMCs, due to their size and structure. PBMC and cell line samples RNA quality and integrity were accessed by rRNA 28S and 18S band analysis through gel electrophoresis.

RNA quality from plasma was not able to be studied via gel electrophoresis due to the absence of rRNA 28S and 18S in plasma. rRNA 28S (~5 kb) and 18 (~2 kb) band appearance, definition and intensity are related to the overall quality of the mRNA population (including miRNAs) of the sample [177], [178].

As observed in further presented Figure 16, the usually obtained 28S/18S band profile for extracted RNA involved a slightly smeared band at about 4-3 kb for rRNA 28S and a well-defined band at 1.5-1 kb corresponding to rRNA 18S.

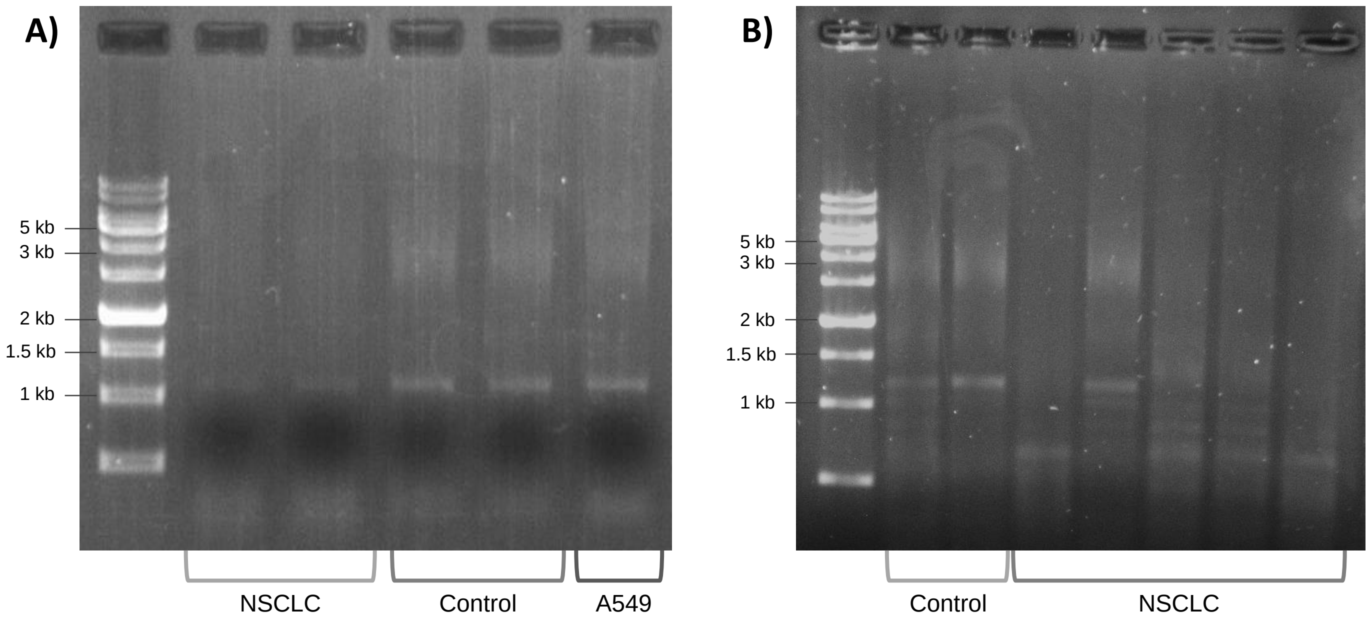

Figure 16. PBMCs and A549 extracted RNA quality. A) Characteristic electrophoresis gel of rRNA 28S/18 profile for extracted RNA from A549 cell line, NSCLC, and control PBMCs, before NSCLC sample collection modifications. B) Characteristic electrophoresis gel rRNA of rRNA 28S/18 profile for extracted RNA from A549 cell line, NSCLC, and control PBMCs after NSCLC sample collection modifications.

Earliest RNA extractions displayed a 28S/18S band profile for cell lines and PBMCs from healthy individuals, but regarding NSCLC samples, 28S/18S bands suggested poor integrity (Figure 16, A). Since the procedures were the same for cell lines and healthy PBMCs, the poor integrity of NSCLC patients' samples could be related to the blood collection and transportation. Blood samples quality is essential to hold RNA integrity, regarding sample storage and time until processing. The difference between NSCLC and healthy PBMCs isolation was related to the delay for NSCLC samples to be processed. NSCLC blood samples were collected in CHUCB at different times in the early morning and gathered by laboratory members in proper refrigerated conditions after 3-4h, which represent a long-time interval until processing that could compromise sample quality. Thus, NSCLC samples started to get picked up just a few moments after collection in the same location where the collections took place and transported to the laboratory for direct processing. Concerning the modifications about NSCLC samples collection just mentioned, extracted RNA from NSCLC PBMCs began to demonstrate integrity for a few NSCLC patients (Figure 16, B).

By analyzing the regular 28S/18S band profile for extracted RNA, it was demonstrated RNA integrity due to rRNA 28S/18S bands appearance in gel electrophoresis, although associated with some RNA degradation. 28S/18S rRNA bands showed up at a slightly lower molecular weight than expected, wherein rRNA 28S (~5 kb) band was located more around 4 kb, and rRNA 18S (~2 kb) near 1.5-1 kb. rRNA 28S smeared band profile also correlates with RNA degradation.

However, reasonable 28S/18S band profiles are commonly viewed in extracted RNA from culture cells, and in the presented studied most RNA samples were from PBMCs. 28S rRNA comprehends a configuration instability due to size and high degree of secondary and tertiary structures. Furthermore, 28S rRNA can encompass "hidden break" sequences that result in 28S rRNA processing into two shorter RNA species [235]. The RNA degradation profile could be related to the sample in study (PBMCs), and the 28S band smear could be connected to 28S intrinsic instability and possible fragmentation. 18S rRNA band remained defined and clear among samples that demonstrated RNA integrity. Notwithstanding degraded RNA previous conclusions, including rRNA 28S RNA degradation related profile, 18S rRNA constant band pattern implies intact RNA integrity for mRNAs, including miRNAs, and further minor PBMC sample RNA degradation.

Preserving RNA quality from human samples is challenging, and it is mainly related to sample physiological state and associated removal procedures. Results for RNA quality in NSCLC PBMCs indicated acceptable RNA integrity and quality in cell lines, PBMCS from most healthy individuals, and for some NSCLC patients. Additionally, results indicated low-scale degradation, and that the applied improvements in sample collection steps positively contributed to overall RNA quality from PBMCs.

4.2.2 RT-qPCR

Extracted RNA samples from plasma and PBMCs followed by cDNA synthesis and posterior qPCR experiments. In qPCR assays, miRNAs 103a-3p and 191-5p were chosen as housekeeping genes, and the NSCLC-related miRNAs 21-3p, 21-5p, 92b-5p, 150-3p, 155-3p, 155-5p, 181a-5p and 3662 were profiled among NSCLC and healthy individuals' samples.

Initially, all the miRNAs primers were tested to optimize qPCR conditions related to primer and sample concentration, including correct primer on miRNA detection. The first qPCR assay was performed by following respective miRCURY LNA SYBR® Green Kit handbook instructions, where cDNA from plasma was diluted 1:30, from PBMCs was 1:60 and 1 µL of each primer was used in master mix preparation.

Results showed that miRNAs were detected in PBMCs, but not in plasma. Housekeeping miRNAs 103a-3p, 191-5p, and NSCLC-miRNAs 21-3p, 21-5p, 181a-5p and 3662 amplified in NTC at a close Ct to sample Ct amplification, proposing contamination on qPCR preparation or used solutions, or primer dimers resulting from unspecific primer connection and further amplification. Further optimization qPCR assays were conducted to enhance miRNA plasma detection and NTC amplified miRNAs proper functioning. Plasma cDNA concentrations were tested between 1:10, 1:5 and pure, but no significant amplifications were achieved for the miRNA panel in plasma samples. Besides poor RNA yields from plasma referred in chapter 4.2.1 - RNA yield and quality, several aspects also play a role in plasma miRNA detection. Low miRNA recovery levels from plasma could be connected to initial sample quality collection, respective proper processing, and insufficient amount of starting material in the RNA extraction step [234], [236].

NTC amplifying miRNA primers were applied at lower concentrations (1:2, 1:5 and 1:10) in order to understand if the NTC amplification occurred due to contamination or primer dimerization. When there is a difference of about ~10 Cts between the sample in study and the respective NTC, the non-specific NTC amplification results mainly from primer dimerization, and the NTC amplification can be ignored for further qPCR assay validation [237], [238]. A ~10 Ct difference were reached among NTC and samples for the NTC amplifying miRNAs when primer dilutions were 1:10 for both housekeeping miRNAs 103a-3p and 191-5p, 1:5 for miR-21-3p, 1:2 for miR-21-5p, 1:2 for miR-181a-5p, and 1:2 for miR-3662.

Based on previous results, qPCR experiments were further performed on RNA from healthy and NSCLC PBMCs, and from A549 and NHDF cell lines, employing the previous input RNA and primers optimized concentrations.

Preliminary miRNA screening on NSCLC cell line A549 and healthy cell line NHDF results were not normalized due to inadequate used housekeeping genes. Housekeeping miRNAs 103a-3p and 191-5p were not suitable for normalization of qPCR miRNA detection results using RNA from the employed cell lines, showing high amplification differences between cell lines and off-range Ct values for appropriate housekeeping genes. However, unnormalized miRNA screening results showed significant differences in A549 miRNA profile, in comparison with NHDF.

Concerning PBMC miRNA expression analysis, a preliminary miRNA screening was conducted comprising 12 healthy control individuals and 23 NSCLC patients. For miRNAs 21-5p and 150-3p, tested samples were increased up to 20 healthy controls and 48 NSCLC patients for miR-21-5p, and 19 healthy controls and 47 NSCLC patients for miR-150-3p. Cell lines and PBMCs qPCR Ct raw data were further processed via $2^{-\Delta\Delta Ct}$ method, considering the value 1 for miRNA expression standardization in healthy controls, and the assay outliers elimination throughout data processing. Statistics were assessed by result significance and receiver operating characteristic (ROC) curve sensitivity, specificity, plus area under the curve (AUC) analysis. miRNA expression results are further discussed down below pursuant chapter 1.3.3 - NSCLC miRNAs in study, focusing on miRNA selected panel roles in NSCLC, and corresponding connection to the achieved outcomes.

Table 5. RT-qPCR non-normalized mean miRNA amplification values in NHDF and A549 cell lines

miRNAs in study	Ct amplification mean (NHDF)	Ct amplification mean (A549)
miR-21-3p	35.80	27.75
miR-21-5p	16.66	14.59
miR-92b-5p	31.47	27.35
miR-150-3p	30.58	28.71
miR-155-5p	31.79	30.69

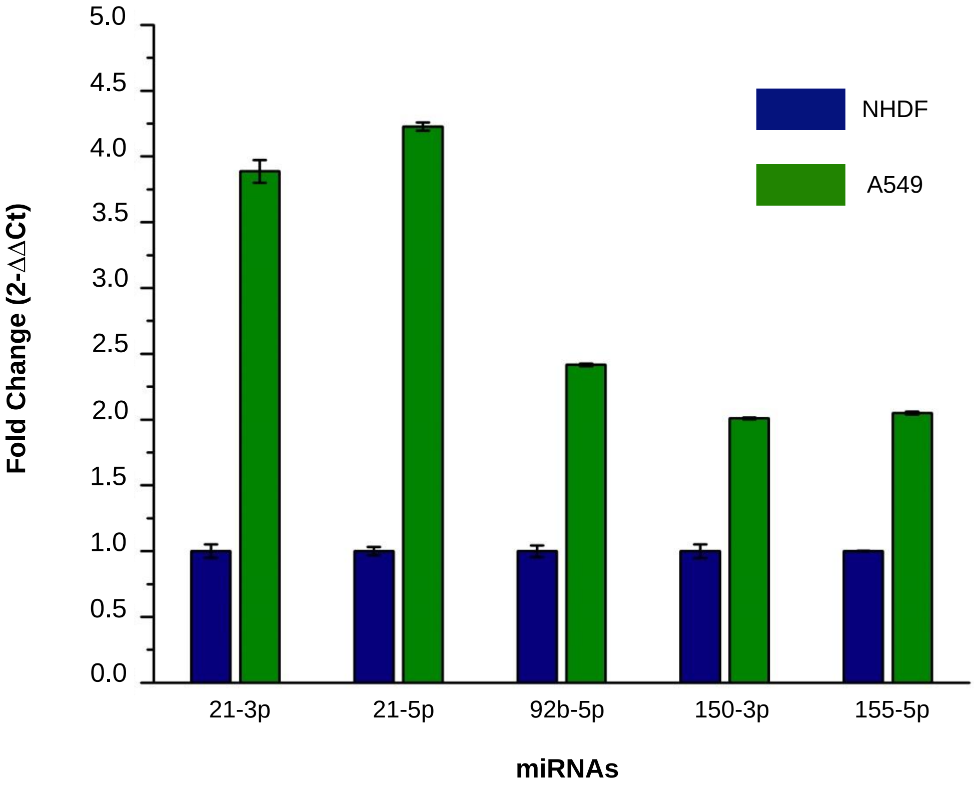

Figure 17. miRNA selected-panel relative expression in A549 versus NHDF cell line. Housekeeping gene normalization was not applied to cell line qPCR data. A549 miRNA expression values were determined from qPCR assays duplicate measurements, and standardized relatively to NHDF a control expression value 1 (mean ± SE, n=2).

Table 5 presents raw RT-qPCR Ct means of miRNAs 21-3p, 21-5p, 92b-5p, 150-3p, and 155-5p screening, and Figure 17 depicts these miRNA expressions in A549 over NHDF profile. 21-3p miRNA expression fold change in NSCLC A549 cell line was 3.89 higher than in NHDF healthy control cell line. Respective miR-21 passenger strand, miR-21-5p, was also up-regulated in A549 cell line, with a fold change value of 4.2 above NHDF miR-21-5p expression. Up-regulated expression results for miR-21 in NSCLC cell line A549 attend to Zhou *et al.* and Yan *el al.* work, which confirmed miR-21 overexpression in A549 cells associated with NSCLC progression [139], [239]. Concerning miR-92b-5p expression, a 2.42-fold change was obtained over NHDF cell line. A miR-92b overexpression in A549 is supported by the research outcomes of Yan *et al.*, where miR-92b was up-regulated in A549 cell lines, acting as an onco-miR in cell growth regulation processes and chemoresistance development [141], [144]. miR-150-3p expression in A549 cell lines was 2.01 higher compared to NHDF control cell line expression. Prior studies verified miR-150 up-regulation in A549 cell lines associated with NSCLC proliferation and metastasis mechanisms [145], [146]. Regarding miR-155 expression analysis, miR-155-5p was up-regulated in A549 cell lines with a 2.05-fold change upon control cell line expression. Studies proved miR-155 up-regulation in A549, along with a proportional increase in expression related to chemotherapy resistance [240], [241]. Furthermore, Lin *et al.* study on miR-155-5p expression role in A549 cell lines indicated inhibition of cell migration and invasion, demonstrating miR-155 multi-functional role on NSCLC [242].

Table 6. RT-qPCR mean miRNA amplification values in control and NSCLC groups

miRNAs in study	Ct amplification mean (Control)	Ct amplification mean (NSCLC)
miR-21-3p	26.18	24.66
miR-21-5p	16.58	15.76
miR-92b-5p	31.62	31.73
miR-150-3p	27.10	27.33
miR-155-3p	34.92	33.01
miR-155-5p	21.76	21.44
miR-181a-5p	22.06	21.04
miR-3662	36.79	36.25

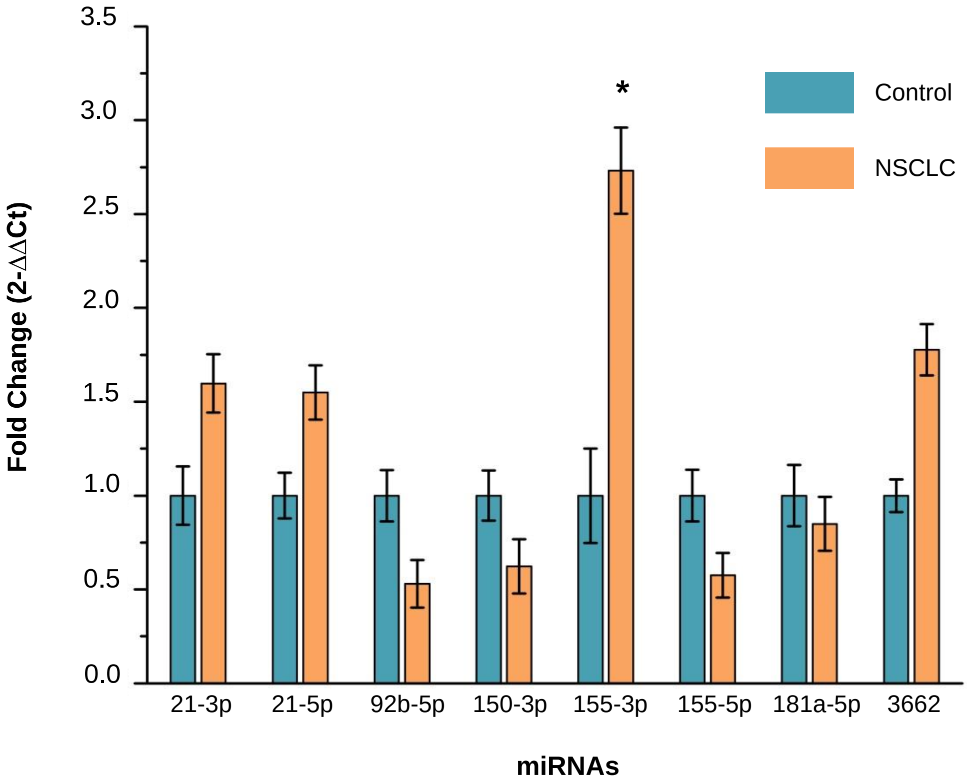

Figure 18. Selected-miRNA relative expression in NSCLC and healthy control PBMCs. Data were normalized to housekeeping miRNAs 103a-3p and 191-5p, and further NSCLC miRNA expression calculated relatively to a healthy control expression value of 1 (mean ± SE. *P<0.05). Data population after outliers exclusion for the multiple miRNAs was: 21-3p (control n=11, NSCLC n=20); miR-21-5p (control n=18, NSCLC n=44); miR-92b-5p (control n=12, NSCLC n=23); miR-150-3p (control n=19, NSCLC n=46); miR-155-3p (control n=10, NSCLC n=23); miR-155-5p (control n=10, NSCLC n=21); miR-181a-5p (control n=11, NSCLC n=16); miR-3662 (control n=8, NSCLC n=14).

Above displayed Table 6 exhibits the direct RT-qPCR Ct mean values for miRNA screening in NSCLC and control PBMCs, and Figure 18 illustrates normalized miRNA profiling results in PBMCs from the same group of samples.

miR-21-3p showed an up-regulated tendency in PBMCs from NSCLC patients with a 1.6-fold change, 100% sensitivity, 36.4 specificity, and an AUC of 0.636 (Figure 19, A). miR-21-5p also had demonstrated propensity to be up-regulated as well in NSCLC PBMCs, which exhibited a 1.55-fold change value over healthy miR-21-5p regular expression, with 77.3% sensitivity, 55.6% specificity, and 0.621 AUC (Figure 19, B). Besides the emerging PBMC interest as a target for miRNA profiling in NSCLC diagnosis, some studies already acknowledged the overexpression of miR-21 in NSCLC PBMCs, along with the intrinsic relation of this PBMC biomarker miRNA with NSCLC potential diagnosis [243], [244]. Achieved results were congruent about miR-21 up-regulation in A549 cell line and NSCLC PBMCs samples, which corroborate the role of miR-21 as an onco-miR that interplay in oncogenic pathways, and subsequently stimulate NSCLC development [135]–[139].

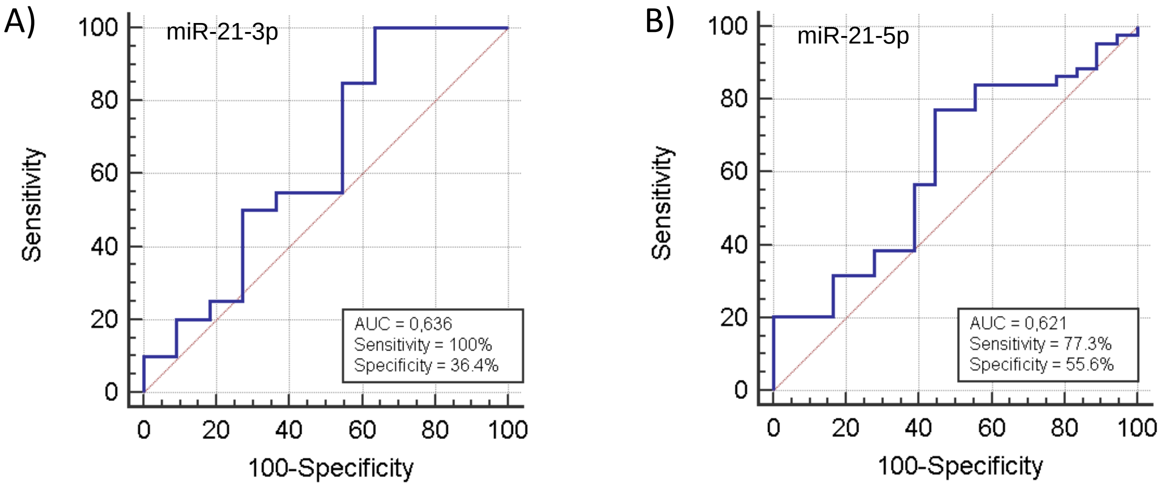

Figure 19. ROC curve analysis on miR-21 RT-qPCR profiling in healthy and NSCLC PBMCs. A) miR-21-3p ROC curve. B) miR-21-5p ROC curve.

92b-5p miRNA showed a downregulated inclination with a 0.53-fold change value in comparison with healthy controls, comprising 60.9% sensitivity, 75% specificity, and 0.63 AUC (Figure 20, A). miR-92b levels in NSCLC tissues are up-regulated according to Yan *et al.*, which are correlated with its' inherent oncogenic role in NSCLC evolution [141]–[144]. Nevertheless, in conformity with Liu *et al.* work, miR-92b may also behave as a tumor suppressor in NSCLC by decelerating metastasis processes [142]. Odd miR-92b-5p downregulation in NSCLC PBMCs oppose A549 overexpression, which could be linked with tumor suppression activity, but also with the unique PBMC miRNA expression setup that could differ from other samples. Pursuant multiple studies, PBMC miRNA expression profile is not relatable with cell lines profile, tissue, and blood samples from the condition in study [245]–[247]. In addition, according to Ma *et al.*, there is no overlap between the miRNA expression profile in PBMCs with the profile in NSCLC tissue and extracellular fluids [132]. Moreover, it is relevant to notice that only the miR-92b-5p strand was screened. Pre-miRNA complementary strand 92b-3p could present a dissimilar expression profile than miR-92b-5p in A549 and NSCLC PBMCs screening assays [113], [114].

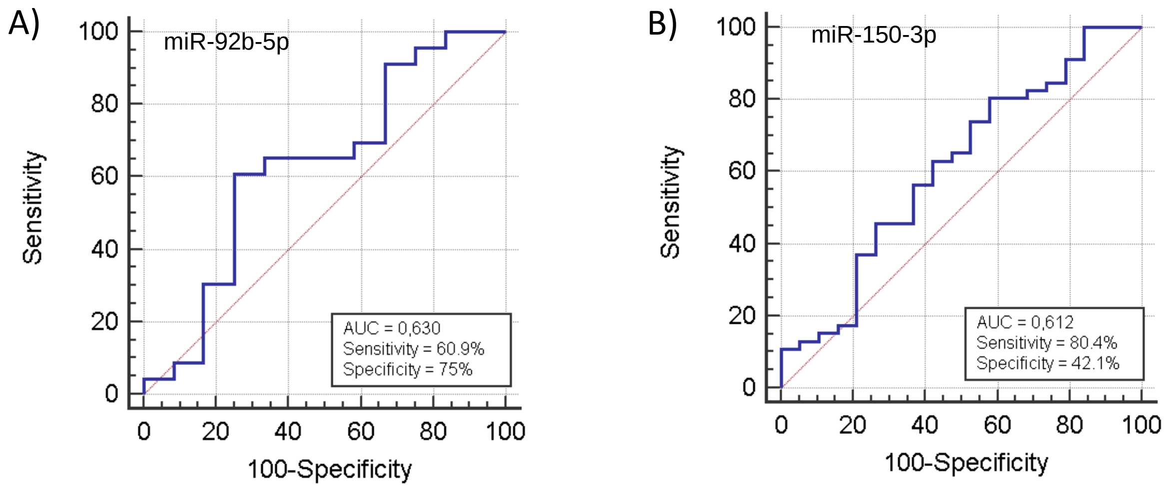

Figure 20. ROC curve analysis on miRNAs 92b-5p and 150-3p RT-qPCR profiling in healthy and NSCLC PBMCs. A) miR-92b-5p ROC curve. B) miR-150-3p ROC curve.

Regarding PBMCs results, miR-150-3p revealed an under-expressed trend in NSCLC, displaying a 0.63-fold change with 80.4% sensitivity, 42.1% specificity, and an AUC value of 0.612 (Figure 20, B). Zeng *et al.* studies demonstrated a slightly higher, but non-significant overexpression of miR-150 expression between NSCLC and healthy PBMCs, even though capable of significantly differentiate NSCLC stages [248]. Regardless reported miR-150 overexpression in NSCLC tissue and in the above reported A549 cell line, noted miR-150-3p down-regulation results in NSCLC PBMCs does not support the general miR-150 oncogene comportment in NSCLC [145]–[148]. However, this variation may result from a particular PBMC miRNA profile that does not overlap the expression profile of other samples, or through the interconnection of the already reported passenger strand miR-150-5p tumor suppressor activity in NSCLC, with miR-150-3p perchance similar functions in NSCLC [132], [149], [245]–[247].

155-3p miRNA screening in NSCLC PBMCs revealed a significant ($p<0.05$) 2.73 up-regulation value relatively to control PBMCs expression, with 73.9% sensitivity, 72.7% specificity, and a 0.711 AUC number (Figure 21, A). On the other hand, miR-155-5p expressed a down-regulated proclivity in NSCLC PBMCs with a 0.58-fold change value comparatively to the healthy control, 95.5% sensitivity, 36.4 specificity, and an AUC of 0.674 (Figure 21, B). Based on Salem *et al.* research results in NSCLC PBMC miRNA screening, miR-155 was under-expressed in NSCLC patients before chemotherapy start, and further considered a poor prognosis biomarker in NSCLC PBMCs [243]. Overexpression of miR-155-3p in NSCLC PBMCs support previously reported A549 expression findings, as well as multiple intrinsic oncogene functions, and miR-155 up-regulated relevant prognostic values in NSCLC tissue, plasma, serum and cell lines [153]–[160]. Although, miR-155-5p down-regulated profile in NSCLC PBMCs may be interconnected with no chemotherapy employment and early NSCLC diagnosis [243]. Considering the possible relevant role of the specific PBMC miRNA profile in the divergent miR-155-3p and miR-155-5p PBMC expression, corroborated by the up-regulation of miR-155-5p in A549 cell lines and posterior down-regulation in NSCLC PBMCs, collected miR-155 results also exhibit a congruent example of miRNA strands 3p and 5p expression imbalance [113], [114], [132], [245]–[247]. miR-155 is a multi-functional miRNA in NSCLC and perhaps, miR-155-3p strand is majorly linked to NSCLC tumorl development mechanisms, and the miR-155-5p passenger strand takes most part in NSCLC drug resistance pathways.

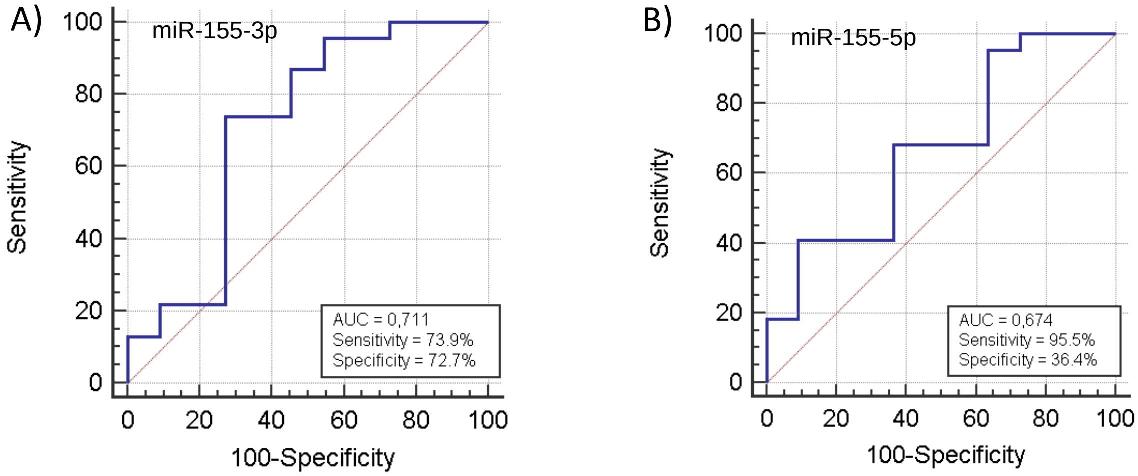

Figure 21. ROC curve analysis on miR-155 RT-qPCR profiling in healthy and NSCLC PBMCs. A) miR-155-3p ROC curve. B) miR-155-5p ROC curve.

The miRNA 181a-5p displayed a down-regulated leaning in NSCLC PBMCs with a 0.85-fold change versus healthy controls, 22.2% sensitivity, 100% specificity, and 0.53 AUC (Figure 22, A). Screening studies documented that miR-181a and respective 5p strand were mostly down-regulated in NSCLC tissue, serum, and A549 cell lines [163], [164], [166]. NSCLC PBMCs miR-181a-5p under expression concord with the overall low expression in NSCLC samples, along with tumor suppressor role of miR-181a in NSCLC [162]–[166].

miR-3662 NSCLC PBMC expression depicted a 1.78-fold change up-regulated tendency over healthy controls, with 73.3% sensitivity, 60% specificity, and a 0.633 AUC value (Figure 22, B). Recent NSCLC diagnosis research appointed miR-3662 as a potential NSCLC circulating biomarker, as a result of miR-3662 overexpression in NSCLC plasma samples [167], [168].

Thereby, miR-3662 role in NSCLC development is still unclear. However, as reported by Chen *et al.*, miR-3662 plays a tumor suppressor role in hepatocellular carcinoma [169]. Observed miR-3662 up-regulation in NSCLC PBMCs attend stated overexpression in plasma, and suggest a miR-3662 oncogene function in NSCLC.

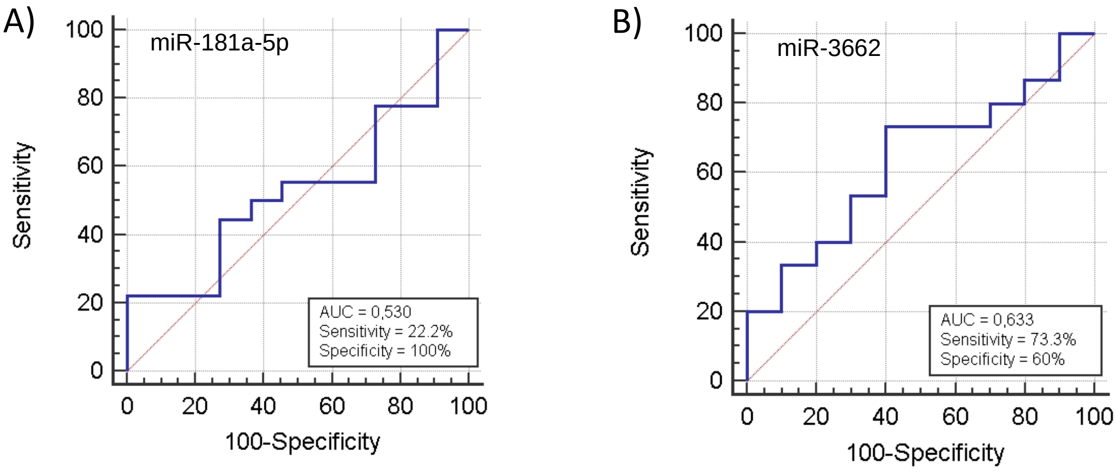

Figure 22. ROC curve analysis on miRNAs 181a-5p and 3662 RT-qPCR profiling in healthy and NSCLC PBMCs. A) miR-181a-5p ROC curve. B) miR-3662 ROC curve.

PBMC miRNA expression statistical aftermath denotes differences for the studied miRNAs among the NSCLC and healthy group. miRNAs 21-3p, 21-5p, 155-3p and 3662 displayed an overexpressed tendency in NSCLC PBMCs. On the other hand, miRNAs 92b-5p, 150-3p, 155-5p and 181a-5p demonstrated a down-regulated predisposition in PBMCs from NSCLC patients. Results on miR-155-3p expression indicated the largest fold change difference reported in this study, with a statistically significant value ($p<0.05$) of 2.73 over the healthy control group expression, purporting relevant differences among NSCLC and healthy individuals. ROC curve analyzed the miRNA expression results capacity to identify NSCLC and non-NSCLC individuals. Sensitivity values show the ability to correctly identify positive NSCLC cases, and specificity to recognize true negatives. AUC is a useful value that quantifies the aptitude of the miRNA in study to describe good discrimination in between studied condition. miRNAs 21-5p, 92b-5p 155-3p and 3662 appeared to acceptably differentiate positive and negative cases. miR-181a-5p revealed a low sensitivity value (22.2%), which relates to its' lack of ability to diagnose true NSCLC cases (sundry false negatives). Low specificity numbers were achieved by miRNAs 21-3p, 150-3p, and 155-5p, showing an inadequate diagnosis of real NSCLC negative cases (various false positives). The vast majority of miRNAs in study demonstrated AUC values above 0.6, which implies a poor NSCLC diagnosis discrimination power. However, miR-155-3p proved an acceptable discrimination capacity with a 0.711 AUC, and on contrary, miR-181a-5p a deficient discrimination competence with an AUC value of 0.53.

miRNAs 21-3p and 21-5p strands were picked for further MB design, development, and detection assays, due to their up-regulation propensity in NSCLC PBMCs, and higher concentrations in samples by comparison with the other miRNAs, as evidenced by the lower miR-21-3p and 5p Ct values (24.66 and 15.76, respectively. Table 6) in qPCR experiments. Despite 21-5p being the most studied strand regarding NSCLC and other health conditions, the passenger strand (miR-21-3p) were also selected for further assays, not only because of the respective up-regulated profile in NSCLC PBMCs, but considering its promising relevant role in NSCLC diagnosis [115], [249].

4.2.3 Clinical analysis

miRNAs 21-3p and 21-5p expression in NSCLC was linked with patients' stage, mutations and smoking background. Thus, an interconnection between miR-21 expression and the NSCLC profile was studied.

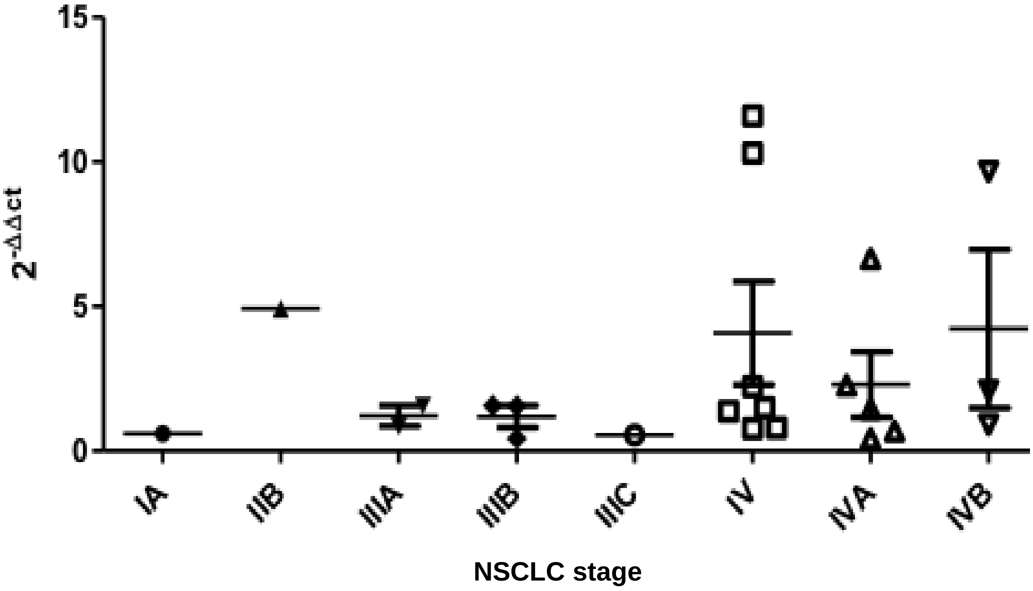

Figure 23. PBMC miR-21-3p expression among NSCLC stage. IA (n=1); IIB (n=1); IIIA (n=2); IIIB (n=3); IIIC (n=1); IV (n=7); IVA (n=5); IVB (n=3). RT-qPCR data is displayed in fold change (± SE).

Figure 23 exhibits miR-21-3p expression in NSCLC PBMCs versus NSCLC stage. Although lower NSCLC stages have a lower number of representative samples, a miR-21-3p overexpression tendency in PBMCs is visible in NSCLC IV stages. Moreover, NSCLC stage progression might be related to miR-21-3p up-regulation in PBMCs. Next presented Figure 24, A, analyses PBMC miR-21-3p expression relation with multiple NSCLC signature mutations. A high miR-21-3p expression is noted in BRAF NSCLC mutation, showing a potential miR-21-3p role in BRAF NSCLC mutation and connected mechanisms. Furthermore, more representative samples are needed in order to support this result. In Figure 24, B, it is perceptible that NSCLC patients who have smoking history display a slightly higher miR-21-3p expression over the ones that do never had connection with smoking. The miR-21-3p up-regulation in smoking patients could be able to discriminate smokers from non-smoker patients.

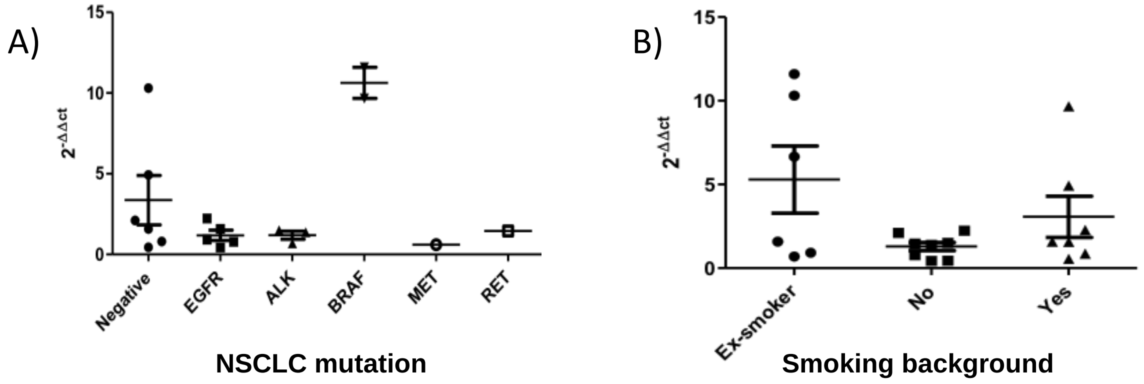

Figure 24. PBMC miR-21-3p expression among NSCLC mutations and smoking record. A) miR-21-3p expression versus NSCLC mutations. Negative (n=6); EGFR (n=5); ALK (n=3); BRAF (n=2); MET (n=1); RET (n=1). B) miR-21-3p expression versus smoking background. Ex-smoker (n=6); No (n=8); Yes (n=7). RT-qPCR data is displayed in fold change (± SE).

Concerning miR-21-5p expression in NSCLC PBMCs, is visible in Figure 25 a miR-21-5p up-regulation proclivity throughout worse NSCLC stages, such as miR-21-3p. Despite miR-21-5p overexpressed inclination in NSCLC advanced stages, earlier NSCLC stages have a little representative population, so for a more correct miR-21-5p expression discrimination among NSCLC patients, more NSCLC samples at stages I and II are required.

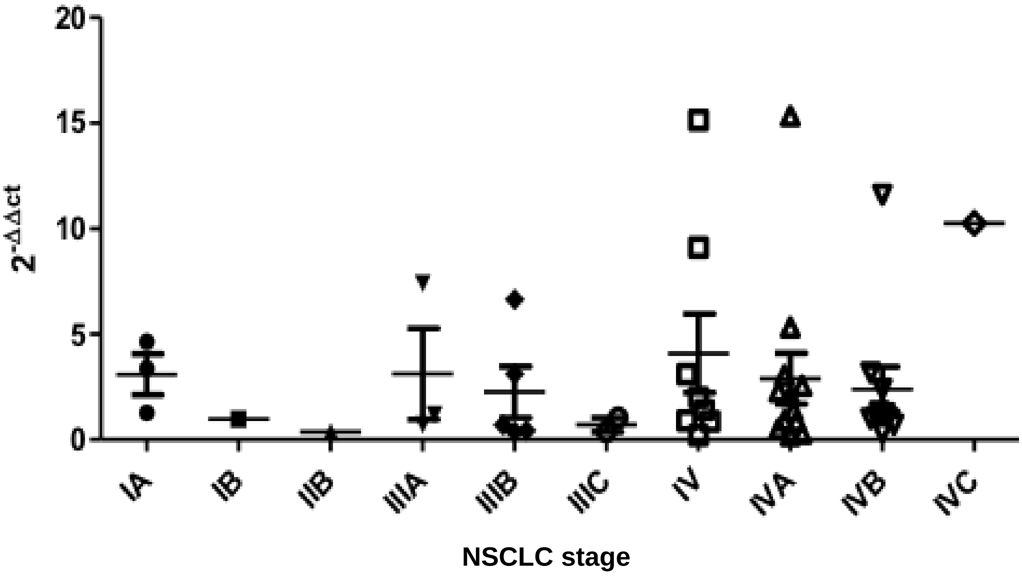

Figure 25. PBMC miR-21-5p expression among NSCLC stage. IA (n=3); IB (n=1); IIB (n=1); IIIA (n=3); IIIB (n=5); IIIC (n=2); IV (n=8); IVA (n=12); IVB (n=10); IVC (n=1). RT-qPCR data is displayed in fold change (± SE).

miR-21-5p expression relatively to NSCLC mutations is displayed in Figure 26, A down below. The miR-21-5p up-regulation in KRAS mutants stands out in comparison with the other mutations. Despite the low population, this overexpression shows a possibility of miR-21-5p interplaying in KRAS NSCLC mutants associated pathways. Figure 26, B shows that NSCLC patients with smoking history did not exhibit a considerable difference relatively to non-smokers concerning miR-21-5p expression, such as the observed on for miR-21-3p

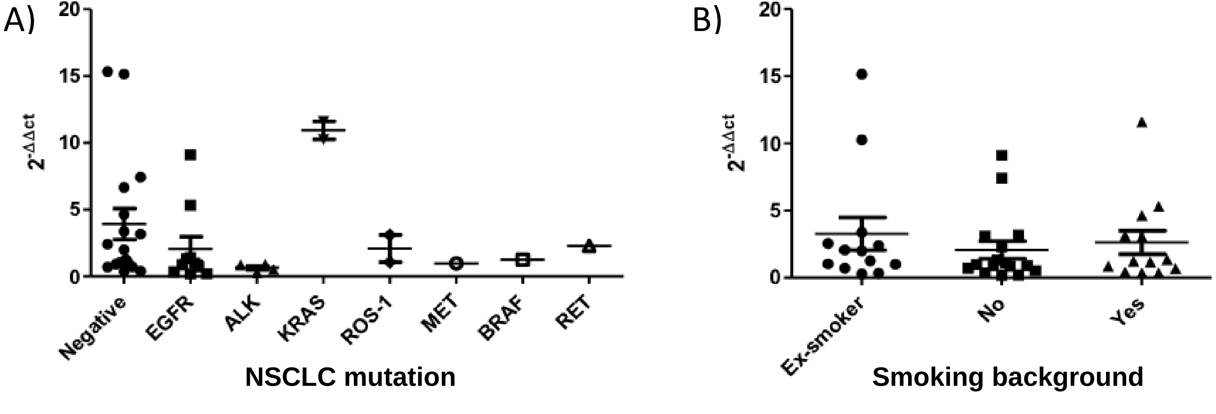

Figure 26. PBMC miR-21-5p expression among NSCLC mutations and smoking record. A) miR-21-5p expression versus NSCLC mutations. Negative (n=17); EGFR (n=10); ALK (n=4); KRAS (n=2); ROS-1 (n=2), MET (n=1); BRAF

(n=1); RET (n=1). B) miR-21-3p expression versus smoking background. Ex-smoker (n=13); No (n=16); Yes (n=13). RT-qPCR data is displayed in fold change (± SE).

Conclusions on both miR-21-3p and 5p expression in PBMCs NSCLC considering NSCLC stage, mutations and smoking history have shown propitious results. Firstly, both miR-21-3p and miR-21-5p exhibited an up-regulated tendency upon NSCLC cases at a more advanced stage (IV). miR-21-3p exhibited an overexpressed profile in BRAF NSCLC mutants, although miR-21-5p was up-regulated in NSCLC cases comprising KRAS mutation. Moreover, miR-21-3p had a higher expression trend in NSCLC patients with smoking record.

Obtained results on miR-21 expression in NSCLC PBMCs advance in accordance with the miR-21 oncogenic role in NSCLC, and show potential to discriminate and more accurately diagnose NSCLC, contributing for a more detailed characterization regarding NSCLC stage, possible mutations, and smoking connection [135]–[139], [243], [244].

4.3 Designed MB dynamics

A total of four molecular beacons were designed in order to detect miR-21. Three of them target miR-21-3p, within MB1 and MB3 21-3p having the same reverse complementary sequence tagged with BHQ1 quencher, but different fluorophores (FAM and HEX, respectively), and MB2 21-3p comprising a miR-21-3p complementary sequence with the HEX fluorophore and BHQ1 quencher as well. Remaining MB1 21-5p aims miR-21-5p, containing the correspondent reverse complementary sequence, and marked with FAM fluorophore and BHQ1 quencher. Figure 27 displays MBs structure with the corresponding donor-acceptor pairs.

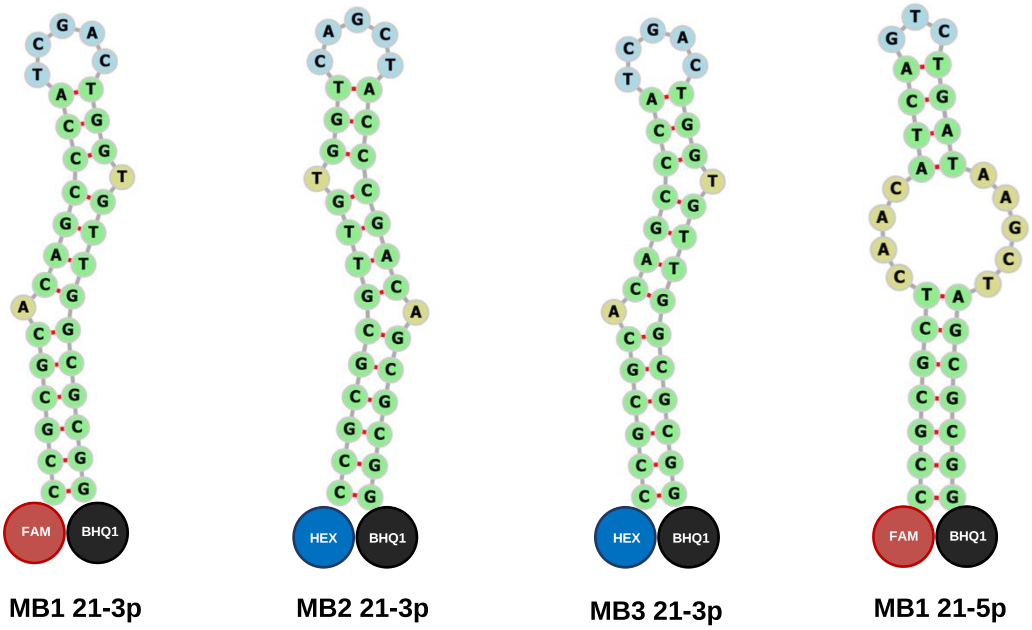

MB1 21-3p **MB2 21-3p** **MB3 21-3p** **MB1 21-5p**

Figure 27. Designed MBs folding structure with the respective fluorophore and quencher. MB1 21-3p, MB2 21-4p and MB3 21-3p target miR-21-3p. MB1 21-5p target miR-21-5p.

Designed MBs were explored in RNAfold and IDT OligoAnalyzer online softwares for MB kinetics and hybridization dynamics study. IDT OligoAnalyzer MB T_m analysis results predicted a temperature of 70.9ºC for both MB1 and MB3 21-3p, 70.6ºC for MB2 21-3p, and 63.4ºC for MB1 21-5p. RNA fold WebServer provided MBs Gibbs free energy (ΔG) projections based on their structure arrangement. ΔG differences for 21-3p MBs were higher than for MB1 21-5p, with values of -19.10 kcal/mol for 21-3p MBs 1 and 3 21-3p, -17.70 kcal/mol in MB2 21-3p, and -12.30 kcal/mol for MB1 21-5p. Table 7 resumes MBs T_m and ΔG software predictions based on their structure and folding.

Table 7. MBs T_m and ΔG software predictions

MB	T_m (ºC)	ΔG (kcal/mol)
MB1 21-3p	70.9	-19.10
MB2 21-3p	70.6	-17.70
MB3 21-3p	70.9	-19.10
MB1 21-5p	63.4	-12.30

T_m represents the temperature in which half of the nucleic acid population are denatured (random coil). MB T_m is an indicator of stability and further specificity upon hybridization mechanisms. Higher T_m is proportionally related to more stable MBs, wherein longer stems play a significant role in increased MB stability [190], [193]. Thereby, long stem MBs are more specific over the target, but also often associated with low hybridization rates and further false-negative results. On the other side, short stem MBs have a lower T_m, resulting in a more unstable MB configuration. Such instability generates higher hybridization rates, but in return, lack of specificity and false-positive products [193], [250], [251]. ΔG denotes the maximum expansion work from a closed system, in which $\Delta G<0$ indicate a more stable complex. A bigger negative value in ΔG depicts a high stable MB, and the subsequent corresponding high T_m [193], [252].

MB fold simulations were performed in RNAfold software, with the corresponding results displayed in figure 27. By analyzing MB simulations, results showed that the designed MBs for miR-21-3p (MBs 1, 2 and 3, 21-3p) were complementary between itself, generating a very small hairpin, and an exceedingly long stem consisting of the previously designed 6 length stem, followed by the miR-21-3p complementary sequence which creates inner nucleotide binding. Therefore, corresponding T_m (70.9°C and 70.6°C) and ΔG (-19.10 kcal/mol and -17.70 kcal/mol) results for miR-21-3p targeting MBs suggest a highly stable MB, which can demonstrate great selectiveness to miR-21-3p, but probable hybridization limitations as well. MB1 21-5p fold simulation data revealed an after stem middle loop region, and a further second small hairpin that results from 21-5p complementary sequence bonding through nucleotide matching. Data from T_m (63.4°C) and ΔG (-12.30 kcal/mol) for MB1 21-5p predicted a less, but considerably stable MB, with hybridization potential towards miR-21-5p [193], [250].

4.4 MB1 21-3p study

MB1 21-3p was design to target miR-21-3p by the incorporation of the reverse complementary miR-21-3p sequence at the MB loop region. MB1 21-3p is labelled with the fluorophore FAM (λ_{ex} = 495 nm; λ_{em} = 520 nm) and BHQ1 quencher. Figure 28 represents MB1 21-3p.

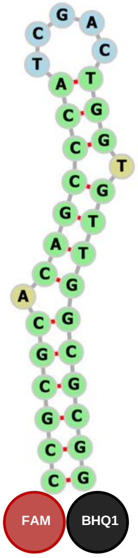

MB1 21-3p

Target: miR-21-3p

Loop design: miR-21-3p reverse complementary

Fluorophore: FAM

Quencher: BHQ1

Figure 28. MB1 21-3p design and structure with corresponding fluorophore and quencher. Structure image represent MB1 21-3p fold configuration.

4.4.1 Biophysical characterization

In chapter 4.4.1 - Biophysical characterization, experiment results on MB1 21-3p structural characterization and dynamics are discussed and analyzed.

4.4.1.1 FRET / Reverse FRET melting

FRET and reverse FRET melting assays were performed in duplicate for MB1 21-3p in 1× PBS and lithium cacodylate 10 mM. In FRET assays, fluorescence is monitored over temperature variation, enabling MB configuration track from closed stem-loop to random coil folding via donor-quencher division through temperature increase, and further donor fluorescent signal [192], [200]. MB1 21-3p FRET melting results in 1× PBS and lithium cacodylate are displayed in Figure 29.

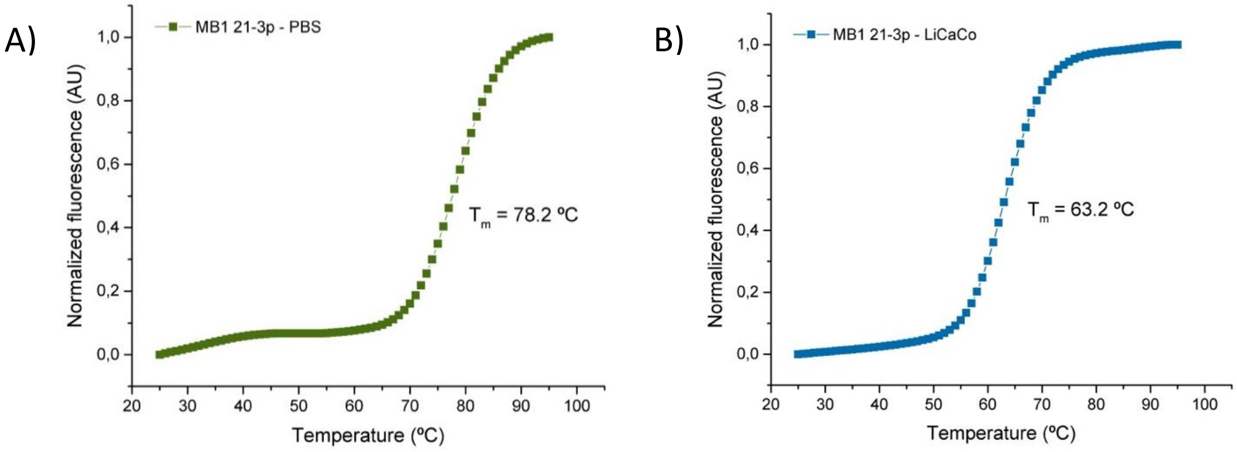

Figure 29. MB1 21-3p FRET curves and T_m. A) MB1 21-3p FRET melting in 1× PBS. B) MB1 21-3p FRET melting in lithium cacodylate.

Considering Figure 29, the MB1 21-3p stem-loop structure began to open at around 70°C in PBS, and 55°C in lithium cacodylate, reaching total unfold at the fluorescence peak. MB1 21-3p revealed a T_m of 78.2°C in 1× PBS and 63.2°C in lithium cacodylate. Collected MB1 21-3p T_m results do not meet the predicted T_m from previous software simulations (70.9°C), taking into account that simulations did not consider MB behavior in buffer solutions like the used ones. Based on FRET melting assays and T_m, MB1 21-3p exhibited a more stable configuration in PBS than in lithium cacodylate, which is showed by the higher T_m on PBS (78.2°C > 83.2°C). Mergny *et al.* had already shown higher G4 conformation stability in potassium and sodium over lithium [253]. Furthermore, PBS mimics the biological environment more accurately in relation to lithium cacodylate, giving a more exact MB dynamic profile in biological samples miRNA detection.

Reverse FRET melting experiments analyze MB kinetics as a regular FRET melting assay, although in this case, fluorescence monitoring starts at a higher temperature until reaching the lower selected temperature [192], [200]. Hereby, the MB structure initiates in an open conformation due to high temperature, and fold towards a stem-loop configuration as the temperature gradually drops. Due to equipment limitations, reverse FRET melting assays were performed by fluorescence acquisition at specific temperatures with a 5-degree range.

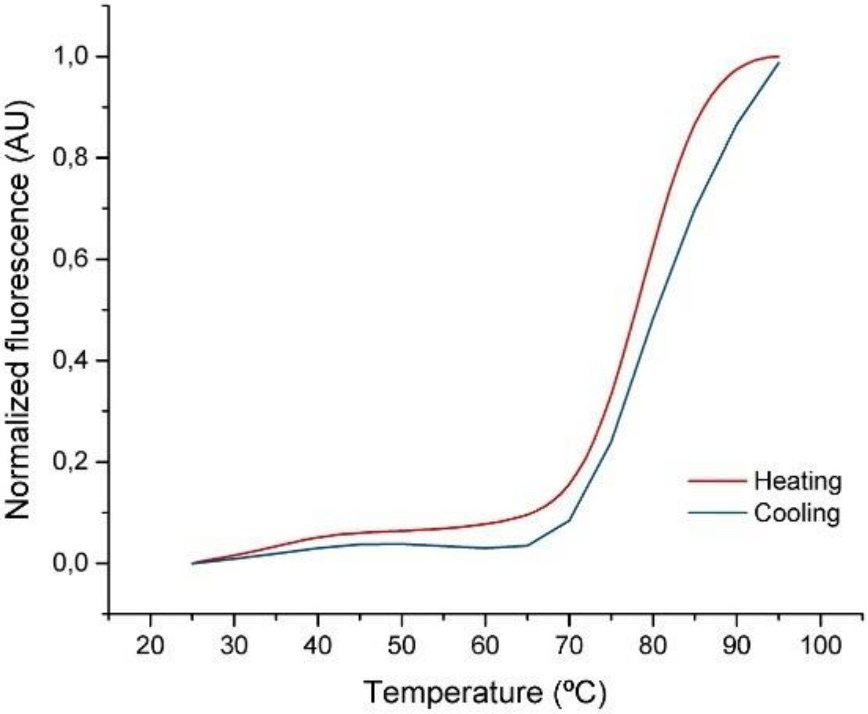

Figure 30. FRET and reverse FRET melting curves of MB1 21-3p. Fluorescence was monitored from 25°C to 95°C, returning to 25°C in reverse FRET melting.

Regarding Figure 30 results on FRET and reverse FRET melting for MB1-3p, it is noticeable that the FRET curve and the reverse FRET curve profile is similar, indicating a stem-loop rupture during the heating step, and a posterior MB hairpin configuration retake ability upon cooling. In this assay, MB1 21-3p T_m was 78.5°C according to FRET curve, and 81°C to the reverse FRET curve. Obtained T_m values resemble FRET melting previous results in Figure 29, A for MB1 21-3p (78.2°C).

4.4.1.2 Circular dichroism (CD)

MB1 21-3p were prepared in 1× PBS at 5 µM and in lithium cacodylate 10 mM at 10 µM for CD experiments. MB1 21-3p conformational studies in CD give details about the MB folding and nucleic acid structure [205], [211]. CD melting assays on MB1 21-3p did not provide data for T_m determination maybe due to low sample ellipticity and concentration, as well as because of the high MB1 21-3p T_m.

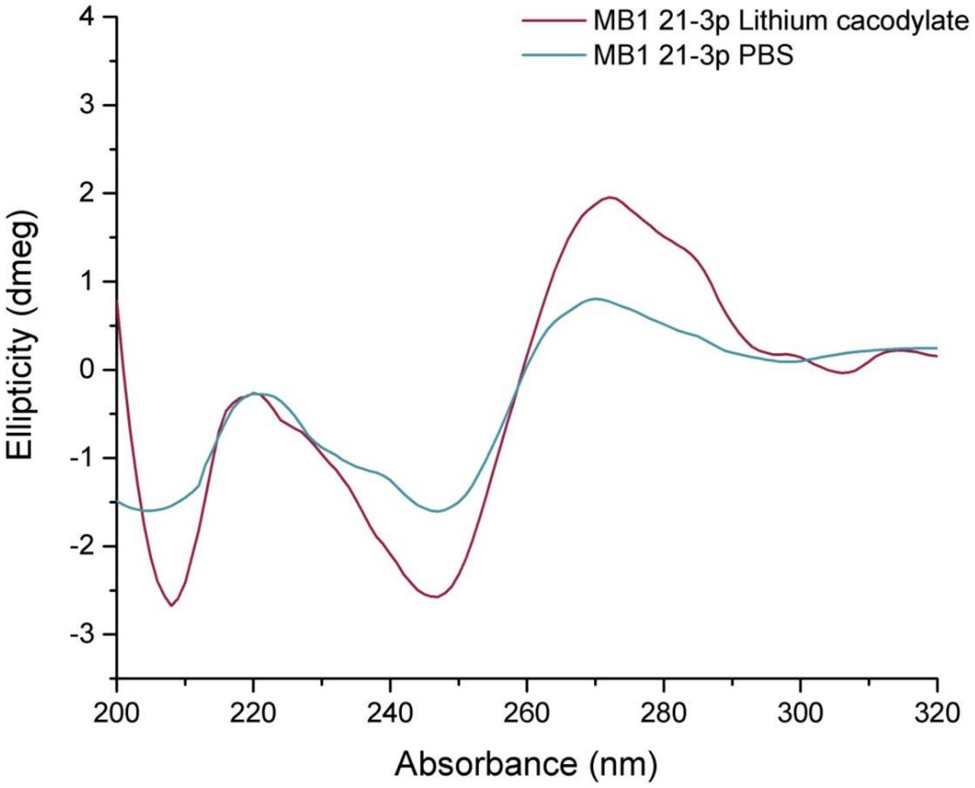

Figure 31. MB1 21-3p CD spectra in PBS and lithium cacodylate. CD spectra measurements were obtained at 20°C in a 200-320 nm range within 4 accumulations.

By analyzing Figure 31, it is visible that both MB1 21-3p PBS and lithium cacodylate CD spectra show a double helix (B-form) DNA signature CD profile, represented by positive wavelength band in between 260-280 nm with a 274 nm band, and negative band nearby 245 nm [209]–[211].

Aforementioned DNA CD profile resembles the MB double helix, and also the probable loop region further binding in MB1 21-3p (Figure 28), resulting in a small hairpin DNA long stem MB configuration. MB1 21-3p showed a weaker ellipticity signal in PBS as in lithium cacodylate, fact that probably rely on the lower MB concentration in PBS, or even the more stable profile of MB1 21-3p in PBS (Figure 29, A).

4.4.1.3 Nuclear magnetic resonance (NMR)

NMR spectroscopy studies were carried in MB1 21-3p in order to analyze unfolding kinetics, as well as hybridization dynamics. Signature MB stem-loop profile exhibit peaks in the imino region, corresponding to the DNA sequence stem and hairpin of the MB [217]–[219]. Firstly, MB1 21-3p spectra was acquired at 25ºC, 40ºC and 60ºC for the monitoring of the specific stem loop peaks over temperature increase. Figure 32 depicts the MB1 21-3p NMR spectra at different temperatures.

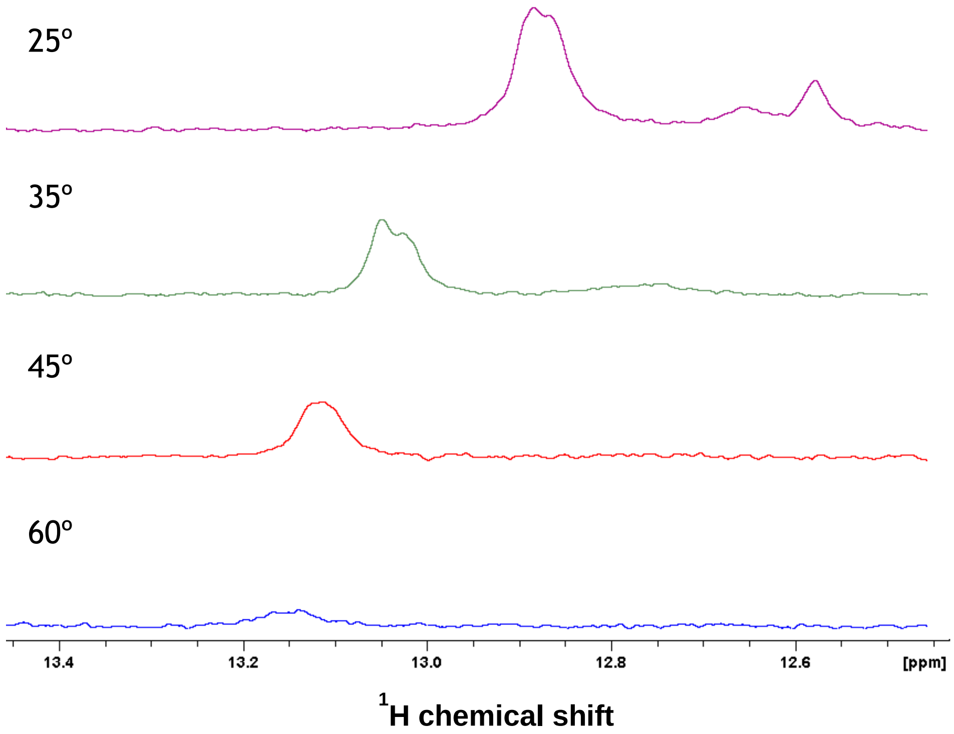

Figure 32. MB1 21-5p NMR spectra with temperature variation. Displayed spectra only comprises the stem region where the MB specific signals are present.

As observed in Figure 32, at 25ºC the MB1 21-3p had two signals between 12.6-12.8 ppm, and a more intense signal near 13 ppm. With temperature variation, the two 12.6-12.8 ppm signals corresponding to the loop region start to vanish, suggesting the MB unfold start from the loop region towards the stem. At 60ºC, these two signals were no longer visible and the stronger one relative to the stem had its' regular profile changed [219], [254]–[257]. Gathered NMR data on MB1 21-3p alone are congruent with previous FRET melting results, which demonstrated the MB1 21-3p unfold with temperature variation.

Additionally, titrations with $MgCl_2$ were conducted in the MB1 21-3p sample to study the possible influence of Mg^{2+} in MB stability and unfolding mechanisms. Mg^{2+} can induce G4 destabilization, so it may also have a destabilizing role in the high stable MB1 21-3p structure, and further promote MB1 21-3p hybridization [258]. Furthermore, synthetic miR-21-3p was also added to MB1 21-3p to analyse if there was a change in the MB profile NMR spectra when the corresponding miRNA sequence was added. No changes were noticed regarding the $MgCl_2$ titrations and miR-21-3p addition, suggesting that Mg^{2+} did not enhanced any alteration in the MB1 21-3p unfolding process, and also that the addition of synthetic miR-21-3p did not stimulate any interaction with the MB1 21-3p. Obtained NMR data on MB1 21-3p with miR-21-3p showed no difference between the MB1 21-3p NMR spectra alone and with the correspondent miRNA, supporting that the MB1 21-3p did not hybridized with the miRNA, which is further related with MB1 21-3p hybridization constraints due to the extremely long stem.

4.4.2 Interaction studies

The following chapter 4.4.2 - Interaction studies discusses MB1 21-3p hybridization assays results with the corresponding miR-21-3p synthetic sequence and biological samples.

4.4.2.1 MB1 21-3p hybridization assays optimization

MB1 21-3p hybridization conditions were optimized for maximum miR-21-3p detection performance. In a starting point, MB hybridization temperature and fluorescence time were optimized due to their crucial influence on MB hybridization experiments and fluorescence data output. MB hybridization temperature is located below MB T_m [226], [227]. Furthermore, MB1 21-3p T_m was taken as reference for MB hybridization temperature determination.

MB1 21-3p hybridization temperature screening was initially conducted in a temperature range of 50-78ºC, in which was selected the range 50-64ºC. Hybridization temperature screening assays were realized using MB1 21-3p and the correspondent miR-21-3p synthetic sequence. Fluorescence reads were carried out in two different plate readers (SpectraMax Gemini XPS Microplate Reader (Plate reader 1) and GloMax™ Explorer Multimode Microplate Reader (Plate reader 2)), as result of incongruent data reported below.

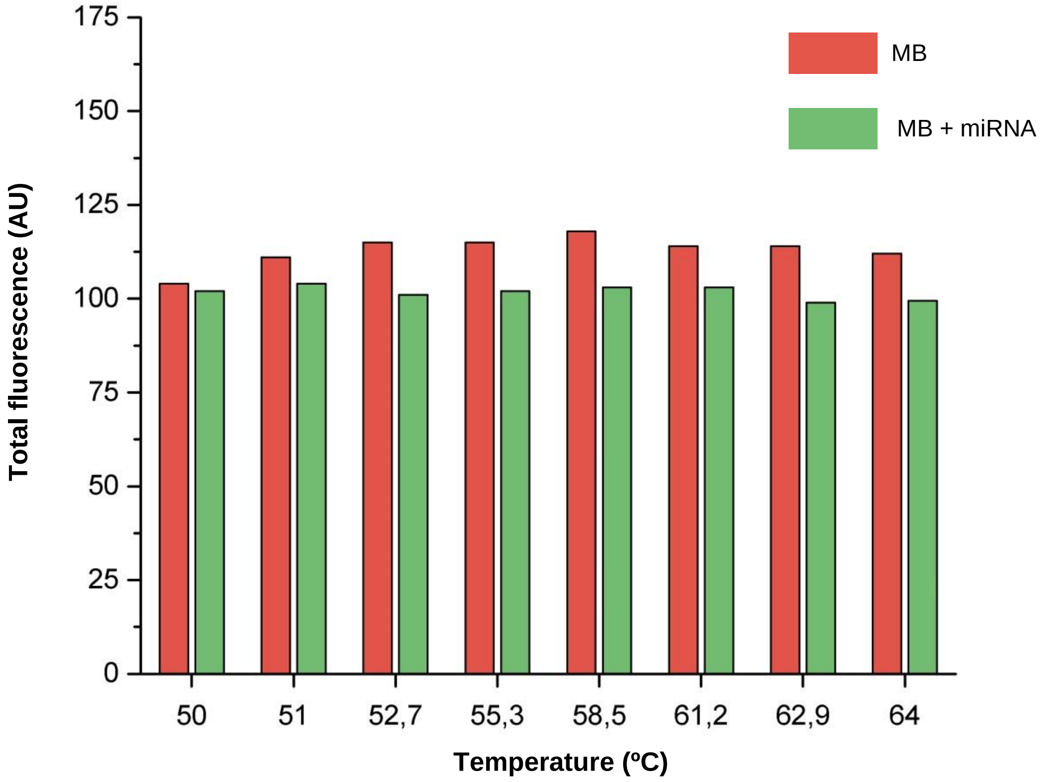

Figure 33. MB1 21-3p fluorescence hybridization temperature screening results obtained in Plate reader 2. Displayed data correspond to raw fluorescence values of a single assay (n=1).

Figure 33 presents total fluorescence reads in the MB1 21-3p hybridization temperature screening assay, which were measured in one of the microplate readers. As observed, alone control MB fluorescence levels were higher in comparison to the MB + miRNA values, proposing no MB1 21-3p hybridization with synthetic miR-21-3p. The MB1 21-3p hybridization inability option is supported by previously reported results, in which software simulations predicted a high stable MB1 21-3p configuration caused by miR-21-3p complementary sequence inner nucleotide paring, resulting in a potential 13 length stem with a minor loop arrangement (figure 26). According to Tsourkas *et al.*, long stem MBs have high specificity towards their target, although, such configuration does not favor hybridization. Tsourkas *et al.* also appointed a 6 pair stem length MB as a long stem MB [193]. Moreover, considering the inherent hybridization limitations of a 6 stem length MB, it is expected that a 13 stem length MB such as MB1 21-3p would have superior constraints towards hybridization performance [193], [250]. Additionally, FRET melting assays determined a high T_m (78.2ºC) for MB1 21-3p that could be related to the proposed constitutional MB1 21-3p stability.

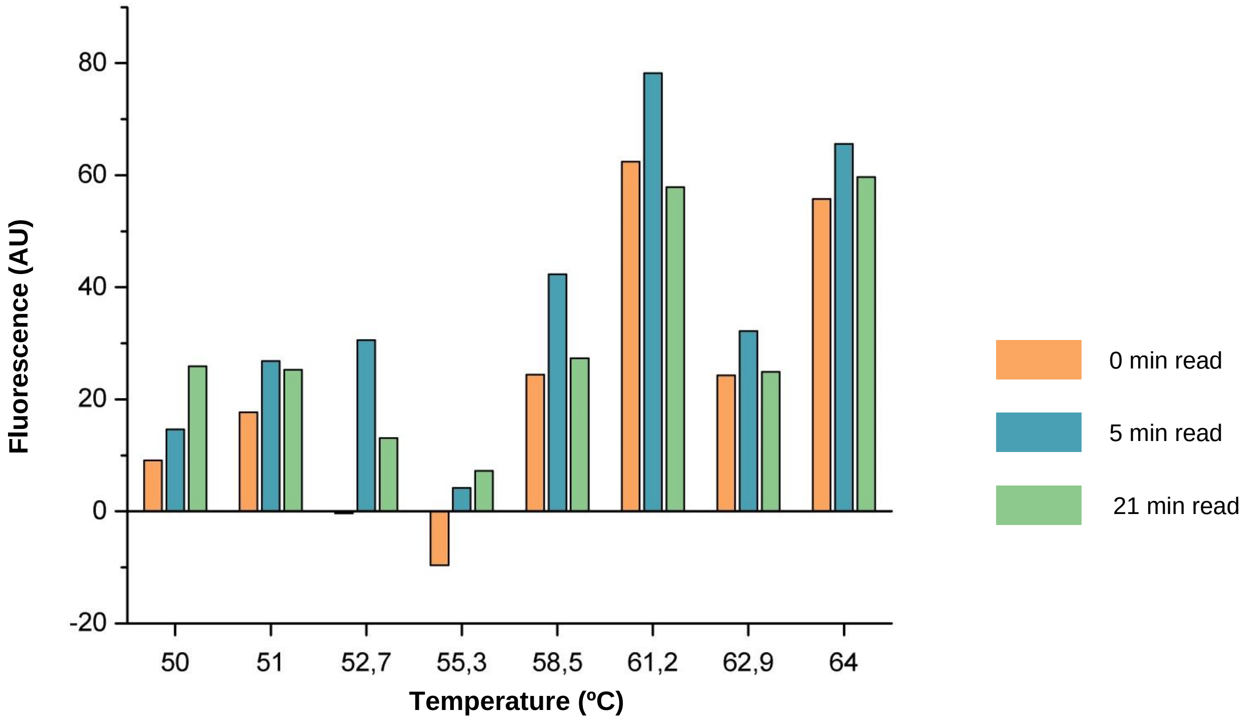

Figure 34. MB1 21-3p fluorescence hybridization temperature and reading time screening results obtained in plate reader 1. Presented data result from MB + miRNA (with MB 21-3p basal fluorescence subtracted) means fluorescence values of 5 separate assays (n=5).

Despite discussed results on MB1 21-3p hybridization ineptitude option, MB1 21-3p fluorescence hybridization temperature screening results measured on Plate reader 1 depicted in Figure 34 open up a new window in MB1 21-3p hybridization dynamics.

By doing the exact same procedure for MB1 21-3p hybridization temperature screening, but using a different fluorescence measurement equipment (plate reader 1), samples containing MB1 21-3p and synthetic miR-21-3p revealed increased fluorescence levels over control MB samples. Furthermore, it was verified that Plate reader 1 was very sensible regarding fluorescence measurements, which even provided big fluorescence differences in similar samples. On the other hand, Plate reader 2 did not exhibited high fluorescence differences between different samples. Thus, further fluorescence measurements were made using both plate readers when possible, for more precise fluorescence data.

Figure 34 compiles the results from 5 independent assays, wherein basal control MB was discounted in MB + miRNA samples. Besides hybridization temperature screening in the selected 50-64ºC range, plate fluorescence reading time was also optimized throughout the experiments. Pursuant Figure 34 results, optimal MB1 21-3p hybridization temperature was

61.5ºC (78.24 fluorescence value with basal MB deducted) and highest fluorescence measurements were acquired 5 min after reading. Provided data suggest an alternative outcome in MB1 21-3p hybridization capacity, showing some substantial results apropos MB1 21-3p hybridization to miR-21-3p.

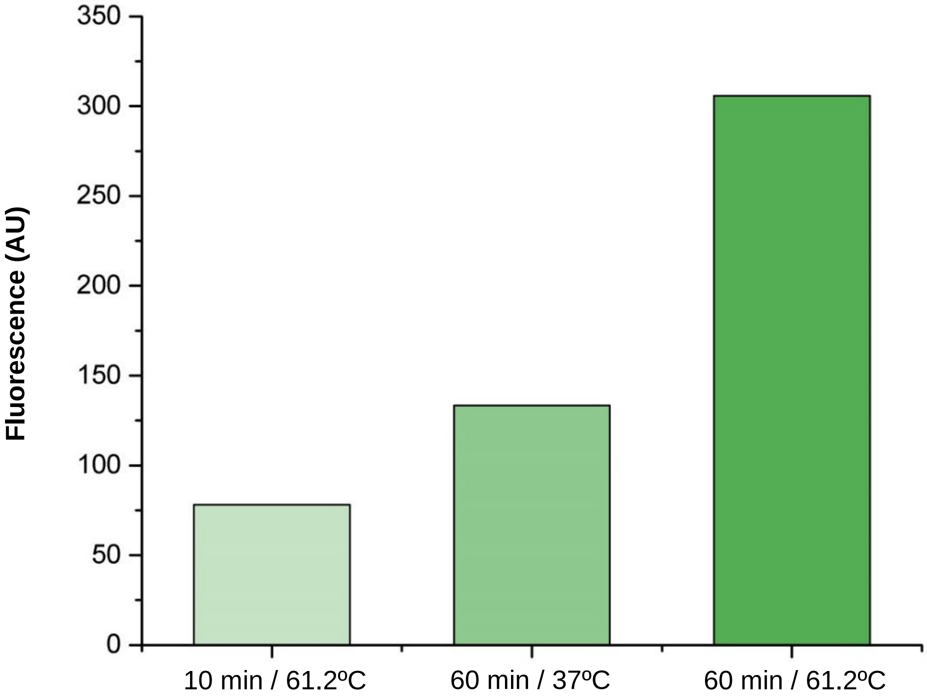

Figure 35. MB1 21-3p incubation time and temperature optimization towards maximum hybridization efficiency. First column represents achieved MB1 21-3p better conditions. Following columns represent condition variation according to MB hybridization studies. Fluorescence data got MB 21-3p basal fluorescence subtracted and was measured in Plate reader 1 (n=1).

With the objective of improving MB1 21-3p hybridization efficiency, further other conditions optimization were done. In agreement with several studies, along with hybridization temperature, MB incubation time with target is also critical. Higher incubation times for 1-2 h, or even overnight, plus MB hybridization step incubation at 37ºC are widely reported [105], [197], [225]–[227], [229]. Given reported information in MB hybridization, further optimization assays involving higher incubation times (1 h) at 37ºC and 61.2ºC were managed.

Figure 35 exhibits the results from MB1 21-3p hybridization in different incubation times and temperatures. The fluorescence data with basal control MB subtracted showed that a higher incubation time (60 min) at the precise MB1 21-3p hybridization temperature (61.2ºC) enhanced hybridization efficiency through a larger MB + miRNA gap over control MB.

4.4.2.2 FRET / Reverse FRET melting

FRET and reverse FRET melting experiments were additionally executed with MB1 21-3p combined with the synthetic miR-21-3p sequence to analyze MB melting curve profile in presence of the correspondent target miRNA. Used protocol included a gradual temperature increase up to 95ºC with a 10 min incubation step for total MB unfold, and a subsequent progressive sample cooling, including a 10 min incubation at 61.2ºC for hybridization to take place. MB1 21-3p at 0.2 μM was mixed with 1, 2 and 4 MB equivalent (0.2, 0.4 and 0.8 μM, respectively) of synthetic miR-21-3p.

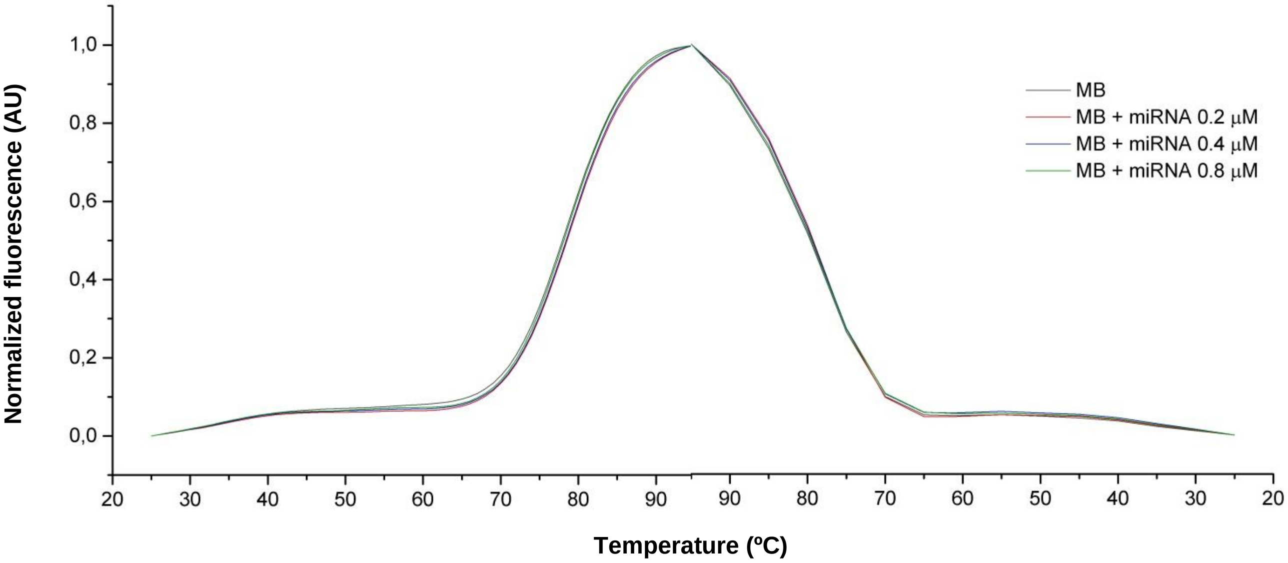

Figure 36. MB1 21-3p with miR-21-3p (0.2, 0.4 and 0.8 μM) FRET and reverse FRET melting curves.

Figure 36 show the FRET and reverse FRET melting curve behavior for MB1 21-3p alone, as in MB1 21-3p along with synthetic miR-21-3p at 1, 2 and 4 MB equivalents. In all samples, fluorescence data indicate an MB opening with the temperature increase until MB full extend at maximum fluorescence peak. Sample cooling lead fluorescence decay, suggesting MB signature structure recovery. MB1 21-3p together with the correspondent miR-21-3p sequence in the same, and ever higher concentrations, did not led to any melting curve variance in FRET performed assays. Presented results resemble FRET assays on single MB1 21-3p reported in chapter 4.4.1.1 - FRET / Reverse FRET melting (Figure 30), and corroborate the former hypothesis of MB1 21-3p hybridization inability due to long stem provided stability, already discussed comprehensively in chapter 4.4.2.1 - MB hybridization assays optimization [193], [250].

4.4.2.3 SDS-PAGE electrophoresis

SDS-PAGE electrophoresis was applied for MB1 21-3p hybridization studies with synthetic miR-21-3p and the band profile was compared in three separate sets involving different conditions. One set was incubated at 25ºc for 10 min, and the two remaining ones at 40ºC and 60ºC. Each set included four total samples comprising miR-21-3p (10 µM), MB1 21-3p (10 µM), MB1 21-3p (10 µM) with 1 equivalent of miR-21-3p (10 µM), and MB1 21-3p (10 µM) with 2 equivalents of miR-21-3p (20 µM).

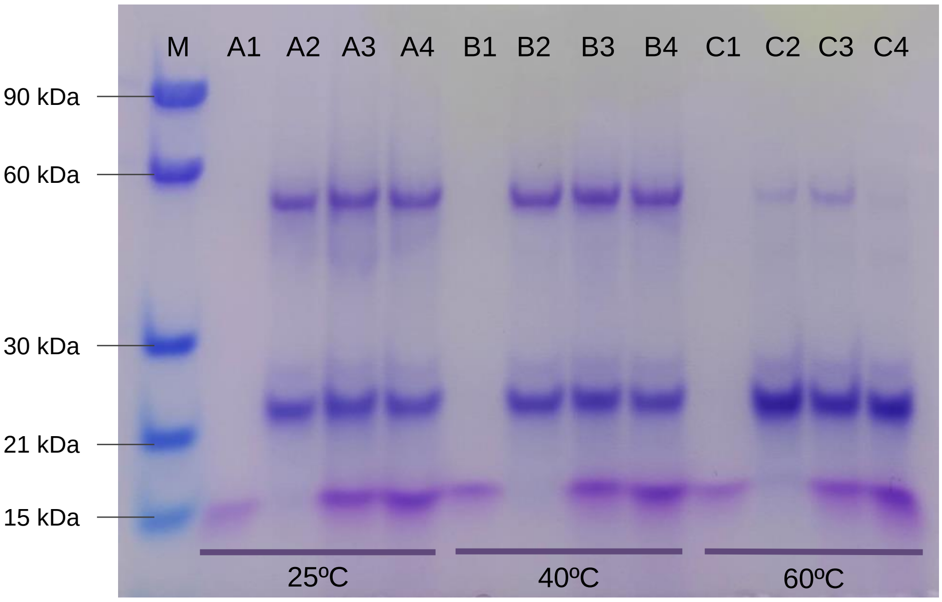

Figure 37. MB1 21-3p hybridization SDS-PAGE electrophoresis gel results. M: Weight marker; A: 25ºC incubation sample set; B: 40ºC incubation sample set; C: 60ºC incubation sample set; 1: miR-21-3p (10 µM); 2: MB1 21-3p (10 µM); 3: MB1 21-3p (10 µM) + miR-21-3p (10 µM); 4: MB1 21-3p (10 µM) + miR-21-3p (20 µM).

Figure 37 displays the results on MB1 21-3p hybridization SDS-PAGE electrophoresis. According to the gel profile, it is visible in all the labelled 1 lanes the correspondent synthetic miR-21-3p band at 10 kDa. Lanes 2 had only MB1 21-3p, which exhibited two bands (around 60 kDa and 20 kDa) for 25ºC and 40ºC incubations, and a single 20 kDa band at the 60ºC incubation set. The 60 kDa band at 25ºC and 40ºC correspond to higher weight MB1 21-3p aggregates, and the 20 kDa band to the native MB1 21-3p structure. The 60 kDa band at 25ºC and 40ºC incubation sets represent higher weight MB1 21-3p aggregates. At 60ºC, the 60 kDa band is not intense as at 25ºC and 40ºC, indicating that the 60ºC pre-incubation step led to aggregate disjunction and further MB1 21-3p fold into their standard conformation. Lanes 3 and 4 showed a clear miR-21-3p and MB1 21-3p band separation, which weights and intensity correspond to control miR-21-3p and MB 21-3p band profile in the same respective set. Conclusions on the presented results indicate that the presence of miR-21-3p synthetic sequence in MB1 21-3p samples do not affect the signature MB1 21-3p band profile, as it looked equally in both single and MB1 21-3p with the correspondent miR-21-3p. Furthermore, the two distinct bands of MB1 21-3p lanes demonstrate two types of MB1 21-3p arrangements which might represent MB1 21-3p structures linked between themselves, creating a high weight molecular complex.

In conformity with Bui *et al.* studies on DNA hairpin hybridization throughout SDS-PAGE electrophoresis, sequence hybridization generates higher molecular weight structures than the sequences alone, which can be verified through SDS-PAGE electrophoresis gel profile band. The more sequences that hybridize, the heavier the complex gets [224]. The fact that when combined, MB1 21-3p and miR-21-3p keep their weights as seen in gel bands, implies no interaction regarding the MB and the complementary miRNA, and further supports the MB1 21-3p hybridization incapacity possibility, as previously shown by FRET / reverse FRET melting assays.

4.4.2.4 *In situ* MB1 21-3p - miRNA detection

After hybridization protocol optimization, the *in situ* MB-based miRNA detection with MB1 21-3p was prepared for miR-21-3p identification in more complex samples. MB1 21-3p was incubated with 500 ng total RNA from NSCLC and control PBMCs at 61.2°C, and fluorescence was further measured in a microplate reader. Figure 38 exhibits total fluorescence data acquired in relation to MB1 21-3p total RNA miRNA detection.

Total fluorescence results for MB1 21-3p with total RNA from control and NSCLC PBMCs depicted in Figure 38 demonstrates almost no difference between controls and NSCLC samples. The small variance among control and NSCLC MB1 21-3p total fluorescence does not meet the overexpressed miR-21-3p RT-qPCR pattern in NSCLC PBMCs (Figure 18). Moreover, the presented minor deviation could be connected with the fact that MB1 21-3p cannot hybridize towards their correspondent miR-21-3p already demonstrated by previous MB1 21-3p hybridization, FRET / reverse FRET melting and SDS-PAGE electrophoresis assays.

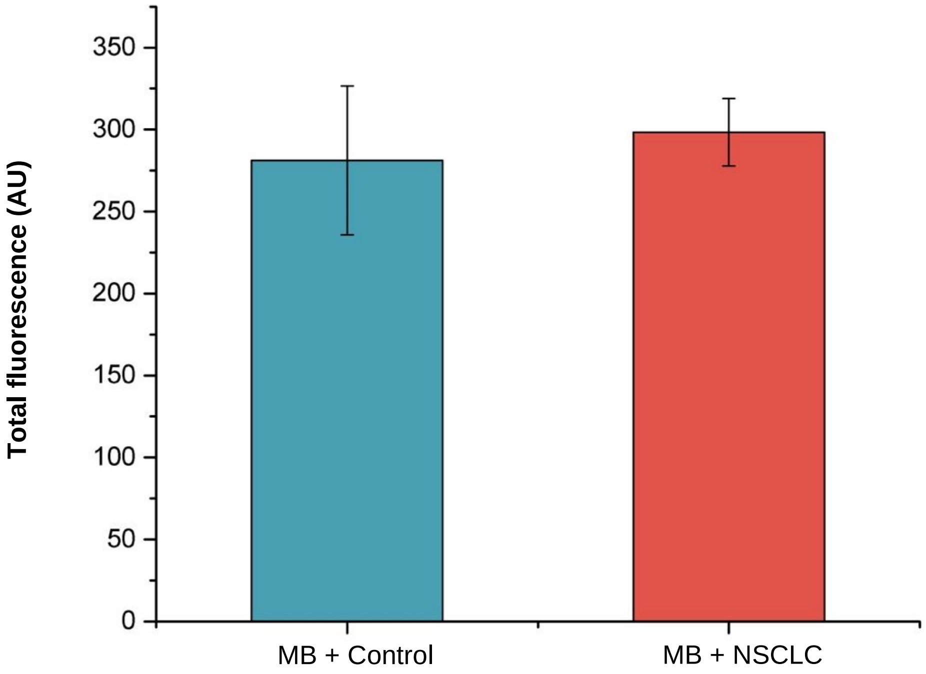

Figure 38. MB1 21-3p NSCLC and control PBMC total RNA hybridization assay. Fluorescence data was measured in Plate reader 1 and is represented as total fluorescence mean results from tested control (n=3) and NSCLC (n=5) groups (± SE).

Nevertheless, the total PBMC RNA input (500 ng) could not be enough for a proper miR-21-3p screening. According to Baker *et al.*, significant MB fluorescence differences were only noted when using total RNA concentrations above 1 μg (1000 ng) [226]. However, total PBMC RNA concentration values around 1 μg were not achievable throughout the applied RNA extraction kit (miRNeasy Micro Kit), noting the obtained PBMC RNA yields in Table 4, in which per extraction, approximately 78.11 ng/μL of PBMC RNA were eluted in 12 μL of RNase free water, not even making up to 1 μg (1000 ng) of total PBMC RNA required for a better MB-miRNA detection.

With a view to improving MB-miRNA fluorescent results, and bearing in mind that a higher total RNA input could lead to significant fluorescence differences, an approach using RT-qPCR products for MB1 21-3p miR-21-3p detection was directed to overpass the low RNA input. RT-qPCR assays were performed with total RNA from NSCLC and control PBMCs. RT-qPCR products had a high number of miR-21-3p copies as a consequence of DNA polymerase specific miR-21-3p fragment amplification. The 10 μL products were incubated with MB1 21-3p, hybridized at 61.2°C, and sample fluorescence was read.

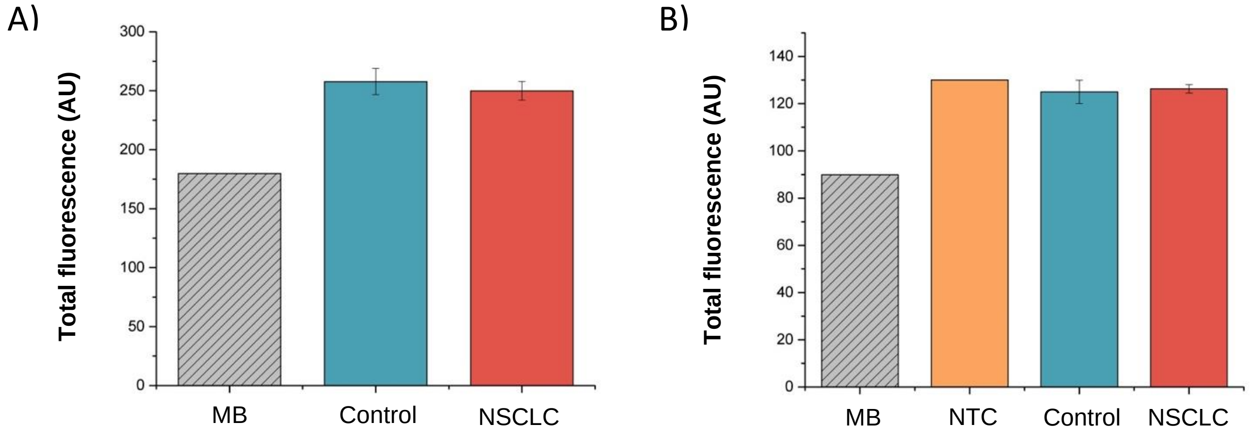

Figure 39. MB1 21-3p RT-qPCR product hybridization assays. A) Total fluorescence results were acquired in Plate reader 1 within control (n=5) and NSCLC (n=8) RT-qPCR products (± SE). B) Total fluorescence results were acquired in Plate reader 2 comprising a RT-qPCR no template control (NTC), healthy control (n=2) and NSCLC (n=3) RT-qPCR products (± SE).

Figure 39 presents total fluorescence data from MB1 21-3p hybridization assays with RT-qPCR products from NSCLC and control PBMCs. First assays were carried in the previous plate reader where MB1 21-3p hybridization conditions were optimized (Plate reader 1). In Figure 39, A, it is observed that both MB1 21-3p with RT-qPCR products from control and NSCLC PBMCs groups had similar levels of total fluorescence. Such MB1 21-3p control and NSCLC equivalent levels are inconsistent with RT-qPCR fluorescence results, wherein NSCLC samples showed a considerable overexpression of miR-21-3p.

Following MB1 21-3p hybridization assays were measured in Plate reader 2 and included an NTC with no amplification in prior RT-qPCR experiments. Plate reader 2 was used to investigate if the obtained fluorescence results are congruent with the ones from Plate reader 1, and an NTC was utilized to examine a possible SYBR Green interference in fluorescence levels. As seen in Figure 39, B, besides control and NSCLC samples fluorescence being basically identical, the NTC that do not show any amplification in the RT-qPCR assay, exhibited a slightly higher fluorescence compared with control and NSCLC amplifying products. Thus, it is proved that the RT-qPCR product containing SYBR Green interpose in fluorescence measurements due to higher fluorescence levels in the NTC sample.

Furthermore, SYBR Green excitation and emission wavelengths (λ_{ex} = 497 nm; λ_{em} = 520 nm) match MB1 21-3p fluorophore FAM peaks (λ_{ex} = 495 nm; λ_{em} = 520 nm). This SYBR Green / FAM excitation and emission overlap make it not possible to combine RT-qPCR products with a FAM donor MB, due to SYBR interference in MB1 21-3p FAM fluorescence reads, as demonstrated by the collected MB1 21-3p hybridization with RT-qPCR products.

Despite the discussed SYBR Green / FAM interplay that compromises fluorescence measurements with MB1 21-3p, data on MB1 21-3p hybridization assays are congruent with the MB1 21-3p no-hybridization hypothesis. Along the multiple performed hybridization assays, no significant differences were observed in between control and NSCLC groups as seen in RT-qPCR experiments. Moreover, the increased fluorescence in MB1 21-3p hybridization samples with RT-qPCR products result from SYBR Green presence.

To exclude the SYBR Green undesired role in MB1 21-3p hybridization assays with RT-qPCR products, an MB design with a different fluorophore that does not meet SYBR Green excitation and emission wavelengths makes the previously suggested MB / RT-qPCR product approach practicable, since a higher number of miR-21-3p is needed and can be achieved via RT-qPCR, and RT-qPCR product elements no longer converge upon MB fluorescence reading. Thus, two MBs were designed with the fluorophore HEX (λ_{ex} = 535 nm; λ_{em} = 556 nm) comprising a complementary miR-21-3p sequence (MB2 21-3p), and the miR-21-3p reverse complementary (MB3 21-3p).

4.5 MB2 and MB3 21-3p study

MB2 and MB3 21-3p were designed with a new fluorophore HEX (λ_{ex} = 535 nm; λ_{em} = 556 nm) and the BHQ1 quencher, aiming the miR-21-3p detection in RT-qPCR products. A new fluorophore was incorporated because SYBR Green excitation and emission wavelenghts (λ_{ex} = 497 nm; λ_{em} = 520 nm) overlap into the fluorophore FAM wavelengths (λ_{ex} = 495 nm; λ_{em} = 520 nm), interfering in further fluorescence readings.

MB2 21-3p and MB3 21-3p design was arranged to target miR-21-3p. MB2 21-3p loop region had the complementary miR-21-3p sequence, and MB3 21-3p the miR-21-3p reverse complementary sequence. Figure 40 illustrates MB2 and MB3 structures in the stem-loop configuration.

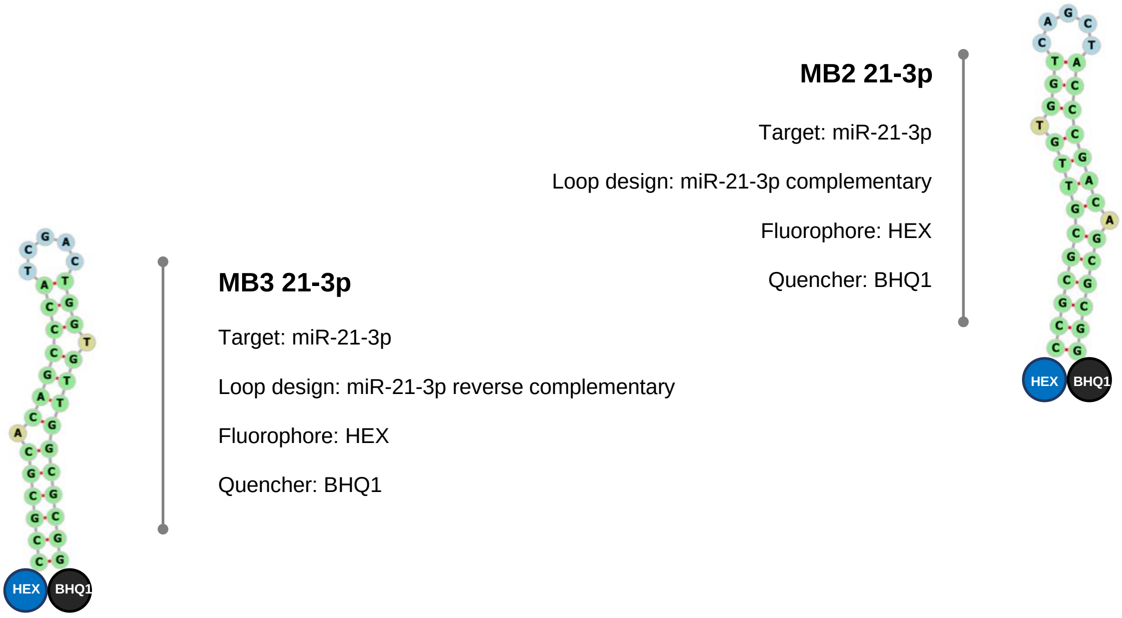

Figure 40. MB2 21-3p and MB3 21-3p design and structure with corresponding fluorophore and quencher. Structure image represent MB2 and MB3 21-3p fold configuration.

4.5.1 Biophysical characterization

In chapter 4.5.1 - Biophysical characterization, experiment results on MB2 21-3p and MB3 21-3p structural characterization and dynamics are discussed and analyzed.

4.5.1.1 FRET / Reverse FRET melting

MB2 21-3p and MB3 21-3p FRET / reverse FRET melting assays were performed in 1×PBS for MB structure folding dynamics study through fluorescence monitoring over temperature variation, and further T_m determination [192], [200]. It was expected that MB2 and MB3 21-3p FRET / reverse FRET melting curve profile results resemble MB1 21-3p ones, considering the similar structure and fold prediction for MB2 and MB3 21-3p regarding MB1 21-3p. MB2 21-3p oligonucleotide structure have the miR-21-3p complementary sequence in the 5' to 3' direction. On the other side, MB3 21-3p have the exact same structure as MB1 21-3p, where the miR-21-3p complementary sequence is arranged in reverse (3' to 5'). Both MB2 and MB3 21-3p had their fluorophore changed to HEX for further hybridization assays with RT-qPCR products. Figure 41 presents FRET / reverse FRET melting curves for MB2 and MB3 21-3p.

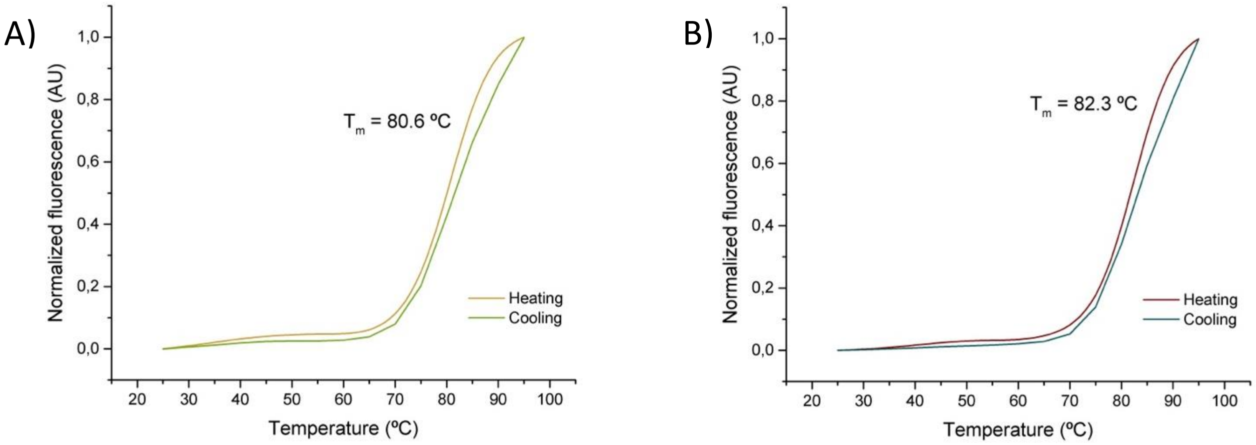

Figure 41. FRET and reverse FRET melting curves of MB2 and MB3 21-3p. A) FRET and reverse FRET melting results for MB2 21-3p. B) FRET and reverse FRET melting results for MB3 21-3p. Fluorescence was monitored from 25ºC to 95ºC, returning to 25ºC in reverse FRET melting.

In Figure 41, A, the MB2 21-3p FRET and reverse FRET melting curves show a similar behavior upon the first heating step, and the posterior cooling one. MB2 21-3p structure assemble start to dissociate at higher temperatures until reaching 95ºC, where the MB is completely unfolded. In the reverse FRET melting step, the temperature starts at 95ºC and progressively lower until 25ºC. Fluorescence starts to decrease with temperature lowering, meaning that the MB fluorophore HEX is getting closer to the acceptor (quencher), and subsequently MB will close and retake the native form. MB2 21-3p T_m was 80.6ºC in the FRET melting curve, which is a higher value relative to the prediction (T_m = 70.6ºC), but similar in relation to MB1 21-3p in PBS (T_m = 78.2ºC). A higher T_m value for MB2 21-3p (80.6ºC) in comparison with the one from the prediction (70.6ºC) could be related to prediction limitations that do not consider the buffer solution in which FRET assays were carried out. A similar MB2 21-3p T_m (80.6ºC) comparatively to MB1 21-3p (78.2ºC) is expected due to the identical structure fold, because besides being in the opposite direction, the miR-21-3p complementary sequence still promotes links involving sequence nucleotides, resulting in a stem arrangement with a minor hairpin at the top, just like MB1 21-3p. The high MB2 21-3p T_m (80.6ºC) also connects with the MB2 21-3p stable structure comprising a potential 13 stem with a 5 nucleotide loop, as reached in the structure simulations.

Regarding MB3 21-3p FRET and reverse FRET melting results in Figure 41, B, it is visible that both FRET and reverse FRET curves had a similar profile. Like previous MBs, MB3 21-3p configuration also dissembles with temperature increasing in FRET, and further recapture the closed fold arrangement upon reverse FRET temperature cooling. MB3 21-3p T_m of 82.3ºC was calculated based on FRET melting curve. The 82.3ºC MB3 21-3p T_m value was higher than the predicted one (70.9ºC), due to the already discussed simulation studies which did not take into account the used PBS buffer. However, this T_m value did not differ much from previous MB T_m, considering that MB3 21-3p have the same design as MB1 21-3p excepting the fluorophore, which was changed from FAM to HEX in MB3 21-3p. MB3 21-3p T_m is characteristic of a highly stable structure, a fact that support the long MB stem throughout miR-21-3p complementary internal coupling formerly debated in previous MB1 21-3p studies.

4.5.1.2 Circular dichroism (CD)

CD experiments on MB2 and MB3 21-3p were performed with 10 μM MBs in PBS buffer. CD data provide details on MB nucleic acid structure folding [205], [211]. MB2 and MB3 21-3p CD melting experiments did not provide spectra signal for T_m determination. Following Figure 42 exhibits CD spectra of MB2 and MB3 21-3p.

In Figure 42, both MB2 and MB3 21-3p exhibit a similar CD spectra profile, with MB3 21-3p (Figure 42, B) presenting slight ellipticity than MB2 21-3p (Figure 42, A). Furthermore, obtained MB2 and MB3 21-3p CD spectra resemble previous MB1 21-3p results.

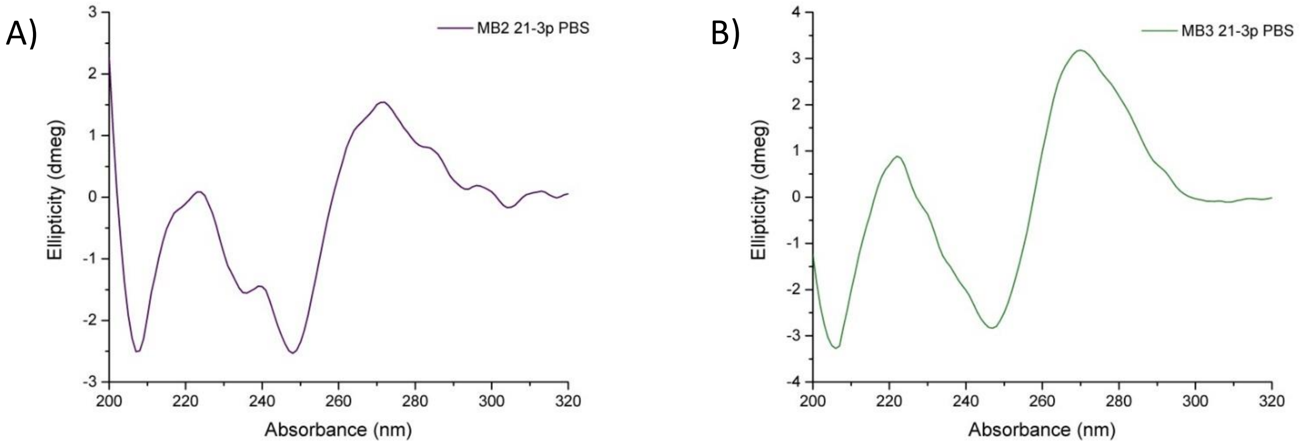

Figure 42. MB2 and MB3 21-3p CD spectra. A) CD spectra of MB2 21-3p in PBS. B) CD spectra of MB3 21-3p in PBS. CD spectra measurements were obtained at 20ºC in a 200-320 nm range within 4 accumulations.

MB2 and MB3 21-3p displayed CD spectra data is representative of the specific DNA double helix secondary structure, in which the signature positive wavelength band 274 nm peak and negative band peak near 245 nm are present [209], [211].

In the 21-3p MBs case, the DNA double helix structure, despite corresponding to the designed stem portion, also corresponds to the further stem elongation through hairpin internal miR-21-3p complementary sequence association, which also comprises a double helix structure.

4.5.2 Interaction studies

The following chapter 4.4.2 - Interaction studies discusses MB2 and MB3 21-3p hybridization assays results with the corresponding miR-21-3p synthetic sequence and biological samples.

4.5.2.1 MB2 / MB3 21-3p hybridization assays optimization

MB2 and MB3 21-3p hybridization assays optimization were performed based on previous MB1 21-3p procedures and results explored in the chapter 4.4.2.1 - MB1 21-3p hybridization assays optimization. MB hybridization temperature was screened in between 52.4-70.2ºC range, in accordance with MB2 and MB3 21-3p determined T_m (80.6ºC and 82.3ºC, respectively). Figure 43 displays fluorescence normalized results on MB2 and MB3 21-3p hybridization temperature screening.

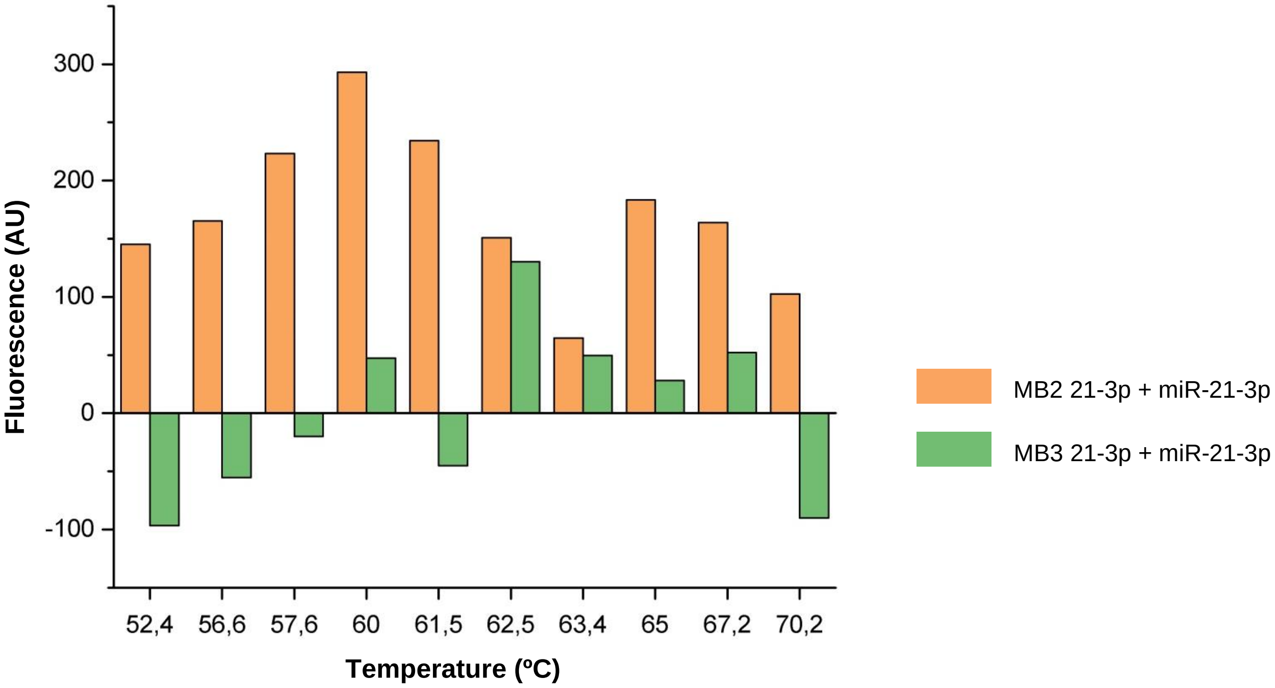

Figure 43. MB2 and MB3 21-3p hybridization temperature screening assays. Fluorescence data was aquired in Plate reader 1 and got respective MB2 and MB3 21-3p basal fluorescence discounted (n=3).

As stated by Figure 43, MB2 21-3p had higher fluorescence levels regarding single MB2 21-3p control at 60ºC (293.12 fluorescence value with basal MB deducted), temperature that represent major MB2 21-3p hybridization rate. MB3 21-3p hybridization temperature was 62.5ºC (130.1 fluorescence value with basal MB deducted), which is in conformity with the maximum fluorescence peak with MB3 21-3p basal fluorescence deducted.

Besides MB2 and MB3 21-3p unfavorable hybridization kinetics due to their highly stable structure, and noting the sensitivity and variance of fluorescence in assay measurements, fluorescence data (Figure 43) of both MB2 and MB3 21-3p suggest hybridization with miR-21-3p sequence. Furthermore, MB2 and MB3 21-3p presented superior raw fluorescence values (MB2 21-3p = 293.12 fluorescence; MB3 21-3p = 130.1 fluorescence) regarding basal levels than previous MB1 21-3p (78.24 fluorescence).

4.5.2.2 Fluorometric assays

Additional fluorometric assays were conducted on single MB2 21-3p, and further with the correspondent miR-21-3p synthetic sequence. Suchlike FRET experiments, fluorometric assays monitor fluorescence during temperature variation. MB2 21-3p (293.12 fluorescence) was selected for the higher fluorescent differences achieved in optimization results relatively to MB3 21-3p (130.1 fluorescence). Furthermore, MB2 21-3p also comprises a different design (complementary miR-21-3p) than MB1 and MB3 21-3p (reverse complementary miR-21-3p). Firstly, 1 μM of MB2 21-3p fluorescence was measured from 25ºC up to 90ºC, followed by the addition of 1 μM of synthetic miR-21-3p and further fluorescence determination assays repetition.

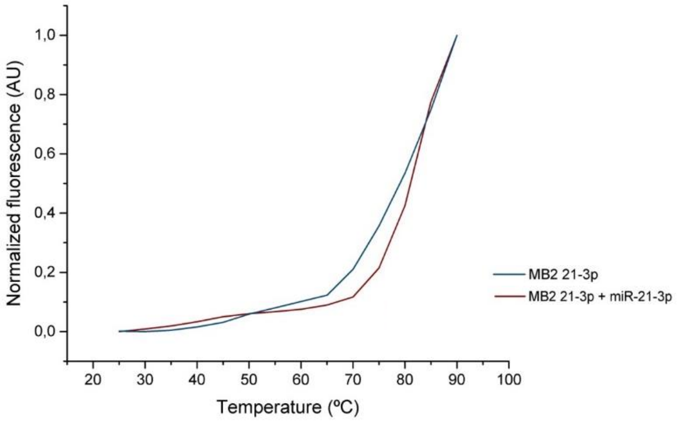

Figure 44. Fluorometric MB2 21-3p single and with synthetic miR-21-3p results. Both assays fluorescence was monitored from 25ºC to 90ºC at the correspondent HEX excitation and emission wavelengths, and further normalized.

Figure 44 shows fluorescence curves of single MB2 21-3p and with synthetic miR-21-3p. As illustrated, MB2 21-3p structure unfolds with temperature increase until reaching random coil conformation. This MB2 21-3p conformation unroll is evidenced through fluorescence augment, a consequence of HEX fluorophore separation from the BHQ1 quencher, which is responsible for fluorescence absorption when both elements are near in MB stem-loop arrangement. Upon miR-21-3p synthetic sequence addition to MB2 21-3p, the fluorescence curve profile resembles the single MB2 21-3p one. Figure 44 reported curve status assumes that the addition of miR-21-3p to MB2 21-3p does not has influence in MB2 21-3p fluorescence dynamics, suggesting no interaction between MB2 21-3p and miR-21-3p, and further connecting with MB2 21-3p hybridization discussed limitations.

4.5.2.3 *In situ* MB2 / MB3 21-3p - miRNA detection

MB2 and MB3 21-3p were especially designed for hybridization assays using RT-qPCR products. The use of RT-qPCR products in MB hybridization assays approach attempt to overpass miRNA low levels limitations in total RNA extracted from 1×10^6 PBMCs. The incorporation of the HEX fluorophore (λ_{ex} = 535 nm; λ_{em} = 556 nm) over the previous used FAM (λ_{ex} = 495 nm; λ_{em} = 520 nm), allowed real MB fluorescence measurement without RT-qPCR SYBR Green (λ_{ex} = 497 nm; λ_{em} = 520 nm) interference.

An initial MB2 and MB3 21-3p hybridization assay with RT-qPCR products were performed to select which MB had a higher sensitivity towards the products. Two miR-21-3p RT-qPCR products were incubated, and further hybridized with MB2 and MB3 21-3p at the determined hybridization temperatures (60°C and 62.5°c, respectively). Figure 45 displays total MB2 and MB3 21-3p fluorescence levels with the RT-qPCR products.

As shown in Figure 45, MB2 21-3p exhibited a slightly higher fluorescence level for PCR product 1 than MB3 21-3p. For PCR 2, both MBs demonstrated similar fluorescence levels. MB2 21-3p had been selected for further RT-qPCR products hybridization assays, not only because of the little higher fluorescence values in PCR product 1 over MB3 21-3p, but also considering fluorescence levels over basal fluorescence (MB2 21-3p = 293.12 fluorescence; MB3 21-3p = 130.1 fluorescence) evidenced in chapter 4.5.2.1 - MB2 / MB3 21-3p hybridization assays optimization, and the distinct MB2 21-3p construction with the complementary miR-21-3p sequence regarding MB1 and MB3 equal design with miR-21-3p reverse complementary sequence.

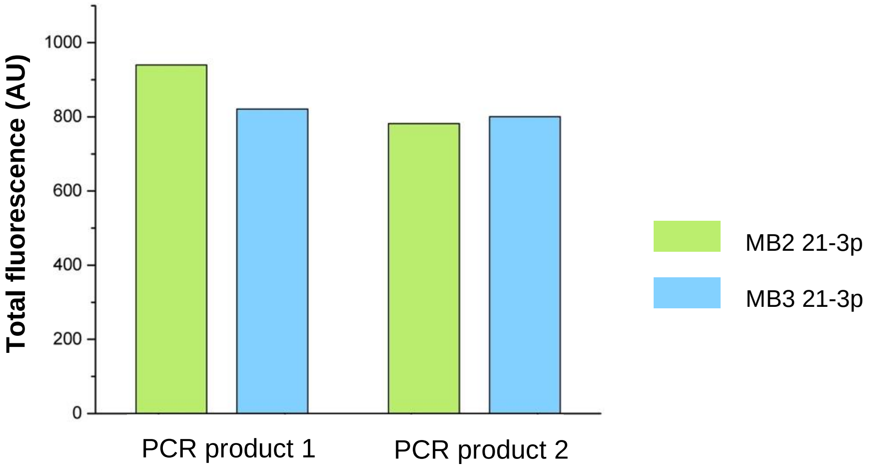

Figure 45. MB2 and MB3 hybridization assays with RT-qPCR products. Fluorescence data was measured in Plate reader 1 and is represented in total values regarding MB2 and MB3 21-3p hybridization with two miR-21-3p representative RT-qPCR products (n=2).

Following MB2 21-3p hybridization experiments were performed with RT-qPCR products from A549 and NHDF cell lines, in order to first analyze differences in cell line samples before advancing to more valuable NSCLC and control PBMCs. Fluorescence measurements were made applying HEX appropriate excitation and emission wavelengths (λ_{ex} = 535 nm; λ_{em} = 556 nm) in both microplate readers used in this work, for more accurate fluorescence data. Figure 46 represents total fluorescence values measured in both readers for MB2 21-3p hybridization assays with A459 and NHDF RT-qPCR products.

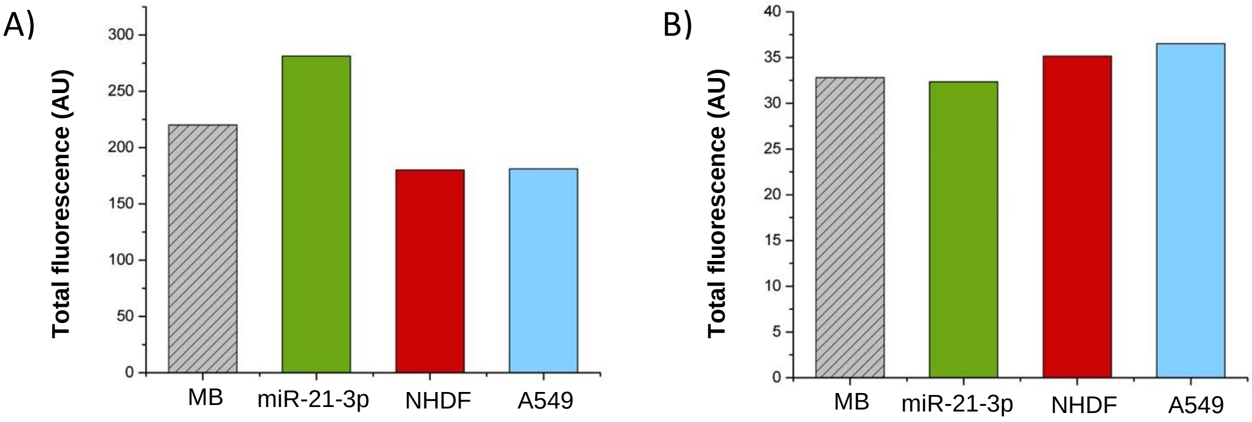

Figure 46. MB2 21-3p NHDF and A549 RT-qPCR products hybridization assays. MB: MB2 21-3p; miR-21-3p: MB2 21-3p + synthetic miR-21-3p; NHDF: MB2 21-3p + NHDF RT-qPCR product; A549: MB2 21-3p + A549 RT-qPCR product (n=1). A) Total fluorescence results were acquired in Plate reader 1. B) Total fluorescence results were acquired in Plate reader 2.

In Figure 46, A, single MB2 21-3p basal fluorescence was higher than NHDF and A549 RT-qPCR products with MB2 21-3p. Furthermore, NHDF and A549 samples MB2 21-3p fluorescence was equal, which was not expected due to miR-21-3p higher ratios in A549 as confirmed in previous RT-qPCR assays. Figure 46, B depicts MB2 21-3p RT-qPCR fluorescence levels above MB2 21-3p basal fluorescence, in which A549 was a little higher value regarding the NHDF sample. Nevertheless, fluorescence differences in both Figure 46, A and B are minimal and do not represent anticipated results based on RT-qPCR miR-21-3p screening assays in NHDF and A549 cell lines, and further hybridization ratios regarding MB2 21-3p hybridization optimization, where MB2 21-3p with synthetic miR-21-3p had a considerable fluorescence gap (MB2 21-3p = 293.12 fluorescence), comparing with the obtained ones in RT-qPCR products MB2 21-3p hybridization assays.

Gathering all the results and aftermath on designed MBs targeting miR-21-3p, obtained results, along MB1, MB2 and MB3 21-3p interaction studies, rather support low MBs 21-3p hybridization kinetics than significant miR-21-3p hybridization rates that meet previous RT-qPCR miR-21-3p screening in cell lines and PBMCs, and that are also acceptable for accurate miR-21-3p detection in biological samples. As result of an unexpected MB 21-3p structure configuration that relies on a longer stem, based on internal miR-21-3p complementary sequence nucleotide bounding, designed MBs targeting miR-21-3p turned more stable than what is desirable for miR-21-3p MB detection. Although longer stems are more specific towards their target, they also relate to low hybridization rates. A 6 pair stem is reported as a long stem in literature, so it is presumed that a potential 13 stem MB have major constraints concerning hybridization kinetics [193], [250].

Besides MBs 1, 2 and 3 21-3p hybridization optimization assays results support MB hybridization unto miR-21-3p synthetic sequence, it is important to note that MB-based fluorescence assays are very sensible, and during reported optimization assays total fluorescence levels varied in between multiple experiments, wherein sometimes even MB with miR-21-3p samples had lower fluorescence levels than single MB, showing that fluorescence levels of supposed MB hybridized with the correspondent miR-21-3p were occasionally lower than MB basal fluorescence [259], [260].

Regarding the considered hypothesis that explores MB targeting miR-21-3p hybridization hindrances, the analogous miR-21-5p strand was selected for the MB-detection hybridization studies ahead involving MB1 21-5p, which according to informatic structure fold simulations on chapter 4.3 - Designed MB dynamics, have better potential due to the open loop region, to adequately detect the correspondent up-regulated miR-21-5p in NSCLC.

4.6 MB1 21-5p study

Due to MBs targeting miR-21-3p incapacity to hybridize towards miR-21-3p because of their highly stable structure, MB1 21-5p was design to target miR-21-5p. MB1 21-5p loop region have the miR-21-5p reverse complementary sequence, and is labelled with the fluorophore FAM (λ_{ex} = 495 nm; λ_{em} = 520 nm) and BHQ1 quencher. Figure 47 represents MB1 21-5p

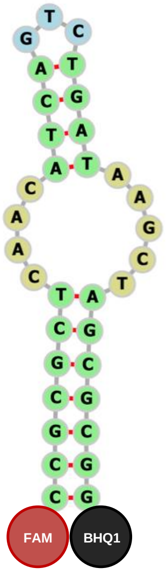

MB1 21-5p

Target: miR-21-5p

Loop design: miR-21-5p reverse complementary

Fluorophore: FAM

Quencher: BHQ1

Figure 47. MB1 21-5p design and structure with corresponding fluorophore and quencher. Structure image represent MB1 21-5p fold configuration.

4.6.1 Biophysical characterization

In chapter 4.6.1 - Biophysical characterization, experiment results on MB1 21-5p structural characterization and dynamics are discussed and analyzed.

4.6.1.1 FRET / Reverse FRET melting

MB1 21-5p was analyzed by FRET and reverse FRET melting assays both in 1×PBS and lithium cacodylate 10 mM. Like previous FRET and reverse FRET melting experiments, MB folding dynamics are studied via fluorescence monitoring over temperature alteration, as well as the determination of MB T_m [192], [200].

Figure 48, A and B displays MB1 21-5p FRET curves in 1×PBS and lithium cacodylate, wherein as expected, fluorescence raised upon temperature increase as result of fluorophore FAM detachment from BHQ1 quencher.

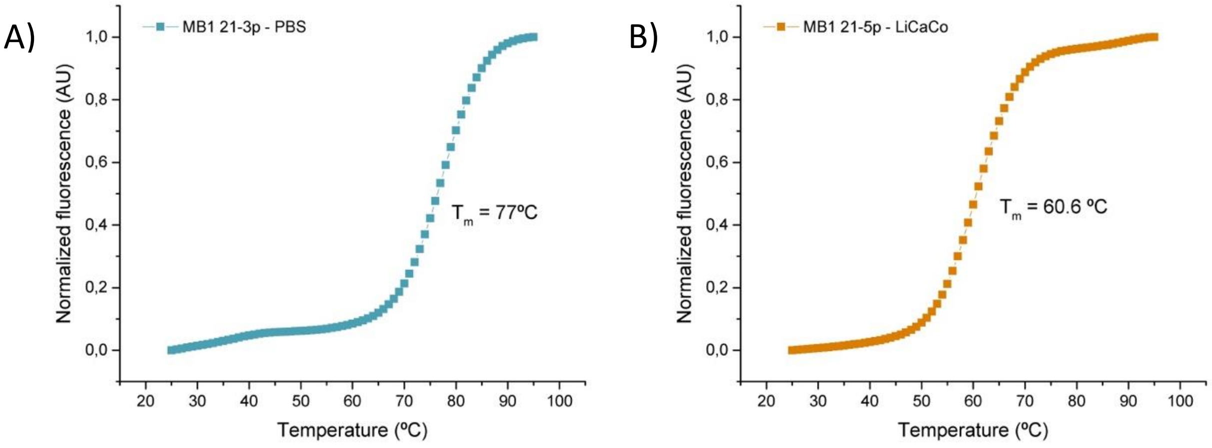

Figure 48. MB1 21-5p FRET curves and T_m. A) MB1 21-5p FRET melting in 1×PBS. B) MB1 21-5p FRET melting in lithium cacodylate.

Referred donor-acceptor split indicates the MB1 21-5p stem-loop unfold to random coil. MB1 21-5p T_m in PBS was 77ºC and in lithium cacodylate was 60.6ºC, showing the more stable profile in PBS rather than in lithium cacodylate just as in MB1 21-3p FRET melting results discussed in chapter 4.4.1.1 - FRET / Reverse FRET melting. Furthermore, lithium cacodylate plays a more destabilizing role in folded structures, reason why MB T_m are lower in comparison with PBS [253]. MB1 21-5p T_m predicted value through software simulations (63.4ºC) do not correspond to the actual MB1 21-5p T_m value in PBS (77ºC), which is explained by predicting model limitations on T_m determination in solution buffers such as PBS.

Using MB structure fold simulation studies as basis in chapter 4.3 - Designed MB dynamics, it is noted that MB1 21-5p was the only MB capable of reproducing the standard MB stem-loop arrangement in software predictions. While MBs 1,2 and 3 21-3p supposedly loop constituted by miR-21-3p complementary sequence as folded into a duplex due to nucleotide pairing, MB1 21-5p loop region formed by miR-21-5p complementary sequence developed a loop structure with a small stem-loop and the top. Furthermore, MB1 21-5p loop formation possibility is connected to a less stable conformation regarding MBs 21-3p 13 nucleotide stem configuration, which will lead to a lower MB1 21-5p T_m. MB1 21-5p T_m on PBS was the most lower regarding all the MBs used in this work, result that might relate to the reported MB1 21-5p distinct configuration.

Reverse FRET melting experiments were performed in MB1 21-5p, wherein the starting temperature is 95ºC, and fluorescence is monitored throughout MB sample cooling until 25ºC. MB1 21-5p FRET and reverse FRET melting curve data is depicted in Figure 49 down below.

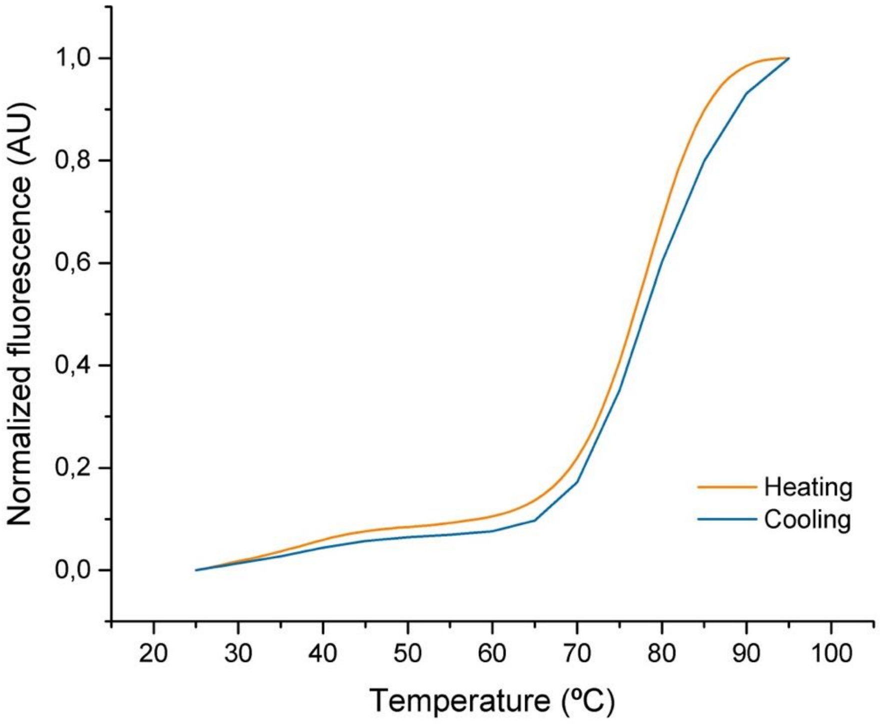

Figure 49. FRET and reverse FRET melting curves of MB1 21-5p. Fluorescence was monitored from 25ºC to 95ºC, returning to 25ºC in reverse FRET melting.

As noticed in Figure 49, MB1 21-5p reverse FRET melting curve is similar to the FRET melting curve. Its profile upon MB1 21-5p heating is equal to the cooling one, showing the MB1 21-5p open mechanism in FRET melting, and the further stem-loop conformation regain under cooling in reverse FRET melting.

4.6.1.2 Circular dichroism (CD)

CD assays were conducted for MB1 21-5p at 10 μM in 1x PBS in order to study the MB structure folding and further nucleic acid disposition [205], [211]. CD melting experiments were also made in MB1 21-5p, however no relevant data was obtained for T_m calculation. Figure 50 reveal MB1 21-5p CD spectra.

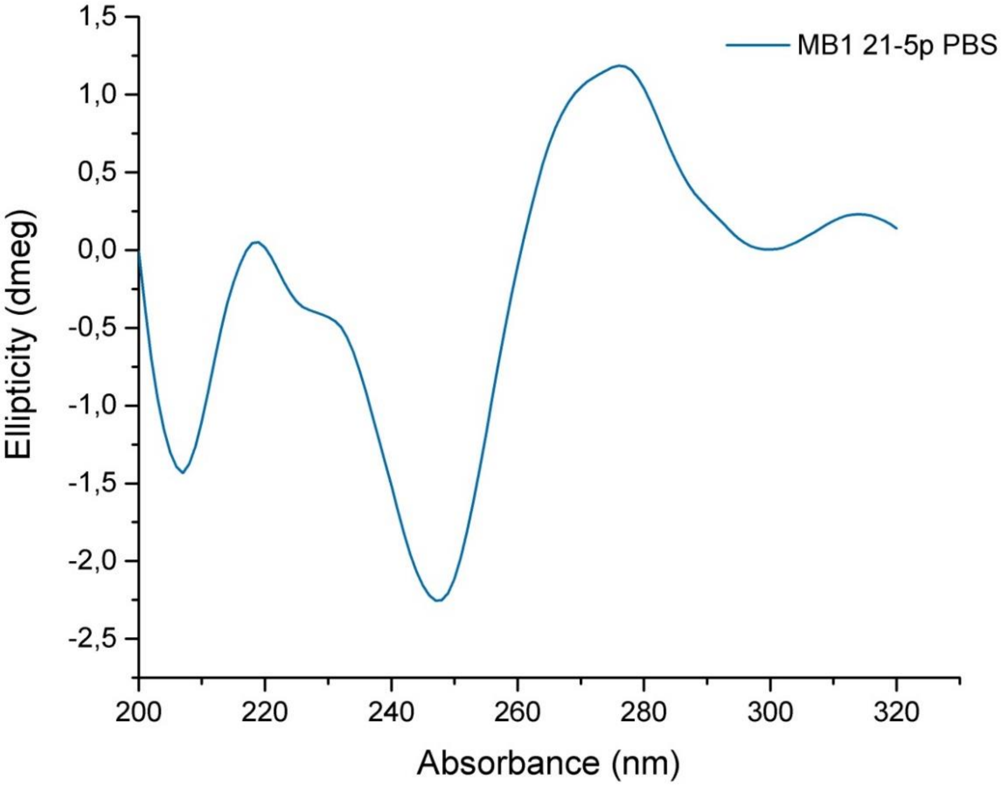

Figure 50. MB1 21-5p CD spectra in PBS. CD spectra measurements were obtained at 20ºC in a 200-320 nm range within 4 accumulations.

It is noted in Figure 50 the signature DNA double helix secondary structure profile with a negative band at approximately 245 nm, and a further positive band at 274 nm. Acquired MB1 21-5p CD spectra resemble the MB stem region constituted by DNA oligonucleotides in the double helix conformation [209], [211]. Besides MB1 21-5p different structure arrangement that promote a hairpin formation at the MB loop region, the correspondent CD spectra was similar to the other MBs spectra in which the hairpin establishment was not favored.

4.6.1.3 Nuclear magnetic resonance (NMR)

The unfolding of MB1 21-5p was also studied by NMR spectroscopy with temperature variation. MB1 21-5p NMR spectra was acquired in a 25ºC-60ºC temperature range, and NMR spectra results for MB1 21-5p are depicted in Figure 51.

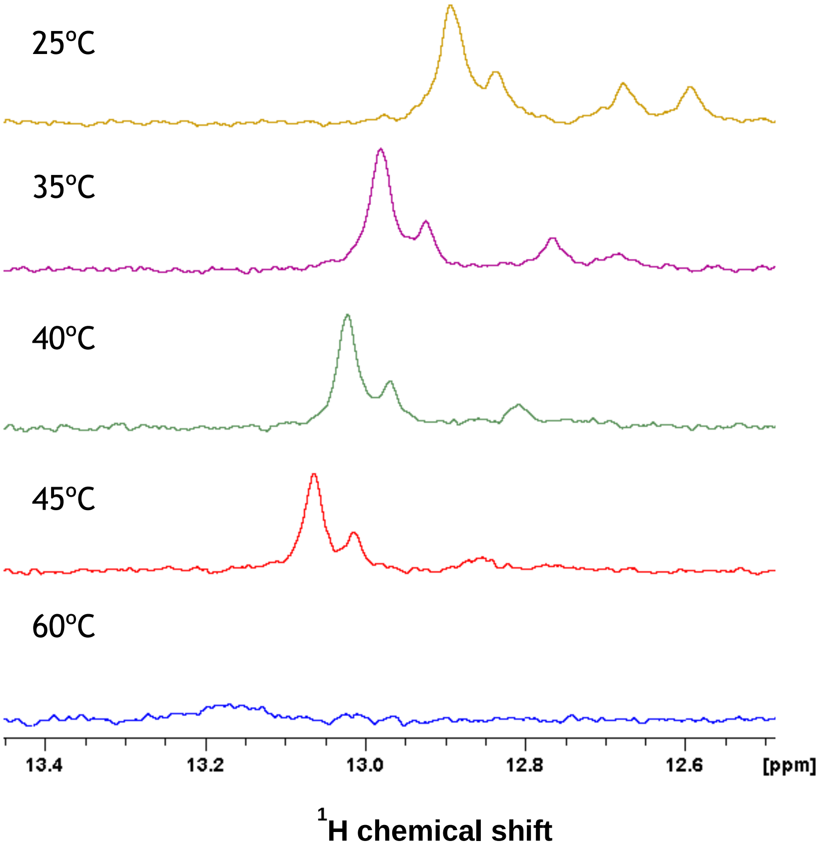

Figure 51. MB1 21-5p NMR spectra with temperature variation. Displayed spectra only comprises the stem region where the MB specific signals are present.

In Figure 51, it is visible two peaks in between 12.6-12.8 ppm that correspond to the hairpin region of the MB, and an additional more intense peak at around 13 ppm equivalent to the stem area. With temperature increase, it is visible that the first signals to vanish are the 12.6-12.8 ppm loop region ones, indicating the MB unfold from the loop towards the stem. Signature MB signals are no longer visible at 60°C, suggesting the total MB1 21-5p unfold into random coil [219], [254]–[257]. Moreover, MB1 21-3p unfold with temperature increase was also visible in previous FRET melting assays.

4.6.2 Interaction studies

The following chapter 4.6.2 - Interaction studies discusses MB1 21-5p hybridization assays results with the corresponding miR-21-5p synthetic sequence and biological samples.

4.6.2.1 MB1 21-5p hybridization assays optimization

Optimization assays were done in MB1 21-5p, in which hybridization temperature and fluorescence read time were screened according to previous MB optimization assays for prime MB1 21-5p hybridization rates. MB1 21-5p hybridization temperature was examined in 50-65ºC temperature range, based on the previous calculated MB1 21-5p T_m of 77ºC. Fluorescence was read in the two microplate readers used along with the study, and protocol procedures were performed according to previous MB hybridization optimization experiments. Figure 52 exhibits fluorescence levels of MB1 21-5p with synthetic miR-21-5p, in which MB1 21-5p basal fluorescence levels were discounted.

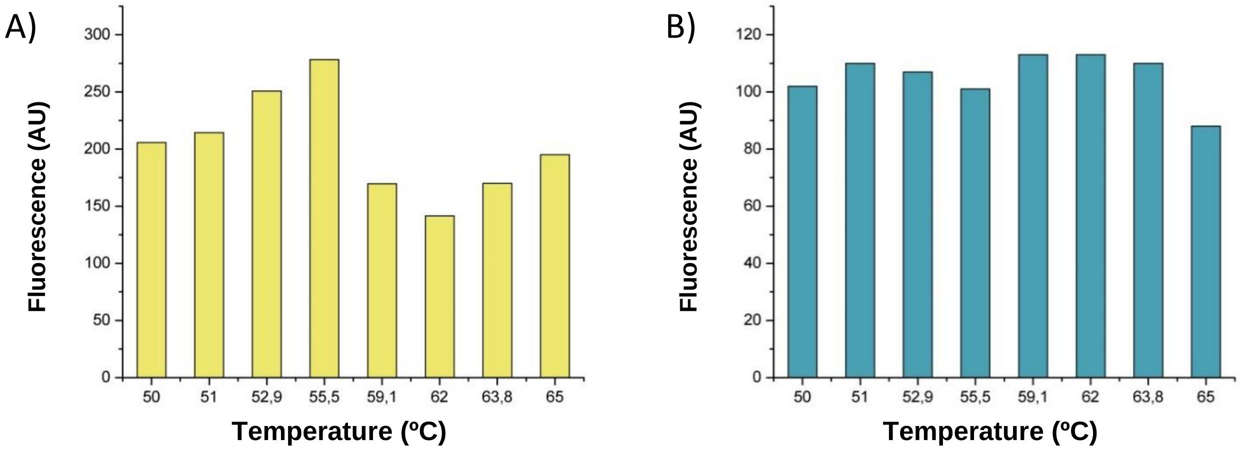

Figure 52. MB1 21-5p hybridization temperature screening assays. A) MB1 21-5p fluorescence reading in Plate reader 1. B) MB1 21-5p fluorescence reading in Plate reader 2. Fluorescence data got MB1 21-5p basal fluorescence discounted (n=1).

Fluorescence data displayed in Figure 52, A and B indicate that in both microplate readers, fluorescence values for MB1 21-5p with miR-21-5p samples were higher than solo MB1 21-5p basal levels, considering that the presented fluorescence data had the basal MB1 21-5p fluorescence deducted. Moreover, positive results supporting MB1 21-5p hybridization towards miR-21-5p were achieved by the two readers, in contrary to what happened in the previous MB1 21-3p hybridization optimization results discussed in chapter 4.4.2.1 - MB1 21-3p hybridization assays optimization, wherein one reader provided positive results and the other negative values in MB with miRNA samples.

In figure 52, A, the maximum fluorescence was reached when MB1 21-5p was incubated with miR-21-5p at 55.5ºC. Further Figure 52, B fluorescence measurements in Plate reader 2 showed highest fluorescence levels at both 59.1ºC and 62ºC. Pursuant fluorescence collected data, the better MB1 21-5p hybridization rates were achieved in between 55.5ºC and 62ºC, suggesting that temperatures within this range favor greater MB1 21-5p/miR-21-5p hybridization. MB1 21-5p hybridization ability is corroborated by the previously reported results, in which samples containing MB1 21-5p reached higher fluorescence values. An additional fluorescence assay was performed to explore MB1 21-5p specificity towards miR-21-5p. MB1 21-5p was incubated with 0.2 μM of miR-21-5p and with miR-21-3p, the other correspondent miR-21 strand which is presumably not targetable by MB1 21-5p.

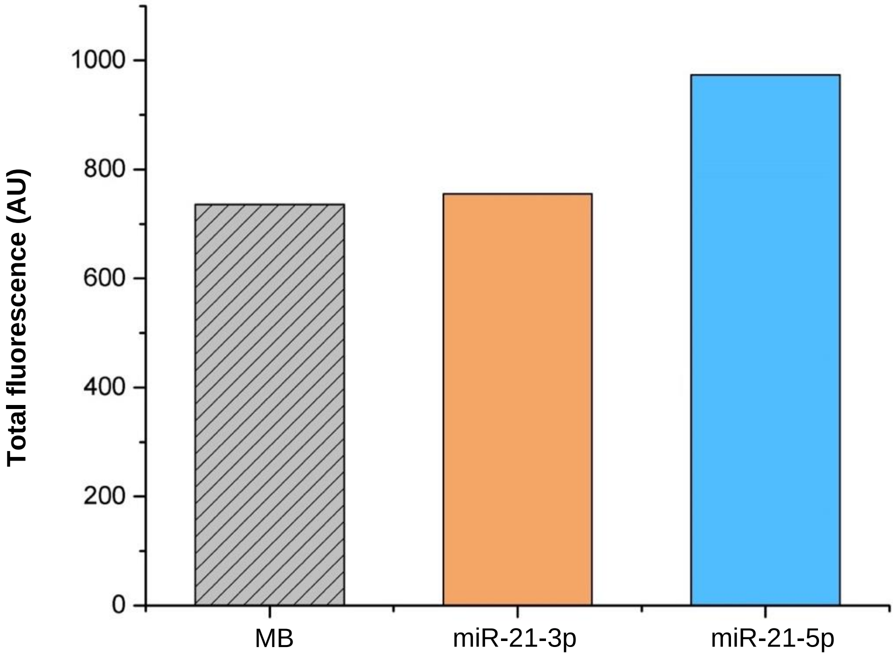

Figure 53. MB1 21-5p hybridization with miR-21-5p and non-specific miR-21-3p. Fluorescence is represented in total values measured in Plate reader 1, regarding MB: MB1 21-5p basal fluorescence, MB1 21-5p + miR-21-3p and MB1 21-5p + miR-21-5p (n=1).

Figure 53 depicts MB1 21-5p total fluorescence data with miR-21-3p and miR-21-5p synthetic sequences. MB1 21-5p with miR-21-3p reached almost MB basal levels, moreover MB1 21-5p together with the specific miR-21-5p attained significant higher fluorescence relatively to single MB. Furthermore, reported results support MB1 21-5p specific hybridization unto miR-21-5p.

4.6.2.2 FRET / Reverse FRET melting

Samples including MB1 21-5p and the miR-21-5p were prepared and applied in FRET and reverse FRET melting assays in the interest of analyzing MB1 21-5p curve profile in presence of synthetic miR-21-5p. A regular FRET / reverse melting protocol was used, where fluorescence levels were measured in the first heating step until 95°C, and further in the cooling reverse FRET melting stage. Three samples comprising single MB1 21-5p at 0.2 μM, MB1 21-5p with miR-21-5p at 0.2 μM, and at 0.4 μM, were prepared in duplicate and followed into FRET / reverse FRET melting assays.

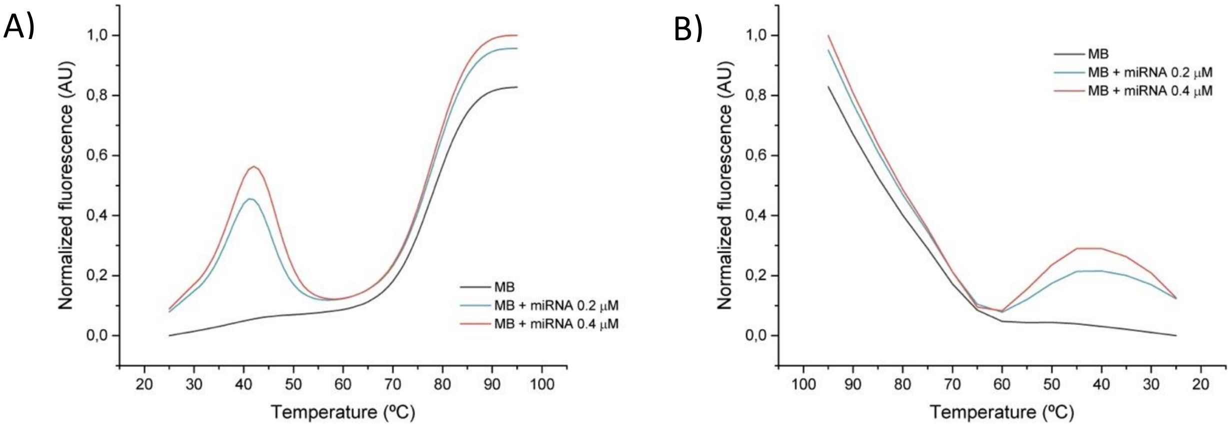

Figure 54. MB1 21-5p with miR-21-5p (0.2 and 0.4 μM) FRET and reverse FRET melting results. A) MB1 21-5p FRET melting curve with miR-21-5p. B) MB1 21-5p reverse FRET melting curve with miR-21-5p. Fluorescence was monitored from 25°C to 95°C, returning to 25°C in reverse FRET melting.

In Figure 54, melting curves of single MB1 21-5p, and jointly with synthetic miR-21-5p are displayed, in which samples containing MB1 21-5p and the correspondent miR-21-5p exhibited a fluorescence peak at 41°C. Single MB1 21-5p FRET / reverse FRET melting curve has a regular profile and resembles previous MB1 21-5p assays above presented in chapter 4.6.1.1 - FRET / Reverse FRET melting. However, the synthetic miR-21-5p addition to MB1 21-5p changed the melting curve profile, in which a fluorescence spike was generated at lower temperatures.

Firstly, starting fluorescence levels in MB1 21-5p with miR-21-5p were higher than MB1 21-5p alone. With temperature increase, a proportional fluorescence variation starts to build up until reaching a band at 41°C, which is higher for 0.4 μM miR-21-5p. Subsequent temperature raise led to this specific fluorescence band reduction, followed by the MB unfold characteristic fluorescence increase at higher temperatures. A similar behavior is observed in reverse FRET melting stage with fluorescence reduction over temperature cooling, and fluorescence band appearance at 41°C, such as in the FRET curve. Furthermore, the demonstrated early fluorescence band before the typical fluorescence profile concerning MB dismantlement was not noticed in MB1 21-3p previous FRET / reverse FRET melting experiments together with the synthetic miR-21-3p sequence, presented in chapter 4.4.2.2 - FRET / Reverse FRET melting.

An additional FRET melting assay was performed with MB1 21-5p mixed with the correspondent synthetic miR-21-5p, and with a non-specific MB1 21-5p target represented by the miR-21-3p. The objective of the following experiment was to verify the MB1 21-5p specificity towards miR-21-5p, by analyzing MB1 21-5p FRET curve behavior with miR-21-3p.

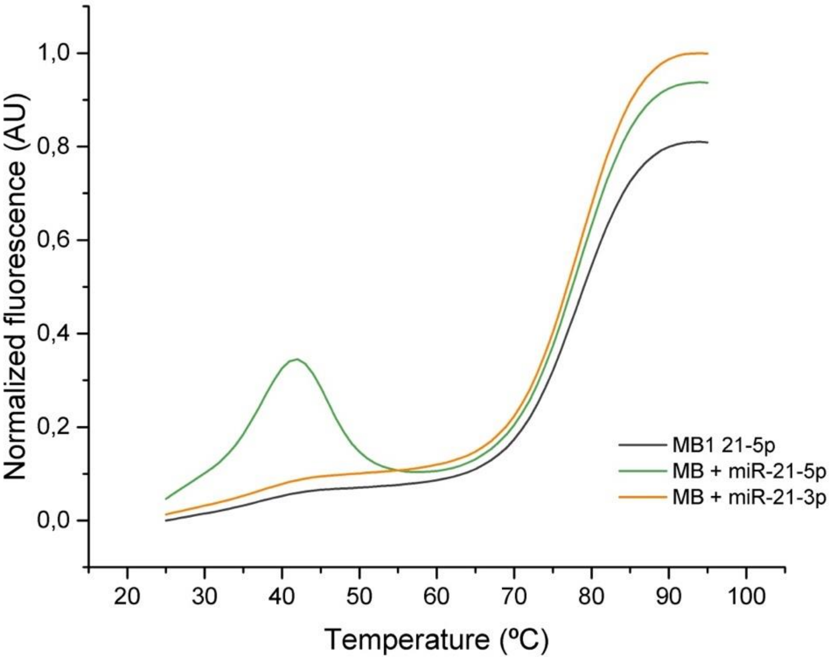

Figure 55. FRET and reverse FRET melting curves for MB1 21-5p with miR-21-5p (0.2 μM) and a non-specific miR-21-3p (0.2 μM) target.

Figure 55 shows FRET melting results on MB1 21-5p with miR-21-5p and miR-21-3p. MB1 21-5p displayed the signature 41ºC fluorescence peak in presence of the correspondent miR-21-5p. When along with miR-21-3p, MB1 21-5p depicted the same FRET curve profile as the MB1 21-5p alone, suggesting that synthetic miR-21-3p does not enhance structural transformations in MB1 21-5p like miR-21-3p. Furthermore, this assay provided evidence that supports MB1 21-5p specificity for miR-21-5p.

Above reported fluorescence band in MB1 21-5p with correspondent miR-21-5p shows that the miRNA addition to the MB influenced, in this case, MB1 21-5p structural dynamics and folding kinetics by interacting with miR-21-5p. Moreover, MB1 21-5p and miR-21-5p interplay is supported by the achieved fluoresce peak at pre-melting temperatures, as well as by the higher fluorescence peak in presence of miR-21-5p larger concentrations, evidence that most likely results from MB1 21-5p hybridization towards the specific miR-21-5p target. Exploring MB1 21-5p hybridization dynamics, an MB1 21-5p fluorescence increase is connected to MB conformational shifting by fluorophore-quencher disunion, resulting in higher fluorescence levels. The higher fluorescence values of MB1 21-5p / miR-21-5p containing samples already suggest MB1 21-5p conformation changes caused by the miR-21-5p presence and further MB1 21-5p hybridization at low temperatures (25ºC). Moreover, these fluorescence differences start to increase, and a maximum fluorescence peak is reached at 41ºC, indicating a stronger and more favorable MB1 21-5p /miR-21-5p hybridization with temperature increase up to 41ºC. However, the fluorescence intensity dropped down with temperature heating beyond 41ºC, reaching similar single MB1 21-5p fluorescence levels. This fluorescence reduction presupposes an MB1 21-5p stem-loop structure retake through MB donor and acceptor coupling, and subsequently a no longer hybridized MB1 21-5p conformation [193], [250].

Fluorescence downgrade phenomenon might be explained through MB1 21-5p structure dynamics and kinetics connection with temperature variation. As seen in FRET / reverse FRET melting MB assays, a temperature increase will enhance MB unfold from the native stem-loop conformation to total random coil arrangement. Hereupon, temperature variation leads to MB conformational changes, wherein a certain temperature favors a specific MB structure. At 25ºC, the stem-loop MB1 21-5p structure is predominant as result of a more stable conformation favored by a lower temperature. However, in presence of miR-21-5p, a temperature increases up to 41ºC will lead to MB1 21-5p hybridization as evidenced by the FRET curve fluorescence spike. Thereafter, a fluorescence declines along with temperature increasing denote no longer MB1 21-5p / miR-21-5p hybridization, which could be connected to the fact that in between 50ºC-70ºC, the most energetic favorable MB1 21-5p structure is the closed stem-loop one, even with miR-21-5p in solution. After 70ºC, MB1 21-5p starts to open until reaching maximum fluorescence levels associated with the whole MB1 21-5p population unfold into random coil [193], [250].

Results on MB1 21-5p showed a 41ºC fluorescence band prior to MB melting when miR-21-5p was added, plus a more intense peak relatively to higher miR-21-5p concentrations, meaning that miR-21-5p addition influenced MB1 21-5p standard melting profile by interacting with MB1 21-5p. Furthermore, the MB1 21-5p / miR-21-5p interaction is related with MB1 21-5p hybridization kinetics, which seems to reach maximum hybridization rate at 41ºC. Temperatures beyond 41ºC appeared to prompt MB1 21-5p / miR-21-5p complex rupture, and further favor MB1 21-5p stem-loop conformation until around 70ºC, temperature where MB1 21-5p will start to open up to fully random coil at 95ºC. Additionally, MB1 21-5p FRET melting results with synthetic miR-21-3p support MB1 21-5p specificity towards the expected target (miR-21-5p).

4.6.2.3 SDS-PAGE electrophoresis

In contemplation of studying MB1 21-5p hybridization capacity, SDS-PAGE electrophoresis assay was performed based on the previous experiment in MB1 21-3p previously discusses on chapter 4.4.2.3 - SDS PAGE electrophoresis.

Three sets were prepared, where each one included miR-21-5p (10 μM), MB1 21-5p (10 μM), MB1 21-5p (10 μM) with 1 equivalent of miR-21-5p (10 μM), and MB1 21-5p (10 μM) with 2 equivalents of miR-21-5p (20 μM). Each set was incubated at different temperatures, 25ºC, 40ºC, and 60ºC.

Displayed gel in Figure 56 from MB1 21-5p SDS-PAGE hybridization studies shows lanes 1 and 2 single miR-21-5p and MB1 21-5p samples. The 20 kDa band in lanes 1 corresponds to miR-21-5p, and the slightly heavier band around 23 kDa is relative to MB1 21-5p. In lanes 2, it also visible a less intense band around 60 kDa that may correspond to higher-weight MB1 21-5p aggregate complexes formed among MB1 21-5p. Lanes 3 and 4 had MB1 21-5p + miR-21-5p (1:1) and (1:2) respectively. Both lanes 3 and 4 show a smeared band at 60 kDa, and lanes 3 have another weak intense band at 23 kDa, and in lanes 4 a significant band at 20 kDa as well. The smeared profile from the 60 kDa band along with the tenuous 50 kDa band below in lanes 3 and 4 could be related to MB1 21-5p hybridization with miR-21-5p products.

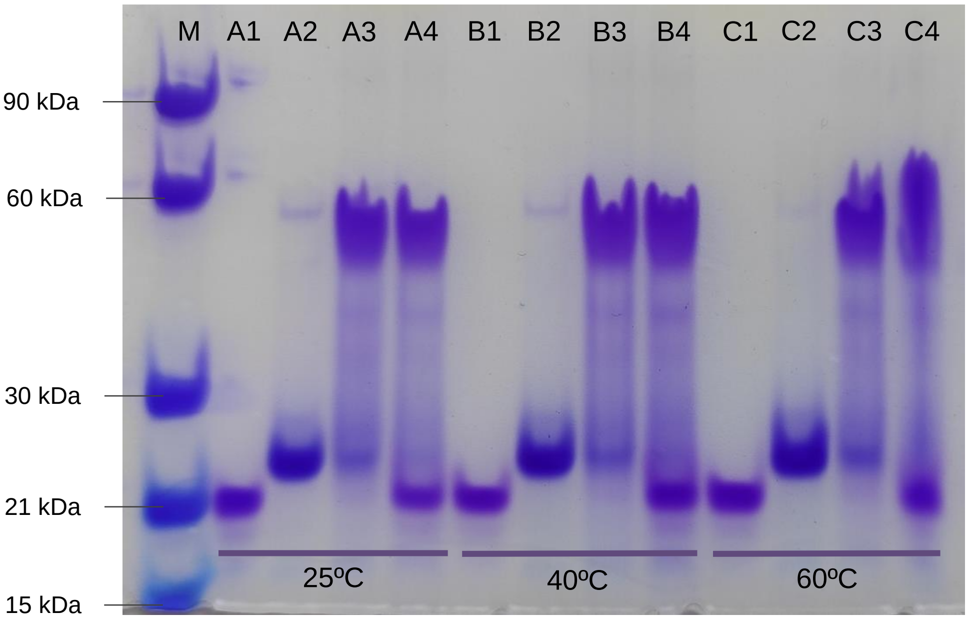

Figure 56. MB1 21-5p hybridization SDS-PAGE electrophoresis gel results. M: Weight marker; A: 25ºC incubation sample set; B: 40ºC incubation sample set; C: 60ºC incubation sample set; 1: miR-21-5p (10 μM); 2: MB1 21-5p (10 μM); 3: MB1 21-5p (10 μM) + miR-21-5p (10 μM); 4: MB1 21-5p (10 μM) + miR-21-5p (20 μM).

MB1 21-5p hybridization with the correspondent synthetic miR-21-5p generates higher molecular height complexes, in which the band smear might represent multiple MB1 21-5p / miR-21-5p complexes that resulted from hybridization processes. In addition, lanes 3 had MB1 21-5p and miR-21-5p at the same concentration (10 μM), which in the respective band profile is not visible the miR-21-5p 20 kDa characteristic band, indicating that miR-21-5p hybridized with MB1 21-5p. Moreover, in lanes 3 is visible a tenuous band near 23 kDa which belongs to remaining MB1 21-5p that did not hybridize. Regarding lanes 4, the same smeared band profile is evident, although the signature 20 kDa band from miR-21-5p is also visible. Such miR-21-5p band emergence is most likely connected with non-hybridized miR-21-5p products, considering that in lanes 4 miR-21-5p was at a double concentration (20 μM) in comparison to MB1 21-5p, showing that miR-21-5p at a two-time higher concentration relatively to MB1 21-5p overpass MB1 21-5p maximum hybridization capacity. Also supporting the option that in lanes 4 MB1 21-5p maximum was reached, in contrary to lanes 3, the corresponding MB1 21-3p band was not present in lanes 4, which makes it possible to conclude that all MB1 21-5p have hybridized as is present in the higher molecular height band at 60 kDa [224].

Noting that in the previous SDS-PAGE electrophoresis assay concerning MB1 21-3p hybridization study, the MB1 21-3p band profile did not present any modification when the correspondent miR-21-3p was added, showing that the presented results support the MB1 21-5p hybridization with miR-21-5p.

4.6.2.4 NMR spectroscopy

MB1 21-5p and synthetic miR-21-5p were prepared and further studied in the NMR spectroscopy technique for MB-miRNA hybridization investigation. Changes in the specific NMR spectra MB signals could be related with hybridization dynamics within the MB1 21-5p and miR-21-5p. Figure 57 shows the NMR spectra for MB1 21-5p with miR-21-5p at different concentrations at 40ºC.

As observed in Figure 57, the addition of 1.5 equivalent to the MB1 21-5p did interfere in the characteristic stem-loop MB signals between 13.2-12.5 ppm. Moreover, the addition of 2 equivalent of miR-21-5p basically led to signal disappearance.

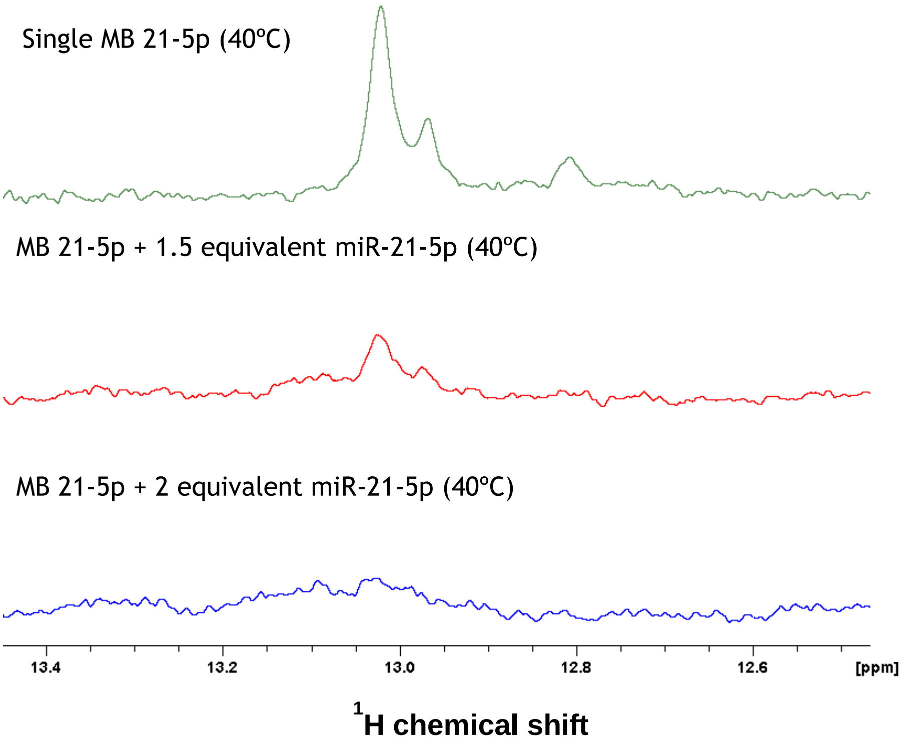

Figure 57. MB1 21-5p NMR spectra with miR-21-5p. Spectra acquisition was performed at 40°C with single MB1 21-5p, and with MB + 1.5 and 2 equivalents of miR-21-5p. Displayed spectra only comprises the stem-loop region where the MB specific signals are present.

This means that MB1 21-5p and miR-21-5p interplay in hybridization dynamics, as seen by the signature MB signal shift and lower signal alongside with the addition of the miRNA [216], [254]–[257]. Collected NMR data on MB1 21-5p with synthetic miR-21-5p meet the previous FRET melting and SDS-PAGE electrophoresis results, wherein evidence of MB1 21-5p hybridization towards miR-21-5p was obtained.

4.6.2.5 MB1 21-5p hybridization enhancement

Previous interaction study results on MB1 21-5p FRET and reverse FRET melting assays with miR-21-5p showed a fluorescence peak at 41°C for samples with MB1 21-5p and miR-21-5p. Thus, former optimization studies on MB1 21-5p were not performed in the optimal temperature range (50-65°C) for MB1 21-5p hybridization, which led to further optimization of MB1 21-5p hybridization assays comprising an incubation step at 41°C for maximum MB1 21-5p hybridization rates. MB1 21-5p with miR-21-5p samples were prepared, incubated at 95°C for 10 min, and subsequently at 41°C for 10 min in the hybridization step. Fluorescence readings were made at different equipment temperatures (25-45°C) and times after reaching 45°C to analyze fluorescence differences connected with reading temperature variation.

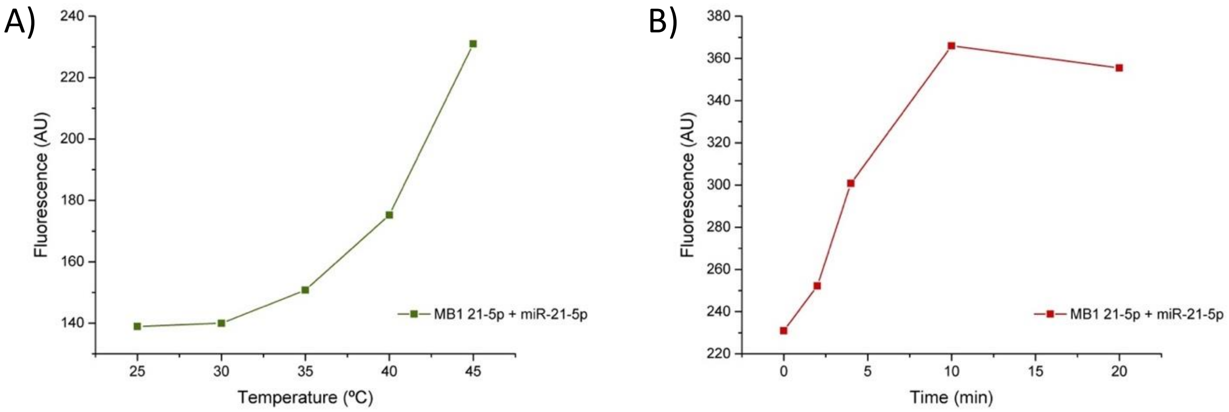

Figure 58. MB1 21-5p hybridization optimization assays. A) MB1 21-5p fluorescence data over temperature variation. B) MB1 21-5p fluorescence data over time after reaching 45°C. MB1 21-5p basal fluorescence values were deducted from presented fluorescence data measured in Plate reader 1.

Figure 58, A and B presents fluorescence results on MB1 21-5p hybridization optimization experiments upon fluorescence reading at the microplate equipment. In Figure 58, A, the higher fluorescence difference between MB1 21-5p alone and MB1 21-5p with miR-21-5p was reached at 45°C. Although, despite the equipment given information regarding temperature, it is important to note that the displayed temperature may not correspond to the actual sample temperature. Furthermore, upon reaching 45°C, samples fluorescence was read for 20 min. Figure 58, B show that 10 min after reaching 45°C, higher fluorescence differences arise, but 20 min later fluorescence levels start to lower. These results suggest that 10 min after arriving to 45°C, the internal equipment temperature is actually 41°C according to the maximum fluorescence peak in previous MB1 21-5p FRET / reverse melting results. At 20 min, internal equipment temperature is higher than 41°C, which lead to a fluorescence decreasing as result of MB1 21-5p optimal hybridization temperature overstep.

Further MB1 21-5p hybridization assays were performed based on results from the presented optimization studies. After incubation, samples were read at the equipment temperature of 45°C after 10 min, corresponding to previous fluorescence maximal output.

4.6.2.6 *In situ* MB1 21-5p - miRNA detection

MB1 21-5p *in situ* miR-21-5p detection experiments were carried out in accordance with previous hybridization optimizations. Biological samples were incubated with MB1 21-5p at 95°C for 10 min, followed by the hybridization step at the optimal hybridization temperature (41°C) for 10 min as well. Samples were further transferred to a 96 well microplate for fluorescence-based assays, and fluorescence was read 10 min after the equipment reached 45°C, as optimized in preceding experiments.

A MB1 21-5p hybridization assay with RT-qPCR products from NHDF and A549 cell lines was executed to study MB1 21-5p hybridization ability with RT-qPCR products. Previous MB1 21-3p hybridization experiments with RT-qPCR products showed that the SYBR Green present in PCR products did interfere with fluorescence measurements, due to SYBR Green excitation and emission wavelength (λ_{ex} = 497 nm; λ_{em} = 520 nm) convergence with the MB1 21-5p fluorophore FAM (λ_{ex} = 495 nm; λ_{em} = 520 nm). However, contrary to MB1 21-5p, it was concluded that MB1 21-3p had hybridization limitations towards the specific miR-21-3p target. Thus, MB1 21-5p positive hybridization results open a possibility concerning the use of RT-qPCR use in hybridization assays. Figure 59 describe total fluorescence from MB1 21-5p hybridization using control and NSCLC RT-qPCR products.

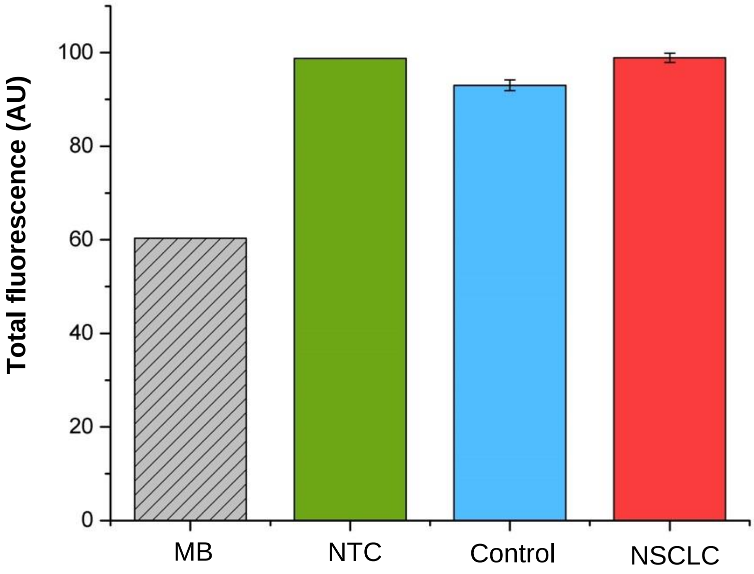

Figure 59. MB1 21-5p control and NSCLC RT-qPCR products hybridization assays. MB: MB1 21-5p; NTC: MB1 21-5p + NTC RT-qPCR product; Control: MB1 21-5p + control RT-qPCR product (n=9); NSCLC: MB1 21-5p + NSCLC RT-qPCR product (n=15). Total fluorescence results were acquired in Plate reader 2 (± SE).

Figure 59 shows total fluorescence values from the MB1 21-5p hybridization assay with NHDF and A549 RT-qPCR products, wherein is observed that the non-amplified NTC product had similar fluorescence levels in comparison with the amplified NHDF and A549 products. These results meet previous MB1 21-3p hybridization with RT-qPCR products results, in which the NTC also exhibited fluorescence values near to the amplifying RT-qPCR products. Furthermore, it is confirmed that even in the hybridization functional MB1 21-5p, hybridization assays including specific miRNA RT-qPCR products is not practicable as result of SYBR interference in MB1 21-5p FAM fluorescence readings.

Considering the null hypothesis on the use of RT-qPCR products in FAM labelled MBs, further hybridization studies were performed using total RNA from biological samples. Firstly, MB1 21-5p was hybridized to 1000 µg and 2000 µg total RNA from NHDF cell line to study hybridization differences related to larger RNA quantities.

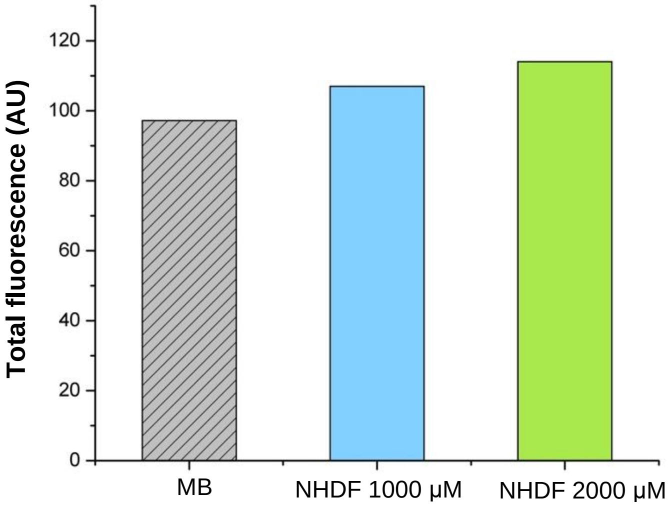

Figure 60. MB1 21-5p hybridization assays at different NHDF RNA concentrations. Fluorescence data is represented as total fluorescence measured values in the Plate reader 2 (n=1).

Figure 60 shows MB1 21-5p fluorescence values upon NHDF RNA hybridization at 1000 µg and 2000 µg. Slightly higher fluorescence values were confirmed for NHDF at 2000 µg, showing that a higher RNA input could lead to significant fluorescence differences. Furthermore, according to Baker *et al.*, more relevant hybridized MB fluorescence levels were verified in samples with RNA concentrations above 1000 µg [197]. Further MB1 21-5p hybridization assays with NHDF and A549 cell lines were conducted using 2000 µg of total RNA, attending to the higher RNA yields in cell lines in comparison to PBMCs, and to the possible higher fluorescence differences connected with the use of higher total RNA concentrations.

As observed in Figure 61, MB1 21-5p hybridization with RNA from A549 cell lines achieved superior fluorescence levels in relation to MB1 21-5p with NHDF RNA. MB1 21-5p with 2000 µg of total RNA from A549 cell lines reached 360.6 fluorescence units, although MB1 21-5p with 2000 µg of total RNA from NHDF cell lines achieved 275 fluorescence units.

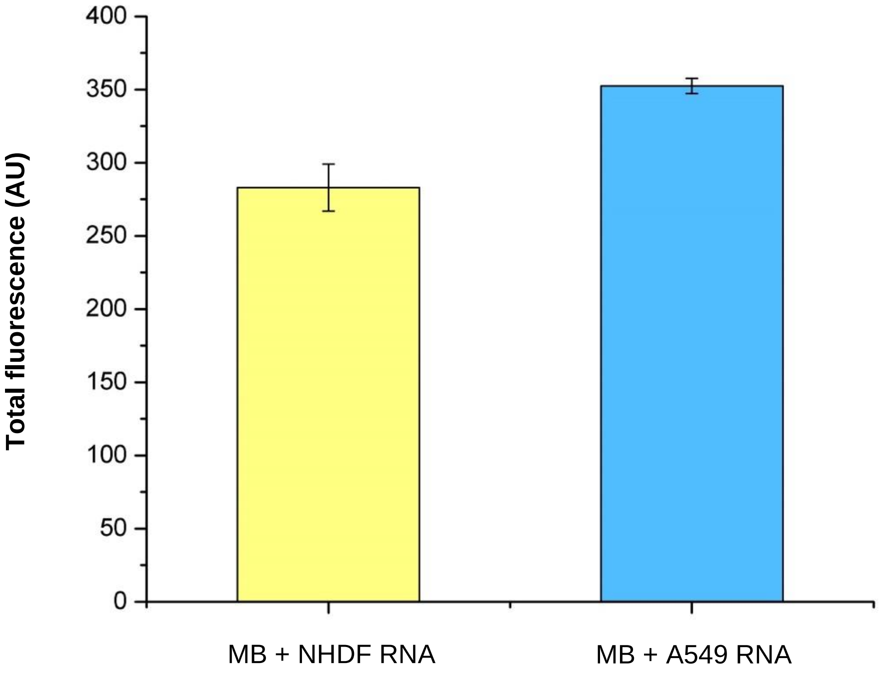

Figure 61. MB1 21-5p NHDF and A549 RNA hybridization assays. Fluorescence data is represented as total fluorescence measured values in Plate reader 1 (n=3, ± SE).

Higher total RNA concentrations used in MB1 21-5p hybridization assays with cell lines generated considerable fluorescence differences between NHDF and A549 cell lines, supporting the previously confirmed miR-21-5p overexpressed profile in A549 by RT-qPCR assays presented in chapter 4.2.2 - RT-qPCR assays.

MB1 21-5p hybridization assays with total RNA from NSCLC and healthy PBMCs were realized with 500 µg of total RNA, due to low RNA concentrations yields from 1 × 10^6 PBMC cells using the miRNeasy Micro Kit. In order to reach a considerable amount of NSCLC and control samples in MB1 21-5p hybridization assays, only a 500 µg of extracted total RNA was achievable with the employed kit. Furthermore, to reach RNA concentrations from PBMCs around 1000 µg, two extractions for the same individual would be needed, requiring twice as many reagents and materials provided in the employed kit, and further compromising the number of tested samples. Thus, 9 different RNA samples from control PBMCs and 19 NSCLC PBMCs samples were studied in MB1 21-5p hybridization assays.

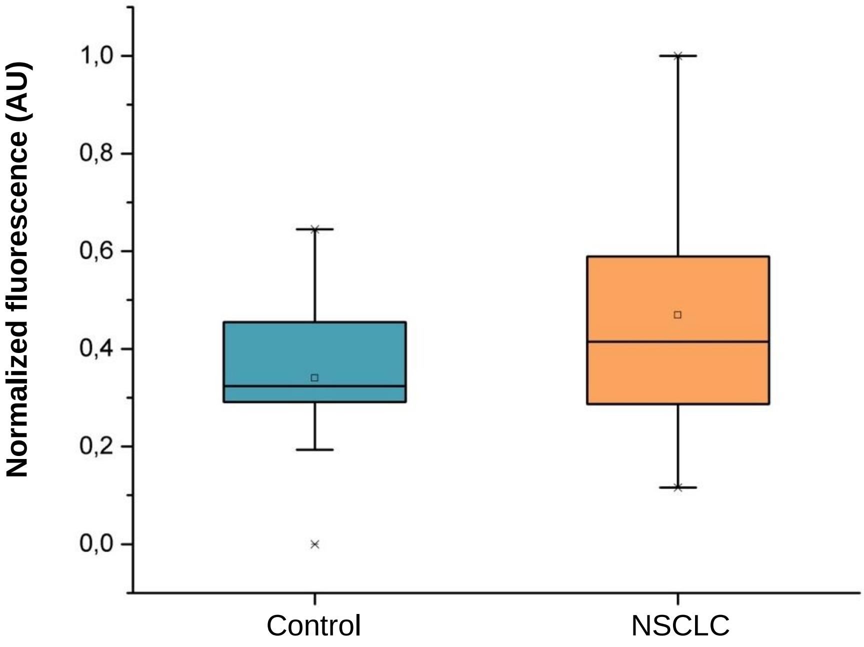

Figure 62. MB1 21-5p hybridization assays with RNA from NSCLC and healthy control PBMCs. Fluorescence levels were measured in the Plate reader 1, further got MB1 21-5p basal fluorescence deducted, and were normalized to 1. Samples in study comprised: healthy control group (n=9); NSCLC group (n=19).

Figure 62 represents MB1 21-5p hybridization with NSCLC and control PBMCs total RNA at 500 µg, wherein a higher fluorescence tendency is visible in NSCLC PBMC samples. Increased fluorescence levels in NSCLC PBMCs RNA indicate a higher miR-21-5p expression in the NSCLC PBMCs population, showing concordance with the miR-21-5p up-regulated profile in RT-qPCR assays. Moreover, even at low concentrations (500 µg), MB1 21-5p hybridization into miR-21-5p results in NSCLC PBMCs showed an upper fluorescence trend relatively to healthy control levels. MB1 21-5p miR-21-5p detection was able to discriminate NSCLC patients with reasonable precision, presenting 73.3% sensitivity, 66.7% specificity and a 0.643 AUC value. Besides MB1 21-5p already evidenced ability to hybridize with synthetic miR-21-5p, demonstrated results with low RNA concentrations from NSCLC and healthy PBMCs showed MB1 21-5p potential to properly identify NSCLC cases via their miR-21-5p up-regulated profile.

Current progress made on MB1 21-5p hybridization dynamics study, as well as in the *in situ* detection of miR-21-5p in biological samples, represent MB1 21-5p potential to screen an NSCLC interest biomarker (miR-21-5p), and further integrate an innovative approach for the diagnosis of NSCLC.

CHAPTER 5 – Conclusions and Future Perspectives

5. Conclusions and Future Perspectives

Chapter 5 - Conclusions discloses the work final aftermath, summing up main results and linking them to central objectives. Future perspectives and alternative tracks are taken into count, for the purpose of reaching even more significant results in favor of science thrilling progress.

Early NSCLC diagnosis is key for patient survival, bearing in mind that NSCLC is usually diagnosed at advanced stages and that the precocious NSCLC diagnosis is directly proportional to a better outcome. Additionally, most consistent NSCLC diagnosis methods often comprise risky invasive procedures. NSCLC biomarkers like miRNAs constitute a powerful non-invasive potential target for NSCLC diagnosis. Moreover, miRNA deregulated expression in PBMCs is associated with NSCLC staging and early diagnosis. A miRNA detection strategy based on MBs capable of hybridizing to target miRNAs, and subsequently generate a proportional fluorescent signal, was developed for miRNA detection in NSCLC biological samples.

Total RNA from PBMCs from NSCLC and healthy individuals was extracted and followed to RT-qPCR assays for miRNA screening. miRNA profiling data indicated an up-regulation of miRNAs 21-3p, 21-5p, 155-3p and 3662 in NSCLC PBMC samples, although miRNAs 92b-5p, 150-3p, 155-3p and 181a-5p exhibited an under-expressed profile. miR-21 followed into further studies due to RT-qPCR absolute and relative quantification results. Moreover, a clinical analysis in miR-21 expression concerning NSCLC stage, mutations, and smoking history, indicated that both miR-21 3p and 5p were up-regulated in advanced NSCLC stages, that miR-21-3p was overexpressed in BRAF mutation NSCLC cases, and in the other hand, miR-21-5p was highly expressed in KRAS NSCLC mutants. Additionally, miR-21-3p also revealed an up-regulated profile in NSCLC patients with smoking background.

MBs targeting miRNA sequences 21-3p and 21-5p were designed and optimized in order to detect the correspondent miRNAs in biological samples. MBs targeting miR-21-3p did not demonstrated capacity to hybridize towards their target, as result of the high stable stem-loop structure generated by inner complementary miR-21-3p sequence nucleotide binding, resulting in a 13 highly stable stem configuration that not favored MB-miRNA hybridization.

MB1 21-5p have demonstrated aptitude to hybridize towards the miR-21-5p target in multiple interaction studies. Furthermore, MB1 21-5p also exhibited hybridization specificity to miR-21-5p. Hybridization assays comprising MB1 21-5p with the different miR-21 strand (miR-21-3p) demonstrated that MB1 21-5p did not produce any signal of hybridization with miR-21-3p. The developed MB-based approach using MB1 21-5p shown a proclivity for higher fluorescence levels in NSCLC PBMCs, with a 77.3% ability to identify positive NSCLC cases, and a 66.7% capacity to recognize negative cases, representing congruent results with RT-qPCR regarding miR-21-5p up-regulated profile. Moreover, obtained results are promising concerning NSCLC diagnosis, wherein the developed approach within MB1 21-5p could constitute an additional method for multi-modal NSCLC diagnosis.

Although achieved results constitute prominent advances towards a more specific and correct NSCLC diagnosis, further experimental assays comprising more samples and additional procedure optimizations are needed. Future work perspectives comprehend a larger NSCLC and healthy population. Firstly, a healthy population increase comprising older individuals is important in order to match NSCLC population numbers. Furthermore, a bigger NSCLC and healthy population are essential for RT-qPCR results validation, providing a more robust and significant data on PBMC miRNA profiling. Presented study only counted with NSCLC patients from Covilhã county, so in order to gather more NSCLC samples, prospects regarding a collaboration with a view of gather NSCLC populations from near districts like Castelo Branco, Guarda and Coimbra could bring more NSCLC individuals to the study. *In situ* developed methodology also requires further optimization, in which the employment of higher total RNA concentrations could lead to more significant fluorescence differences between NSCLC and healthy samples. Furthermore, developed MB-based strategy integration in a lab on a chip (LOC) could represent major advantages, considering a more accessible and time valuable NSCLC diagnosis.

Additionally, relevant RT-qPCR results regarding miR-155-3p overexpressed profile in NSCLC PBMCs are already being studied by the group, as well as the MB-based approach enhancement, aiming a more powerful miRNA detection in NSCLC biological samples.

CHAPTER 6 – References

6. References

[1] R. B. Taylor, “The Respiratory System,” in *Diagnostic Principles and Applications*, New York, NY: Springer New York, 2013, pp. 141–160.

[2] J. F. Tomashefski and C. F. Farver, “Anatomy and histology of the lung,” in *Dail and Hammar’s Pulmonary Pathology*, vol. 1, Springer New York, 2008, pp. 20–48.

[3] D. J. Finley and V. W. Rusch, “Anatomy of the Pleura,” *Thoracic Surgery Clinics*, vol. 21, no. 2. pp. 157–163, May 2011.

[4] R. O. McClellan, *Concepts In Inhalation Toxicology*. CRC Press, 1995.

[5] N. E. Robinson and P. W. Furlow, “Anatomy of the respiratory system,” in *Equine Respiratory Medicine and Surgery*, Elsevier Ltd, 2007, pp. 3–17.

[6] D. J. Minnich and D. J. Mathisen, “Anatomy of the Trachea, Carina, and Bronchi,” *Thoracic Surgery Clinics*, vol. 17, no. 4. pp. 571–585, Nov. 2007.

[7] L. Knudsen and M. Ochs, “The micromechanics of lung alveoli: structure and function of surfactant and tissue components,” *Histochemistry and Cell Biology*, vol. 150, no. 6. Springer Verlag, pp. 661–676, Dec. 01, 2018.

[8] C. L. VanPutte, J. L. Regan, and A. F. Russo, “Seeley’s essentials of anatomy & physiology.”

[9] R. G. Crystal, S. H. Randell, J. F. Engelhardt, J. Voynow, and M. E. Sunday, “Airway epithelial cells: Current concepts and challenges,” in *Proceedings of the American Thoracic Society*, Sep. 2008, vol. 5, no. 7, pp. 772–777.

[10] F. Stanke, “The Contribution of the Airway Epithelial Cell to Host Defense,” *Mediators Inflamm.*, vol. 2015, 2015, doi: 10.1155/2015/463016.

[11] L. E. Ostrowski, K. L. Andrews, P. D. Potdar, and P. Nettesheim, “Ciliated-cell differentiation and gene expression,” in *Protoplasma*, 1999, vol. 206, no. 4, pp. 245–248.

[12] C. W. Davis and B. F. Dickey, “Regulated airway goblet cell mucin secretion,” *Annual Review of Physiology*, vol. 70. pp. 487–512, 2008.

[13] P. S. Hiemstra, P. B. McCray, and R. Bals, “The innate immune function of airway epithelial cells in inflammatory lung disease,” *Eur. Respir. J.*, vol. 45, no. 4, pp. 1150–1162, Apr. 2015, doi: 10.1183/09031936.00141514.

[14] P. D. Wagner, “The physiological basis of pulmonary gas exchange: Implications for clinical interpretation of arterial blood gases,” *Eur. Respir. J.*, vol. 45, no. 1, pp. 227–243, Jan. 2015, doi: 10.1183/09031936.00039214.

[15] J. B. West and P. D. Wagner, “Pulmonary gas exchange,” *American Journal of Respiratory and Critical Care Medicine*, vol. 157, no. 4 II SUPPL. American Thoracic Society, pp. 82–87, Dec. 14, 1998.

[16] “Lungs and Respiratory System.” https://physiotherapypedia.com/lungs-and-respiratory-system/ (accessed Oct. 06, 2021).

[17] *Forum of International Respiratory Societies The Global Impact of Respiratory Disease*. 2012.

[18] J. B. Soriano *et al.*, “Prevalence and attributable health burden of chronic respiratory diseases, 1990–2017: a systematic analysis for the Global Burden of Disease Study 2017,” *Lancet Respir. Med.*, vol. 8, no. 6, pp. 585–596, Jun. 2020, doi: 10.1016/S2213-2600(20)30105-3.

[19] J. H. Ryu and P. D. Scanlon, “Obstructive lung diseases: COPD, asthma, and many imitators,” *Mayo Clin. Proc.*, vol. 76, no. 11, pp. 1144–1153, 2001, doi: 10.4065/76.11.1144.

[20] M. Decramer, W. Janssens, and M. Miravitlles, “Chronic obstructive pulmonary disease.,” *Lancet (London, England)*, vol. 379, no. 9823, pp. 1341–51, Apr. 2012, doi: 10.1016/S0140-6736(11)60968-9.

[21] P. J. Barnes, S. D. Shapiro, and R. A. Pauwels, “Chronic obstructive pulmonary disease: Molecular and cellular mechanisms,” *European Respiratory Journal*, vol. 22, no. 4. European Respiratory Society, pp. 672–688, Oct. 01, 2003.

[22] J. W. Mims, “Asthma: Definitions and pathophysiology,” *Int. Forum Allergy Rhinol.*, vol. 5, pp. S2–S6, Sep. 2015, doi: 10.1002/alr.21609.

[23] C. Anandan, U. Nurmatov, O. C. P. Van Schayck, and A. Sheikh, “Is the prevalence of

asthma declining? Systematic review of epidemiological studies," *Allergy: European Journal of Allergy and Clinical Immunology*, vol. 65, no. 2. John Wiley & Sons A/S, pp. 152–167, Feb. 01, 2010.

[24] P. King, S. Holdsworth, N. Freezer, and P. Holmes, "Bronchiectasis," *Internal Medicine Journal*, vol. 36, no. 11. John Wiley & Sons, Ltd, pp. 729–737, Nov. 01, 2006.

[25] N. Saxena, "Restrictive lung disease," in *The Perioperative Medicine Consult Handbook*, Springer International Publishing, 2015, pp. 199–202.

[26] C. C. W. Hsia, "Cardiopulmonary limitations to exercise in restrictive lung disease," *Medicine and Science in Sports and Exercise*, vol. 31, no. 1 SUPPL. American College of Sports Medicine, 1999.

[27] N. Jain, R. Lodha, and S. K. Kabra, "Upper respiratory tract infections," *Indian J. Pediatr.*, vol. 68, no. 12, pp. 1135–1138, 2001, doi: 10.1007/BF02722930.

[28] A. Meneghetti, "Upper Respiratory Tract Infection Medication," *Medscape*, pp. 1–18, Oct. 2015, Accessed: Jun. 15, 2021. [Online]. Available: http://emedicine.medscape.com/article/302460-medication#showall.

[29] K. C. Carroll and L. L. Adams, "Lower Respiratory Tract Infections," *Microbiol. Spectr.*, vol. 4, no. 4, Aug. 2016, doi: 10.1128/microbiolspec.DMIH2-0029-2016.

[30] S. Kinkade and N. A. Long, "Acute bronchitis," *Am. Fam. Physician*, vol. 94, no. 7, pp. 560–565, Oct. 2016, doi: 10.5005/jp/books/10950_9.

[31] J. H. Reynolds, G. McDonald, H. Alton, and S. B. Gordon, "Pneumonia in the immunocompetent patient," *British Journal of Radiology*, vol. 83, no. 996. pp. 998–1009, Dec. 2010.

[32] S. D. Lawn and A. I. Zumla, "Tuberculosis," in *The Lancet*, 2011, vol. 378, no. 9785, pp. 57–72.

[33] J. Shrestha *et al.*, "Lung-on-a-chip: the future of respiratory disease models and pharmacological studies," *Crit. Rev. Biotechnol.*, vol. 40, no. 2, pp. 213–230, Feb. 2020, doi: 10.1080/07388551.2019.1710458.

[34] A. G. Harrison, T. Lin, and P. Wang, "Mechanisms of SARS-CoV-2 Transmission and Pathogenesis," *Trends in Immunology*, vol. 41, no. 12. Elsevier Ltd, pp. 1100–1115, Dec.

01, 2020.

[35] K. Habas *et al.*, "Resolution of coronavirus disease 2019 (COVID-19)," *Expert Review of Anti-Infective Therapy*, vol. 18, no. 12. Taylor and Francis Ltd., pp. 1201–1211, 2020.

[36] S. I. Hajdu, "A note from history: Landmarks in history of cancer, part 1," *Cancer*, vol. 117, no. 5. John Wiley & Sons, Ltd, pp. 1097–1102, Mar. 01, 2011.

[37] I. B. Weinstein and K. Case, "The history of cancer research: Introducing an AACR centennial series," *Cancer Research*, vol. 68, no. 17. pp. 6861–6862, Sep. 01, 2008.

[38] H. Sung *et al.*, "Global Cancer Statistics 2020: GLOBOCAN Estimates of Incidence and Mortality Worldwide for 36 Cancers in 185 Countries," *CA. Cancer J. Clin.*, vol. 71, no. 3, pp. 209–249, May 2021, doi: 10.3322/caac.21660.

[39] B. C. Bade and C. S. Dela Cruz, "Lung Cancer 2020: Epidemiology, Etiology, and Prevention," *Clinics in Chest Medicine*, vol. 41, no. 1. W.B. Saunders, pp. 1–24, Mar. 01, 2020.

[40] J. A. Barta, C. A. Powell, and J. P. Wisnivesky, "Global epidemiology of lung cancer," *Annals of Global Health*, vol. 85, no. 1. Ubiquity Press, 2019.

[41] R. J. Cersosimo, "Lung cancer: A review," *American Journal of Health-System Pharmacy*, vol. 59, no. 7. American Society of Health-Systems Pharmacy, pp. 611–642, Apr. 01, 2002.

[42] M. Duruisseaux and M. Esteller, "Lung cancer epigenetics: From knowledge to applications," *Seminars in Cancer Biology*, vol. 51. Academic Press, pp. 116–128, Aug. 01, 2018.

[43] H. H. Popper, "Progression and metastasis of lung cancer," 2016, doi: 10.1007/s10555-016-9618-0.

[44] D. E. Ost, S. C. J. Yeung, L. T. Tanoue, and M. K. Gould, "Clinical and organizational factors in the initial evaluation of patients with lung cancer: Diagnosis and management of lung cancer, 3rd ed: American college of chest physicians evidence-based clinical practice guidelines," *Chest*, vol. 143, no. 5 SUPPL, 2013, doi: 10.1378/chest.12-2352.

[45] Y. Sekido, K. M. Fong, and J. D. Minna, "Molecular Genetics of Lung Cancer," *Annual Review of Medicine*, vol. 54. Annual Reviews 4139 El Camino Way, P.O. Box 10139,

Palo Alto, CA 94303-0139, USA , pp. 73–87, Nov. 28, 2003.

[46] S. A. Bialous and L. Sarna, “Lung Cancer and Tobacco: What Is New?,” *Nursing Clinics of North America*, vol. 52, no. 1. W.B. Saunders, pp. 53–63, Mar. 01, 2017.

[47] L. R. Zhang *et al.*, “Cannabis smoking and lung cancer risk: Pooled analysis in the International Lung Cancer Consortium,” *Int. J. Cancer*, vol. 136, no. 4, pp. 894–903, Feb. 2015, doi: 10.1002/ijc.29036.

[48] D. Bracken-Clarke *et al.*, “Vaping and lung cancer – A review of current data and recommendations,” *Lung Cancer*, vol. 153. Elsevier Ireland Ltd, pp. 11–20, Mar. 01, 2021.

[49] R. Taylor, F. Najafi, and A. Dobson, “Meta-analysis of studies of passive smoking and lung cancer: Effects of study type and continent,” *Int. J. Epidemiol.*, vol. 36, no. 5, pp. 1048–1059, Oct. 2007, doi: 10.1093/ije/dym158.

[50] J. Malhotra, M. Malvezzi, E. Negri, C. La Vecchia, and P. Boffetta, “Risk factors for lung cancer worldwide,” *Eur. Respir. J.*, vol. 48, no. 3, pp. 889–902, Sep. 2016, doi: 10.1183/13993003.00359-2016.

[51] S. Tsim, C. A. O’Dowd, R. Milroy, and S. Davidson, “Staging of non-small cell lung cancer (NSCLC): A review,” *Respiratory Medicine*, vol. 104, no. 12. pp. 1767–1774, Dec. 2010.

[52] A. Jemal *et al.*, “Annual Report to the Nation on the Status of Cancer, 1975-2014, Featuring Survival,” *Journal of the National Cancer Institute*, vol. 109, no. 9. Oxford University Press, Sep. 01, 2017.

[53] “BioRender.” https://biorender.com/ (accessed Oct. 07, 2021).

[54] N. McGonigle, “Lung cancer,” *Surgery (United Kingdom)*, vol. 38, no. 5. Elsevier Ltd, pp. 249–254, May 01, 2020.

[55] A. De Luca, M. Gallo, C. Esposito, A. Morabito, and N. Normanno, “Promising role of circulating tumor cells in the management of sclc,” *Cancers*, vol. 13, no. 9. MDPI AG, p. 2029, May 01, 2021.

[56] M. Zheng, “Classification and Pathology of Lung Cancer,” *Surgical Oncology Clinics of North America*, vol. 25, no. 3. W.B. Saunders, pp. 447–468, 2016.

[57] L. H. Araujo, L. Horn, R. E. Merritt, K. Shilo, M. Xu-Welliver, and D. P. Carbone, “Cancer of the Lung,” in *Abeloff’s Clinical Oncology*, Elsevier, 2020, pp. 1108-1158.e16.

[58] J. Subramanian and R. Govindan, “Lung cancer in never smokers: A review,” *Journal of Clinical Oncology*, vol. 25, no. 5. American Society of Clinical Oncology, pp. 561–570, Feb. 10, 2007.

[59] X. Jiang, J. Wu, J. Wang, and R. Huang, “Tobacco and oral squamous cell carcinoma: A review of carcinogenic pathways,” *Tobacco Induced Diseases*, vol. 17, no. April. International Society for the Prevention of Tobacco Induced Diseases, 2019.

[60] S. H. Moolgavkar and A. G. Knudson, “Mutation and cancer: A model for human carcinogenesis,” *J. Natl. Cancer Inst.*, vol. 66, no. 6, pp. 1037–1052, Jun. 1981, doi: 10.1093/jnci/66.6.1037.

[61] N. Chatterjee and G. C. Walker, “Mechanisms of DNA damage, repair, and mutagenesis,” *Environmental and Molecular Mutagenesis*, vol. 58, no. 5. John Wiley and Sons Inc., pp. 235–263, Jun. 01, 2017.

[62] S. Chakarov, R. Petkova, G. Russev, and N. Zhelev, “DNA damage and mutation. Types of DNA damage,” *Biodiscovery*, vol. 11, no. 11, p. 1, Feb. 2014, doi: 10.7750/biodiscovery.2014.11.1.

[63] J. Chen, B. F. Miller, and A. V. Furano, “Repair of naturally occurring mismatches can induce mutations in flanking DNA,” *Elife*, vol. 2014, no. 3, Apr. 2014, doi: 10.7554/eLife.02001.001.

[64] W. A. Cooper, D. C. L. Lam, S. A. O’Toole, and J. D. Minna, “Molecular biology of lung cancer,” *Journal of Thoracic Disease*, vol. 5, no. SUPPL.5. Pioneer Bioscience Publishing, 2013.

[65] J. D. Minna, J. A. Roth, and A. F. Gazdar, “Focus on lung cancer,” 2002.

[66] N. Karachaliou *et al.*, “KRAS mutations in lung cancer,” *Clinical Lung Cancer*, vol. 14, no. 3. Elsevier, pp. 205–214, May 01, 2013.

[67] I. Ferrer, J. Zugazagoitia, S. Herbertz, W. John, L. Paz-Ares, and G. Schmid-Bindert, “KRAS-Mutant non-small cell lung cancer: From biology to therapy,” *Lung Cancer*, vol. 124. Elsevier Ireland Ltd, pp. 53–64, Oct. 01, 2018.

[68] M. Román *et al.*, “KRAS oncogene in non-small cell lung cancer: Clinical perspectives on the treatment of an old target,” *Molecular Cancer*, vol. 17, no. 1. BioMed Central Ltd., pp. 1–14, Feb. 19, 2018.

[69] Y. Lin, X. Wang, and H. Jin, “EGFR-TKI resistance in NSCLC patients: mechanisms and strategies.,” *Am. J. Cancer Res.*, vol. 4, no. 5, pp. 411–35, 2014, Accessed: Jun. 20, 2021. [Online]. Available: http://www.ncbi.nlm.nih.gov/pubmed/25232485.

[70] A. Mogi and H. Kuwano, “TP53 mutations in nonsmall cell lung cancer,” *Journal of Biomedicine and Biotechnology*, vol. 2011. 2011.

[71] F. Facchinetti *et al.*, “LKB1/STK11 mutations in non-small cell lung cancer patients: Descriptive analysis and prognostic value,” *Lung Cancer*, vol. 112, pp. 62–68, Oct. 2017, doi: 10.1016/j.lungcan.2017.08.002.

[72] Y. Jin *et al.*, “B-Myb is up-regulated and promotes cell growth and motility in non-small cell lung cancer,” *Int. J. Mol. Sci.*, vol. 18, no. 6, p. 860, Jun. 2017, doi: 10.3390/ijms18060860.

[73] U. R. Rapp *et al.*, “Myc is a metastasis gene for non-small-cell lung cancer,” *PLoS One*, vol. 4, no. 6, p. e6029, Jun. 2009, doi: 10.1371/journal.pone.0006029.

[74] M. Soda *et al.*, “Identification of the transforming EML4-ALK fusion gene in non-small-cell lung cancer,” *Nature*, vol. 448, no. 7153, pp. 561–566, Aug. 2007, doi: 10.1038/nature05945.

[75] M. Scheffler *et al.*, “PIK3CA mutations in non-small cell lung cancer (NSCLC): Genetic heterogeneity, prognostic impact and incidence of prior malignancies,” *Oncotarget*, vol. 6, no. 2, pp. 1315–1326, 2015, doi: 10.18632/oncotarget.2834.

[76] C. J. Cheng and F. J. Slack, “The duality of oncomiR addiction in the maintenance and treatment of cancer,” *Cancer Journal (United States)*, vol. 18, no. 3. NIH Public Access, pp. 232–237, May 2012.

[77] H. Petrek and A. M. Yu, “MicroRNAs in non-small cell lung cancer: Gene regulation, impact on cancer cellular processes, and therapeutic potential,” *Pharmacology research & perspectives*, vol. 7, no. 6. NLM (Medline), p. e00528, Dec. 01, 2019.

[78] N. Duma, R. Santana-Davila, and J. R. Molina, “Non–Small Cell Lung Cancer:

Epidemiology, Screening, Diagnosis, and Treatment," *Mayo Clinic Proceedings*, vol. 94, no. 8. Elsevier Ltd, pp. 1623–1640, Aug. 01, 2019.

[79] V. L. Athey, R. J. Suckling, A. M. Tod, S. J. Walters, and T. K. Rogers, "Early diagnosis of lung cancer: Evaluation of a community-based social marketing intervention," *Thorax*, vol. 67, no. 5, pp. 412–417, 2012, doi: 10.1136/thoraxjnl-2011-200714.

[80] L. G. Collins, C. Haines, R. Perkel, and R. E. Enck, "Lung Cancer: Diagnosis and Management," Jan. 2007. Accessed: Jun. 21, 2021. [Online]. Available: http://familydoctor.org/161.xml.

[81] M. P. Rivera, F. Detterbeck, and A. C. Mehta, "Diagnosis of lung cancer: The guidelines," *Chest*, vol. 123, no. 1 SUPPL. American College of Chest Physicians, pp. 129S-136S, Jan. 01, 2003.

[82] L. Kalinke, R. Thakrar, and S. M. Janes, "The promises and challenges of early non-small cell lung cancer detection: patient perceptions, low-dose CT screening, bronchoscopy and biomarkers," *Molecular Oncology*. John Wiley and Sons Ltd, 2020.

[83] A. McLean, D. Barnes, and L. Troy, "Diagnosing Lung Cancer: The Complexities of Obtaining a Tissue Diagnosis in the Era of Minimally Invasive and Personalised Medicine," *J. Clin. Med.*, vol. 7, no. 7, p. 163, Jun. 2018, doi: 10.3390/jcm7070163.

[84] S. Bal, "Non small cell lung cancer (NSCLC): current status and future prospects," 2004. Accessed: Jun. 22, 2021. [Online]. Available: https://www.researchgate.net/publication/8174517.

[85] P. F. Pinsky, M. Freedman, P. Kvale, M. Oken, N. Caporaso, and J. Gohagan, "Abnormalities on chest radiograph reported in subjects in a cancer screening trial," *Chest*, vol. 130, no. 3, pp. 688–693, 2006, doi: 10.1378/chest.130.3.688.

[86] S. H. Bradley *et al.*, "Sensitivity of chest X-ray for detecting lung cancer in people presenting with symptoms: A systematic review," *Br. J. Gen. Pract.*, vol. 69, no. 689, pp. E827–E835, 2019, doi: 10.3399/bjgp19X706853.

[87] A. del Ciello, P. Franchi, A. Contegiacomo, G. Cicchetti, L. Bonomo, and A. R. Larici, "Missed lung cancer: When, where, and why?," *Diagnostic and Interventional Radiology*, vol. 23, no. 2. AVES Ibrahim Kara, pp. 118–126, Mar. 01, 2017.

[88] J. A. Verschakelen and W. De Wever, *Computed Tomography of the Lung*. Berlin, Heidelberg: Springer Berlin Heidelberg, 2018.

[89] N. Hollings and P. Shaw, “Diagnostic imaging of lung cancer,” *Eur. Respir. J.*, vol. 19, no. 4, pp. 722–742, Apr. 2002, doi: 10.1183/09031936.02.00280002.

[90] D. J. Brenner, E. J. Hall, and D. Phil, “Computed Tomography-An Increasing Source of Radiation Exposure,” 2007. Accessed: Jun. 22, 2021. [Online]. Available: www.nejm.org.

[91] C. Greco, K. Rosenzweig, G. L. Cascini, and O. Tamburrini, “Current status of PET/CT for tumour volume definition in radiotherapy treatment planning for non-small cell lung cancer (NSCLC),” *Lung Cancer*, vol. 57, no. 2. Elsevier, pp. 125–134, Aug. 01, 2007.

[92] A. S. Ammanagi, V. D. Dombale, A. T. Miskin, G. L. Dandagi, and S. S. Sangolli, “Sputum cytology in suspected cases of carcinoma of lung (Sputum cytology a poor man’s bronchoscopy!),” *Lung India*, vol. 29, no. 1, pp. 19–23, Jan. 2012, doi: 10.4103/0970-2113.92356.

[93] T. L. Bauer and D. B. Berkheim, “Bronchoscopy Diagnostic and Therapeutic for Non-Small Cell Lung Cancer,” 2016, doi: 10.1016/j.soc.2016.02.009.

[94] S. Ozkaya, Tuna, A. Dirican, S. Findik, Atici, and Erkan, “Diagnostic efficacy of computed tomography-guided transthoracic needle aspiration and biopsy in patients with pulmonary disease,” *Onco. Targets. Ther.*, vol. 6, p. 1553, Nov. 2013, doi: 10.2147/ott.s45013.

[95] A. Hasanovic, N. Rekhtman, C. S. Sigel, and A. L. Moreira, “Advances in Fine Needle Aspiration Cytology for the Diagnosis of Pulmonary Carcinoma,” *Patholog. Res. Int.*, vol. 2011, pp. 1–7, Jun. 2011, doi: 10.4061/2011/897292.

[96] H. Hoffmann, “Invasive staging of lung cancer by mediastinoscopy and video-assisted thoracoscopy,” in *Lung Cancer*, Dec. 2001, vol. 34, no. SUPPL. 3, pp. 3–5.

[97] Y. W. Chiu *et al.*, “Costs of biopsy and complications in patients with lung cancer,” *Clin. Outcomes Res.*, vol. 13, pp. 191–200, 2021, doi: 10.2147/CEOR.S295494.

[98] U. Topal and B. Ediz, “Transthoracic needle biopsy: Factors effecting risk of pneumothorax,” *Eur. J. Radiol.*, vol. 48, no. 3, pp. 263–267, Dec. 2003, doi:

10.1016/S0720-048X(03)00058-5.

[99] S. B. Knight, P. A. Crosbie, H. Balata, J. Chudziak, T. Hussell, and C. Dive, “Progress and prospects of early detection in lung cancer,” *Open Biol.*, vol. 7, no. 9, 2017, doi: 10.1098/rsob.170070.

[100] C. Rolfo *et al.*, “Liquid Biopsy for Advanced Non-Small Cell Lung Cancer (NSCLC): A Statement Paper from the IASLC,” *Journal of Thoracic Oncology*, vol. 13, no. 9. Elsevier Inc, pp. 1248–1268, Sep. 01, 2018.

[101] A. G. Dent, T. G. Sutedja, and P. V. Zimmerman, “Exhaled breath analysis for lung cancer,” *Journal of Thoracic Disease*, vol. 5, no. SUPPL.5. Pioneer Bioscience Publishing, p. S540, 2013.

[102] P. Villalobos and I. I. Wistuba, “Lung Cancer Biomarkers,” *Hematol. Oncol. Clin. North Am.*, vol. 31, no. 1, p. 13, Feb. 2017, doi: 10.1016/J.HOC.2016.08.006.

[103] J. Liao, J. Shen, Q. Leng, M. Qin, M. Zhan, and F. Jiang, “MicroRNA-based biomarkers for diagnosis of non-small cell lung cancer (NSCLC),” *Thorac. Cancer*, vol. 11, no. 3, pp. 762–768, Mar. 2020, doi: 10.1111/1759-7714.13337.

[104] Y. Han and H. Li, “miRNAs as biomarkers and for the early detection of non-small cell lung cancer (NSCLC),” *J. Thorac. Dis.*, vol. 10, no. 5, p. 3119, May 2018, doi: 10.21037/JTD.2018.05.32.

[105] J. H. Lee, J. A. Kim, M. H. Kwon, J. Y. Kang, and W. J. Rhee, “In situ single step detection of exosome microRNA using molecular beacon,” *Biomaterials*, vol. 54, pp. 116–125, Jun. 2015, doi: 10.1016/J.BIOMATERIALS.2015.03.014.

[106] Y. Q *et al.*, “Novel molecular beacons to monitor microRNAs in non-small-cell lung cancer,” *Mol. Cell. Probes*, vol. 26, no. 5, pp. 182–187, Oct. 2012, doi: 10.1016/J.MCP.2012.07.001.

[107] J. S. Mattick and I. V. Makunin, “Non-coding RNA,” *Hum. Mol. Genet.*, vol. 15, no. suppl_1, pp. R17–R29, Apr. 2006, doi: 10.1093/HMG/DDL046.

[108] M. C. de Sousa, M. Gjorgjieva, D. Dolicka, C. Sobolewski, and M. Foti, “Deciphering miRNAs’ action through miRNA editing,” *Int. J. Mol. Sci.*, vol. 20, no. 24, Dec. 2019, doi: 10.3390/IJMS20246249.

[109] M. H. Sohel, "Extracellular/Circulating MicroRNAs: Release Mechanisms, Functions and Challenges," *Achiev. Life Sci.*, vol. 10, no. 2, pp. 175–186, Dec. 2016, doi: 10.1016/J.ALS.2016.11.007.

[110] A. Vishnoi and S. Rani, "MiRNA biogenesis and regulation of diseases: An overview," *Methods Mol. Biol.*, vol. 1509, pp. 1–10, 2017, doi: 10.1007/978-1-4939-6524-3_1.

[111] S. M. Hammond, "An overview of microRNAs," *Adv. Drug Deliv. Rev.*, vol. 87, pp. 3–14, Jun. 2015, doi: 10.1016/J.ADDR.2015.05.001.

[112] D. P. Bartel, "Metazoan MicroRNAs," *Cell*, vol. 173, no. 1, p. 20, Mar. 2018, doi: 10.1016/J.CELL.2018.03.006.

[113] N. Ludwig *et al.*, "Distribution of miRNA expression across human tissues," *Nucleic Acids Res.*, vol. 44, no. 8, pp. 3865–3877, May 2016, doi: 10.1093/NAR/GKW116.

[114] Z. Zhang *et al.*, "microRNA arm-imbalance in part from complementary targets mediated decay promotes gastric cancer progression," *Nat. Commun. 2019 101*, vol. 10, no. 1, pp. 1–16, Sep. 2019, doi: 10.1038/s41467-019-12292-5.

[115] Y. Han *et al.*, "Dysregulation of miRNA-21 and their potential as biomarkers for the diagnosis of cervical cancer," *Int. J. Clin. Exp. Pathol.*, vol. 8, no. 6, p. 7131, 2015, Accessed: Oct. 11, 2021. [Online]. Available: /pmc/articles/PMC4525940/.

[116] A. Eulalio, E. Huntzinger, and E. Izaurralde, "Getting to the Root of miRNA-Mediated Gene Silencing," *Cell*, vol. 132, no. 1, pp. 9–14, Jan. 2008, doi: 10.1016/J.CELL.2007.12.024.

[117] Y. Peng and C. M. Croce, "The role of MicroRNAs in human cancer," *Signal Transduct. Target. Ther. 2016 11*, vol. 1, no. 1, pp. 1–9, Jan. 2016, doi: 10.1038/sigtrans.2015.4.

[118] K. Saliminejad, H. R. Khorram Khorshid, S. Soleymani Fard, and S. H. Ghaffari, "An overview of microRNAs: Biology, functions, therapeutics, and analysis methods," *J. Cell. Physiol.*, vol. 234, no. 5, pp. 5451–5465, May 2019, doi: 10.1002/JCP.27486.

[119] K.-L. Wu, Y.-M. Tsai, C.-T. Lien, P.-L. Kuo, and J.-Y. Hung, "The Roles of MicroRNA in Lung Cancer," *Int. J. Mol. Sci.*, vol. 20, no. 7, Apr. 2019, doi: 10.3390/IJMS20071611.

[120] Z. B, P. X, C. GP, and A. TA, "microRNAs as oncogenes and tumor suppressors," *Dev. Biol.*, vol. 302, no. 1, pp. 1–12, Feb. 2007, doi: 10.1016/J.YDBIO.2006.08.028.

[121] X. Zhu *et al.*, “Frontiers of MicroRNA Signature in Non-small Cell Lung Cancer,” *Front. Cell Dev. Biol.*, vol. 0, p. 771, Apr. 2021, doi: 10.3389/FCELL.2021.643942.

[122] Y. Wang *et al.*, “Role of deregulated microRNAs in non-small cell lung cancer progression using fresh-frozen and formalin-fixed, paraffin-embedded samples,” *Oncol. Lett.*, vol. 11, no. 1, pp. 801–808, Jan. 2016, doi: 10.3892/OL.2015.3976.

[123] P. D *et al.*, “miRNA profiling in serum and tissue samples to assess noninvasive biomarkers for NSCLC clinical outcome,” *Tumour Biol.*, vol. 37, no. 4, pp. 5503–5513, Apr. 2016, doi: 10.1007/S13277-015-4391-1.

[124] S. Hu, Y. Yuan, Z. Song, D. Yan, and X. Kong, “Expression profiles of microRNAs in drug-resistant non-small cell lung cancer cell lines using microRNA sequencing,” *Cell. Physiol. Biochem.*, vol. 51, no. 6, pp. 2509–2522, Jan. 2019, doi: 10.1159/000495921.

[125] J. Hou, F. Meng, L. W. C. Chan, W. C. S. Cho, and S. C. C. Wong, “Circulating plasma MicroRNAs as diagnostic markers for NSCLC,” *Frontiers in Genetics*, vol. 7, no. NOV. Frontiers Media S.A., Nov. 03, 2016.

[126] H. AR *et al.*, “Serum MiRNA as Predictive and Prognosis Biomarker in Advanced Stage Non-small Cell Lung Cancer in Indonesia,” *Zhongguo Fei Ai Za Zhi*, vol. 23, no. 5, pp. 321–332, May 2020, doi: 10.3779/J.ISSN.1009-3419.2020.104.02.

[127] X. Y *et al.*, “Altered miRNA expression in sputum for diagnosis of non-small cell lung cancer,” *Lung Cancer*, vol. 67, no. 2, pp. 170–176, Feb. 2010, doi: 10.1016/J.LUNGCAN.2009.04.004.

[128] M. Mosallaei, N. Ehtesham, S. Rahimirad, M. Saghi, N. Vatandoost, and S. Khosravi, “PBMCs: a new source of diagnostic and prognostic biomarkers,” *https://doi.org/10.1080/13813455.2020.1752257*, 2020, doi: 10.1080/13813455.2020.1752257.

[129] C. C. Chang, C. C. Lin, W. L. Hsieh, H. W. Lai, C. H. Tsai, and Y. W. Cheng, “MicroRNA expression profiling in PBMCs: A potential diagnostic biomarker of chronic hepatitis C,” *Dis. Markers*, vol. 2014, 2014, doi: 10.1155/2014/367157.

[130] C. Wang *et al.*, “Comparative miRNA Expression Profiles in Individuals with Latent and Active Tuberculosis,” *PLoS One*, vol. 6, no. 10, p. e25832, Oct. 2011, doi: 10.1371/JOURNAL.PONE.0025832.

[131] X. Zhu *et al.*, “Identification of PBMC-expressed miRNAs for rheumatoid arthritis,” *https://doi.org/10.1080/15592294.2019.1676613*, vol. 15, no. 4, pp. 386–397, Apr. 2019, doi: 10.1080/15592294.2019.1676613.

[132] M. J, L. Y, Z. M, M. DL, S. SA, and J. F, “Differential miRNA expressions in peripheral blood mononuclear cells for diagnosis of lung cancer,” *Lab. Invest.*, vol. 95, no. 10, pp. 1197–1206, Oct. 2015, doi: 10.1038/LABINVEST.2015.88.

[133] M. Florczuk, A. Szpechcinski, and J. Chorostowska-Wynimko, “miRNAs as Biomarkers and Therapeutic Targets in Non-Small Cell Lung Cancer: Current Perspectives,” *Target. Oncol.*, vol. 12, no. 2, pp. 179–200, Apr. 2017, doi: 10.1007/S11523-017-0478-5.

[134] S. Gallach *et al.*, “MicroRNA profiling associated with non-small cell lung cancer: next generation sequencing detection, experimental validation, and prognostic value,” *Oncotarget*, vol. 8, no. 34, p. 56143, 2017, doi: 10.18632/ONCOTARGET.18603.

[135] C. Bica-Pop, R. Cojocneanu-Petric, L. Magdo, L. Raduly, D. Gulei, and I. Berindan-Neagoe, “Overview upon miR-21 in lung cancer: focus on NSCLC,” *Cell. Mol. Life Sci.*, vol. 75, no. 19, pp. 3539–3551, Oct. 2018, doi: 10.1007/S00018-018-2877-X.

[136] J. guang Zhang, J. jun Wang, F. Zhao, Q. Liu, K. Jiang, and G. hai Yang, “MicroRNA-21 (miR-21) represses tumor suppressor PTEN and promotes growth and invasion in non-small cell lung cancer (NSCLC),” *Clin. Chim. Acta*, vol. 411, no. 11–12, pp. 846–852, Jun. 2010, doi: 10.1016/J.CCA.2010.02.074.

[137] Z.-L. Liu, H. Wang, J. Liu, and Z.-X. Wang, “MicroRNA-21 (miR-21) expression promotes growth, metastasis, and chemo- or radioresistance in non-small cell lung cancer cells by targeting PTEN,” *Mol. Cell. Biochem. 2012 3721*, vol. 372, no. 1, pp. 35–45, Sep. 2012, doi: 10.1007/S11010-012-1443-3.

[138] H. Shen *et al.*, “Alteration in Mir-21/PTEN Expression Modulates Gefitinib Resistance in Non-Small Cell Lung Cancer,” *PLoS One*, vol. 9, no. 7, p. e103305, Jul. 2014, doi: 10.1371/JOURNAL.PONE.0103305.

[139] B. Zhou, D. Wang, G. Sun, F. Mei, Y. Cui, and H. Xu, “Effect of miR-21 on Apoptosis in Lung Cancer Cell Through Inhibiting the PI3K/ Akt/NF-κB Signaling Pathway in Vitro and in Vivo,” *Cell. Physiol. Biochem.*, vol. 46, no. 3, pp. 999–1008, Apr. 2018, doi: 10.1159/000488831.

[140] W. Zheng *et al.*, “MicroRNA-21: A promising biomarker for the prognosis and diagnosis of non-small cell lung cancer,” *Oncol. Lett.*, vol. 16, no. 3, p. 2777, Sep. 2018, doi: 10.3892/OL.2018.8972.

[141] L. Lei, Y. Huang, and W. Gong, “Inhibition of miR-92b suppresses nonsmall cell lung cancer cells growth and motility by targeting RECK,” *Mol. Cell. Biochem. 2013 3871*, vol. 387, no. 1, pp. 171–176, Oct. 2013, doi: 10.1007/S11010-013-1882-5.

[142] L. X, T. XD, L. Y, Z. T, and C. L, “Regulation of Twist in the metastasis of non-small cell lung cancer by miR-92b.,” *Eur. Rev. Med. Pharmacol. Sci.*, vol. 20, no. 19, pp. 4003–4010, Oct. 2016, Accessed: Sep. 06, 2021. [Online]. Available: https://europepmc.org/article/med/27775799.

[143] J.-H. Guo *et al.*, “MicroRNA-92b acts as an oncogene by targeting PTEN/AKT in NSCLC,” *Cell Biochem. Funct.*, vol. 38, no. 8, pp. 1100–1110, Dec. 2020, doi: 10.1002/CBF.3568.

[144] L. Y, L. L, G. Y, L. X, M. Q, and G. Q, “MiR-92b regulates the cell growth, cisplatin chemosensitivity of A549 non small cell lung cancer cell line and target PTEN,” *Biochem. Biophys. Res. Commun.*, vol. 440, no. 4, pp. 604–610, Nov. 2013, doi: 10.1016/J.BBRC.2013.09.111.

[145] H. Li *et al.*, “MiR-150 promotes cellular metastasis in non-small cell lung cancer by targeting FOXO4,” *Sci. Reports 2016 61*, vol. 6, no. 1, pp. 1–11, Dec. 2016, doi: 10.1038/srep39001.

[146] K. Jiang, M. Shen, Y. Chen, and W. Xu, “miR-150 promotes the proliferation and migration of non-small cell lung cancer cells by regulating the SIRT2/JMJD2A signaling pathway,” *Oncol. Rep.*, vol. 40, no. 2, pp. 943–951, Aug. 2018, doi: 10.3892/OR.2018.6487.

[147] D.-T. Wang *et al.*, “miR-150, p53 protein and relevant miRNAs consist of a regulatory network in NSCLC tumorigenesis,” *Oncol. Rep.*, vol. 30, no. 1, pp. 492–498, Jul. 2013, doi: 10.3892/OR.2013.2453.

[148] N. Zhang, X. Wei, and L. Xu, “miR-150 promotes the proliferation of lung cancer cells by targeting P53,” *FEBS Lett.*, vol. 587, no. 15, pp. 2346–2351, Aug. 2013, doi: 10.1016/J.FEBSLET.2013.05.059.

[149] F. Q. Dai, C. R. Li, X. Q. Fan, L. Tan, R. T. Wang, and H. Jin, “miR-150-5p Inhibits Non-Small-Cell Lung Cancer Metastasis and Recurrence by Targeting HMGA2 and β-Catenin Signaling,” *Mol. Ther. - Nucleic Acids*, vol. 16, pp. 675–685, Jun. 2019, doi: 10.1016/J.OMTN.2019.04.017.

[150] Y. QW, S. XF, Y. GT, L. XB, W. MS, and Z. J, “Increased expression of microRNA-150 is associated with poor prognosis in non-small cell lung cancer.,” *Int. J. Clin. Exp. Pathol.*, vol. 8, no. 1, pp. 842–846, Jan. 2015, Accessed: Jul. 25, 2021. [Online]. Available: https://europepmc.org/articles/PMC4348842.

[151] Z. L *et al.*, “Serum MicroRNA-150 Predicts Prognosis for Early-Stage Non-Small Cell Lung Cancer and Promotes Tumor Cell Proliferation by Targeting Tumor Suppressor Gene SRCIN1,” *Clin. Pharmacol. Ther.*, vol. 103, no. 6, pp. 1061–1073, Jun. 2018, doi: 10.1002/CPT.870.

[152] X. ZENG, S. ZHANG, J. ZHENG, H. YUAN, and Y. WANG, “Altered miR-143 and miR-150 expressions in peripheral blood mononuclear cells for diagnosis of non-small cell lung cancer,” *Chin. Med. J. (Engl).*, pp. 4510–4516, 2013, Accessed: Jul. 25, 2021. [Online]. Available: http://dx.doi.org/.

[153] X. Xue *et al.*, “MiR-21 and MiR-155 promote non-small cell lung cancer progression by downregulating SOCS1, SOCS6, and PTEN,” *Oncotarget*, vol. 7, no. 51, p. 84508, 2016, doi: 10.18632/ONCOTARGET.13022.

[154] L. F, S. D, W. Y, L. X, Z. J, and T. Y, “MiR-155 inhibits proliferation and invasion by directly targeting PDCD4 in non-small cell lung cancer,” *Thorac. cancer*, vol. 8, no. 6, pp. 613–619, Nov. 2017, doi: 10.1111/1759-7714.12492.

[155] H. L, C. J, Z. Y, and W. C, “Critical role of miR-155/FoxO1/ROS axis in the regulation of non-small cell lung carcinomas,” *Tumour Biol.*, vol. 37, no. 4, pp. 5185–5192, Apr. 2016, doi: 10.1007/S13277-015-4335-9.

[156] X. Lv, L. Yao, J. Zhang, P. Han, and C. Li, “Inhibition of microRNA-155 sensitizes lung cancer cells to irradiation via suppression of HK2-modulated glucose metabolism,” *Mol. Med. Rep.*, vol. 14, no. 2, pp. 1332–1338, Aug. 2016, doi: 10.3892/MMR.2016.5394.

[157] Z. HZ *et al.*, “Detection of miR-155-5p and imaging lung cancer for early diagnosis: in vitro and in vivo study,” *J. Cancer Res. Clin. Oncol.*, vol. 146, no. 8, pp. 1941–1951, Aug. 2020, doi: 10.1007/S00432-020-03246-2.

[158] C. Shao, F. Yang, Z. Qin, X. Jing, Y. Shu, and H. Shen, “The value of miR-155 as a biomarker for the diagnosis and prognosis of lung cancer: a systematic review with meta-analysis,” *BMC Cancer 2019 191*, vol. 19, no. 1, pp. 1–10, Nov. 2019, doi: 10.1186/S12885-019-6297-6.

[159] T. Donnem *et al.*, “Prognostic Impact of MiR-155 in Non-Small Cell Lung Cancer Evaluated by in Situ Hybridization,” *J. Transl. Med. 2011 91*, vol. 9, no. 1, pp. 1–9, Jan. 2011, doi: 10.1186/1479-5876-9-6.

[160] G. F, C. J, W. H, and Z. G, “Potential diagnostic value of miR-155 in serum from lung adenocarcinoma patients,” *Oncol. Rep.*, vol. 31, no. 1, pp. 351–357, Jan. 2014, doi: 10.3892/OR.2013.2830.

[161] S. AM, L. YA, and A. AI, “MicroRNA-181a - a tale of discrepancies,” *Expert Rev. Mol. Med.*, vol. 14, Jan. 2012, doi: 10.1017/S1462399411002122.

[162] W. Gao *et al.*, “Deregulated expression of miR-21, miR-143 and miR-181a in non small cell lung cancer is related to clinicopathologic characteristics or patient prognosis,” *Biomed. Pharmacother.*, vol. 64, no. 6, pp. 399–408, Jul. 2010, doi: 10.1016/J.BIOPHA.2010.01.018.

[163] C. Braicu *et al.*, “miR-181a/b therapy in lung cancer: reality or myth?,” *Mol. Oncol.*, vol. 13, no. 1, pp. 9–25, Jan. 2019, doi: 10.1002/1878-0261.12420.

[164] M. Z *et al.*, “MiR-181a-5p inhibits cell proliferation and migration by targeting Kras in non-small cell lung cancer A549 cells,” *Acta Biochim. Biophys. Sin. (Shanghai).*, vol. 47, no. 8, pp. 630–638, Aug. 2015, doi: 10.1093/ABBS/GMV054.

[165] S. Q, Z. Z, Y. N, C. Q, Z. X, and F. M, “MiR-181a inhibits non-small cell lung cancer cell proliferation by targeting CDK1,” *Cancer Biomark.*, vol. 20, no. 4, pp. 539–546, 2017, doi: 10.3233/CBM-170350.

[166] W. X. Xue, M. Y. Zhang, Rui Li, X. Liu, Y. H. Yin, and Y. Q. Qu, “Serum miR-1228-3p and miR-181a-5p as Noninvasive Biomarkers for Non-Small Cell Lung Cancer Diagnosis and Prognosis,” *Biomed Res. Int.*, vol. 2020, 2020, doi: 10.1155/2020/9601876.

[167] T. Powrózek, P. Krawczyk, D. M. Kowalski, K. Winiarczyk, M. Olszyna-Serementa, and J. Milanowski, “Plasma circulating microRNA-944 and microRNA-3662 as potential histologic type-specific early lung cancer biomarkers,” *Transl. Res.*, vol. 166, no. 4, pp.

315–323, Oct. 2015, doi: 10.1016/J.TRSL.2015.05.009.

[168] T. Powrózek *et al.*, "The diagnostic role of plasma circulating precursors of miRNA-944 and miRNA-3662 for non-small cell lung cancer detection," *Pathol. - Res. Pract.*, vol. 213, no. 11, pp. 1384–1387, Nov. 2017, doi: 10.1016/J.PRP.2017.09.011.

[169] Z. Chen *et al.*, "MiR-3662 suppresses hepatocellular carcinoma growth through inhibition of HIF-1α-mediated Warburg effect," *Cell Death Dis. 2018 95*, vol. 9, no. 5, pp. 1–14, May 2018, doi: 10.1038/s41419-018-0616-8.

[170] M. R. Green and J. Sambrook, "How to Win the Battle with RNase," *Cold Spring Harb. Protoc.*, vol. 2019, no. 2, p. pdb.top101857, Feb. 2019, doi: 10.1101/PDB.TOP101857.

[171] M. B. Kirschner, J. J. B. Edelman, S. C.-H. Kao, M. P. Vallely, N. van Zandwijk, and G. Reid, "The Impact of Hemolysis on Cell-Free microRNA Biomarkers," *Front. Genet.*, vol. 4, no. MAY, 2013, doi: 10.3389/FGENE.2013.00094.

[172] S. Pizzamiglio *et al.*, "A methodological procedure for evaluating the impact of hemolysis on circulating microRNAs," *Oncol. Lett.*, vol. 13, no. 1, pp. 315–320, Jan. 2017, doi: 10.3892/OL.2016.5452.

[173] M. MP *et al.*, "Quantitative PCR Measurement of miR-371a-3p and miR-372-p Is Influenced by Hemolysis," *Front. Genet.*, vol. 10, no. MAY, 2019, doi: 10.3389/FGENE.2019.00463.

[174] B. M. Ian, "Extraction of RNA From Cells and Tissue," *Methods Mol. Med.*, vol. 108, pp. 139–148, 2005, doi: 10.1385/1-59259-850-1:139.

[175] P. Chomczynski and N. Sacchi, "The single-step method of RNA isolation by acid guanidinium thiocyanate-phenol-chloroform extraction: Twenty-something years on," *Nat. Protoc.*, vol. 1, no. 2, pp. 581–585, Jul. 2006, doi: 10.1038/NPROT.2006.83.

[176] C. R. Merril, "Gel Electrophoresis of Proteins: A Practical Approach, Third ed. Edited by B. D. Hames," *Anal. Biochem.*, vol. 280, no. 2, p. 333, May 2000, doi: 10.1006/ABIO.2000.4496.

[177] D. O'Neil, H. Glowatz, and M. Schlumpberger, "Ribosomal RNA Depletion for Efficient Use of RNA-Seq Capacity," *Curr. Protoc. Mol. Biol.*, vol. 103, no. 1, pp. 4.19.1-4.19.8, Jul. 2013, doi: 10.1002/0471142727.MB0419S103.

[178] P. S. Aranda, D. M. LaJoie, and C. L. Jorcyk, "Bleach gel: A simple agarose gel for analyzing RNA quality," *Electrophoresis*, vol. 33, no. 2, pp. 366–369, Jan. 2012, doi: 10.1002/ELPS.201100335.

[179] B. LM, D. S, B. M, M. TR, Y. M, and H. DJ, "Poly(A) polymerase modification and reverse transcriptase PCR amplification of environmental RNA," *Appl. Environ. Microbiol.*, vol. 71, no. 3, pp. 1267–1275, Mar. 2005, doi: 10.1128/AEM.71.3.1267-1275.2005.

[180] I. E. Tzanetakis, K. E. Keller, and R. R. Martin, "The use of reverse transcriptase for efficient first- and second-strand cDNA synthesis from single- and double-stranded RNA templates," *J. Virol. Methods*, vol. 124, no. 1–2, pp. 73–77, Mar. 2005, doi: 10.1016/J.JVIROMET.2004.11.006.

[181] M. Joshi and J. D. Deshpande, "POLYMERASE CHAIN REACTION: METHODS, PRINCIPLES AND APPLICATION," *Int. J. Biomed. Res.*, vol. 2, no. 1, pp. 81–97, Feb. 2011, doi: 10.7439/IJBR.V2I1.83.

[182] M. Arya, I. S. Shergill, M. Williamson, L. Gommersall, N. Arya, and H. R. H. Patel, "Basic principles of real-time quantitative PCR," *Expert Rev. Mol. Diagn.*, vol. 5, no. 2, pp. 209–219, Mar. 2005, doi: 10.1586/14737159.5.2.209.

[183] L. KJ and S. TD, "Analysis of relative gene expression data using real-time quantitative PCR and the 2(-Delta Delta C(T)) Method," *Methods*, vol. 25, no. 4, pp. 402–408, 2001, doi: 10.1006/METH.2001.1262.

[184] B. Rizzacasa, "Comparative Ct method quantification (2-ΔCt method).," May 2019, doi: 10.17504/PROTOCOLS.IO.ZP7F5RN.

[185] M. T. Dorak, "Relative quantification," *Real-time PCR*, pp. 89–108, Jan. 2007, doi: 10.4324/9780203967317-12.

[186] E. Ragni *et al.*, "miR-103a-3p and miR-22-5p Are Reliable Reference Genes in Extracellular Vesicles From Cartilage, Adipose Tissue, and Bone Marrow Cells," *Front. Bioeng. Biotechnol.*, vol. 0, p. 51, Feb. 2021, doi: 10.3389/FBIOE.2021.632440.

[187] É. Costé and F. Rouleux-Bonnin, "The crucial choice of reference genes: identification of miR-191-5p for normalization of miRNAs expression in bone marrow mesenchymal stromal cell and HS27a/HS5 cell lines," *Sci. Reports 2020 101*, vol. 10, no. 1, pp. 1–13,

Oct. 2020, doi: 10.1038/s41598-020-74685-7.

[188] E. Sauer, I. Babion, B. Madea, and C. Courts, “An evidence based strategy for normalization of quantitative PCR data from miRNA expression analysis in forensic organ tissue identification,” *Forensic Sci. Int. Genet.*, vol. 13, pp. 217–223, 2014, doi: 10.1016/j.fsigen.2014.08.005.

[189] S. Søes *et al.*, “Hypomethylation and increased expression of the putative oncogene ELMO3 are associated with lung cancer development and metastases formation,” *Oncoscience*, vol. 1, no. 5, p. 367, 2014, doi: 10.18632/ONCOSCIENCE.42.

[190] W. Tan, K. Wang, and T. J. Drake, “Molecular beacons,” *Curr. Opin. Chem. Biol.*, vol. 8, no. 5, pp. 547–553, Oct. 2004, doi: 10.1016/J.CBPA.2004.08.010.

[191] K. Wang *et al.*, “Molecular engineering of DNA: Molecular beacons,” *Angew. Chemie - Int. Ed.*, vol. 48, no. 5, pp. 856–870, Jan. 2009, doi: 10.1002/ANIE.200800370.

[192] J. Carvalho and C. Cruz, “Forster resonance energy transfer for studying nucleic acids denaturation: A chemical and biological sciences laboratory experiment,” *Biochem. Mol. Biol. Educ.*, vol. 48, no. 4, pp. 329–336, Jul. 2020, doi: 10.1002/BMB.21353.

[193] A. Tsourkas, M. A. Behlke, S. D. Rose, and G. Bao, “Hybridization kinetics and thermodynamics of molecular beacons,” *Nucleic Acids Res.*, vol. 31, no. 4, pp. 1319–1330, Feb. 2003, doi: 10.1093/NAR/GKG212.

[194] C. Wang and C. J. Yang, “Application of Molecular Beacons in Real-Time PCR,” *Mol. Beacons*, p. 45, Jan. 2014, doi: 10.1007/978-3-642-39109-5_3.

[195] A. Miranda *et al.*, “Aptamer-based approaches to detect nucleolin in prostate cancer,” *Talanta*, vol. 226, p. 122037, May 2021, doi: 10.1016/J.TALANTA.2020.122037.

[196] N. Bidar *et al.*, “Monitoring of microRNA using molecular beacons approaches: Recent advances,” *TrAC Trends Anal. Chem.*, vol. 131, p. 116021, Oct. 2020, doi: 10.1016/J.TRAC.2020.116021.

[197] B. MB, B. G, and S. CD, “The use of molecular beacons to detect and quantify microRNA,” *Methods Mol. Biol.*, vol. 1039, pp. 279–287, 2013, doi: 10.1007/978-1-62703-535-4_22.

[198] R. M. Clegg, “Chapter 1 Förster resonance energy transfer-FRET what is it, why do it,

and how it's done," *Lab. Tech. Biochem. Mol. Biol.*, vol. 33, no. C, pp. 1–57, 2009, doi: 10.1016/S0075-7535(08)00001-6.

[199] G. A. Jones and D. S. Bradshaw, "Resonance Energy Transfer: From Fundamental Theory to Recent Applications," *Front. Phys.*, vol. 0, no. JULY, p. 100, Jul. 2019, doi: 10.3389/FPHY.2019.00100.

[200] R. D, Z. J, B. L, G. A, B. A, and M. JL, "A FRET-based screening assay for nucleic acid ligands," *Methods*, vol. 57, no. 1, pp. 122–128, May 2012, doi: 10.1016/J.YMETH.2012.03.020.

[201] G. A, L. L, and M. JL, "Thermal melting studies of ligand DNA interactions," *Methods Mol. Biol.*, vol. 613, pp. 25–35, 2010, doi: 10.1007/978-1-60327-418-0_2.

[202] A. Margineanu *et al.*, "Screening for protein-protein interactions using Förster resonance energy transfer (FRET) and fluorescence lifetime imaging microscopy (FLIM)," *Sci. Reports 2016 61*, vol. 6, no. 1, pp. 1–17, Jun. 2016, doi: 10.1038/srep28186.

[203] D. Dodd and R. Hudson, "Intrinsically Fluorescent Base-Discriminating Nucleoside Analogs," *Mini. Rev. Org. Chem.*, vol. 6, no. 4, pp. 378–391, Sep. 2009, doi: 10.2174/157019309789371659.

[204] A. Kaur, P. Kaur, and S. Ahuja, "Förster resonance energy transfer (FRET) and applications thereof," *Anal. Methods*, vol. 12, no. 46, pp. 5532–5550, Dec. 2020, doi: 10.1039/D0AY01961E.

[205] B. Ranjbar and P. Gill, "Circular Dichroism Techniques: Biomolecular and Nanostructural Analyses- A Review," *Chem. Biol. Drug Des.*, vol. 74, no. 2, pp. 101–120, Aug. 2009, doi: 10.1111/J.1747-0285.2009.00847.X.

[206] A. J. Miles, R. W. Janes, and B. A. Wallace, "Tools and methods for circular dichroism spectroscopy of proteins: a tutorial review," *Chem. Soc. Rev.*, 2021, doi: 10.1039/D0CS00558D.

[207] L. CH *et al.*, "Applications of circular dichroism (CD) for structural analysis of proteins: qualification of near- and far-UV CD for protein higher order structural analysis," *J. Pharm. Sci.*, vol. 100, no. 11, pp. 4642–4654, 2011, doi: 10.1002/JPS.22695.

[208] J. Carvalho, J. A. Queiroz, and C. Cruz, "Circular dichroism of G-Quadruplex: A laboratory experiment for the study of topology and ligand binding," *J. Chem. Educ.*, vol. 94, no. 10, pp. 1547–1551, Oct. 2017, doi: 10.1021/ACS.JCHEMED.7B00160.

[209] N. Farahani, M. Behmanesh, and B. Ranjbar, "Evaluation of Rationally Designed Label-free Stem-loop DNA Probe Opening in the Presence of miR-21 by Circular Dichroism and Fluorescence Techniques," *Sci. Reports 2020 101*, vol. 10, no. 1, pp. 1–11, Mar. 2020, doi: 10.1038/s41598-020-60157-5.

[210] G. R. Bishop and J. B. Chaires, "Characterization of DNA Structures by Circular Dichroism," *Curr. Protoc. Nucleic Acid Chem.*, pp. 7.11.1-7.11.8, Dec. 2002, doi: 10.1002/0471142700.NC0711S11.

[211] J. Kypr, I. Kejnovská, D. Renčiuk, and M. Vorlíčková, "Circular dichroism and conformational polymorphism of DNA," *Nucleic Acids Res.*, vol. 37, no. 6, pp. 1713–1725, Apr. 2009, doi: 10.1093/NAR/GKP026.

[212] V. Mlynárik, "Introduction to nuclear magnetic resonance," *Anal. Biochem.*, vol. 529, pp. 4–9, Jul. 2017, doi: 10.1016/J.AB.2016.05.006.

[213] Y. Parlak and N. Guzeler, "Nuclear magnetic resonance spectroscopy applications in foods," *Curr. Res. Nutr. Food Sci.*, vol. 4, no. SpecialIssue2, pp. 161–168, Oct. 2016, doi: 10.12944/CRNFSJ.4.SPECIAL-ISSUE-OCTOBER.22.

[214] K. Zia, T. Siddiqui, S. Ali, I. Farooq, M. S. Zafar, and Z. Khurshid, "Nuclear Magnetic Resonance Spectroscopy for Medical and Dental Applications: A Comprehensive Review," *Eur. J. Dent.*, vol. 13, no. 1, p. 124, 2019, doi: 10.1055/S-0039-1688654.

[215] L. Žídek, R. Štefl, and V. Sklenář, "NMR methodology for the study of nucleic acids," *Curr. Opin. Struct. Biol.*, vol. 11, no. 3, pp. 275–281, Jun. 2001, doi: 10.1016/S0959-440X(00)00218-9.

[216] V. A. Bloomfield, D. M. Crothers, and I. Tinoco, "Nucleic acids : structures, properties, and functions," p. 794, 2000.

[217] S. Campagne, V. Gervais, and A. Milon, "Nuclear magnetic resonance analysis of protein–DNA interactions," *J. R. Soc. Interface*, vol. 8, no. 61, pp. 1065–1078, Aug. 2011, doi: 10.1098/RSIF.2010.0543.

[218] T. Q. N. Nguyen, K. W. Lim, and A. T. Phan, "A Dual-Specific Targeting Approach Based on the Simultaneous Recognition of Duplex and Quadruplex Motifs," *Sci. Reports 2017 71*, vol. 7, no. 1, pp. 1–7, Sep. 2017, doi: 10.1038/s41598-017-10583-9.

[219] S. Ikuta, R. Chattopadhyaya, H. Ito, R. E. Dickerson, and D. R. Kearns, "NMR study of a synthetic DNA hairpin," *Biochemistry*, vol. 25, no. 17, pp. 4840–4849, 2002, doi: 10.1021/BI00365A018.

[220] J. R. Lakowicz, "Principles of fluorescence spectroscopy," *Princ. Fluoresc. Spectrosc.*, pp. 1–954, 2006, doi: 10.1007/978-0-387-46312-4.

[221] A. Bose, I. Thomas, and E. Abraham, "International Journal of Advances in Pharmaceutical Analysis Fluorescence spectroscopy and its applications: A Review QR Code *Correspondence Info," *Int. J. Adv. Pharm. Anal.*, 2018, doi: 10.7439/ijapa.

[222] A. Zepeda, C. Arias, F. Flores-Jasso, and L. Vaca, "RNA Imaging: Tracking in Real-Time RNA Transport in Neurons Using Molecular Beacons and Confocal Microscopy CHAPTER OUTLINE," *BS:MCB*, vol. 113, pp. 361–389, 2013, doi: 10.1016/B978-0-12-407239-8.00017-3.

[223] † Andrew Tsourkas, ‡ Mark A. Behlke, † and Yangqing Xu, and † Gang Bao*, "Spectroscopic Features of Dual Fluorescence/Luminescence Resonance Energy-Transfer Molecular Beacons," *Anal. Chem.*, vol. 75, no. 15, pp. 3697–3703, Aug. 2003, doi: 10.1021/AC034295L.

[224] H. Bui, S. Garg, V. Miao, T. Song, R. Mokhtar, and J. Reif, "Design and analysis of linear cascade DNA hybridization chain reactions using DNA hairpins," *New J. Phys.*, vol. 19, no. 1, p. 015006, Jan. 2017, doi: 10.1088/1367-2630/AA53D0.

[225] A. M. James, M. B. Baker, G. Bao, and C. D. Searles, "MicroRNA Detection Using a Double Molecular Beacon Approach: Distinguishing Between miRNA and Pre-miRNA," *Theranostics*, vol. 7, no. 3, p. 634, 2017, doi: 10.7150/THNO.16840.

[226] M. B. Baker, G. Bao, and C. D. Searles, "In vitro quantification of specific microRNA using molecular beacons," *Nucleic Acids Res.*, vol. 40, no. 2, pp. 1–12, 2012, doi: 10.1093/nar/gkr1016.

[227] Q. Liu *et al.*, "Quantitative Detection of miRNA-21 Expression in Tumor Cells and Tissues Based on Molecular Beacon," *Int. J. Anal. Chem.*, vol. 2018, 2018, doi:

10.1155/2018/3625823.

[228] K. Shahsavar, E. Shokri, and M. Hosseini, “A fluorescence-readout method for miRNA-155 detection with double-hairpin molecular beacon based on quadruplex DNA structure,” *Microchem. J.*, vol. 158, p. 105277, Nov. 2020, doi: 10.1016/J.MICROC.2020.105277.

[229] J. Zhou *et al.*, “High-throughput single-EV liquid biopsy: Rapid, simultaneous, and multiplexed detection of nucleic acids, proteins, and their combinations,” *Sci. Adv*, vol. 6, 2020, Accessed: Aug. 03, 2021. [Online]. Available: http://advances.sciencemag.org/.

[230] Y. Q *et al.*, “Monitoring microRNAs using a molecular beacon in CD133+/ CD338+ human lung adenocarcinoma-initiating A549 cells,” *Asian Pac. J. Cancer Prev.*, vol. 15, no. 1, pp. 161–166, 2014, doi: 10.7314/APJCP.2014.15.1.161.

[231] O. S. L. Gonçalves *et al.*, “Detection of miRNA cancer biomarkers using light activated Molecular Beacons,” *RSC Adv.*, vol. 9, no. 22, pp. 12766–12783, Apr. 2019, doi: 10.1039/C9RA00081J.

[232] T. U. Metcalf *et al.*, “Global analyses revealed age-related alterations in innate immune responses after stimulation of pathogen recognition receptors,” *Aging Cell*, vol. 14, no. 3, p. 421, Jun. 2015, doi: 10.1111/ACEL.12320.

[233] C. SC, U. K, C. W, W. W, K. WB, and M. T, “Age-related impaired proliferation of peripheral blood mononuclear cells is associated with an increase in both IL-10 and IL-12,” *Exp. Gerontol.*, vol. 34, no. 2, pp. 243–252, Apr. 1999, doi: 10.1016/S0531-5565(98)00064-3.

[234] R. K. Y. Wong, M. MacMahon, J. V. Woodside, and D. A. Simpson, “A comparison of RNA extraction and sequencing protocols for detection of small RNAs in plasma,” *BMC Genomics 2019 201*, vol. 20, no. 1, pp. 1–12, Jun. 2019, doi: 10.1186/S12864-019-5826-7.

[235] P. Natsidis, P. H. Schiffer, I. Salvador-Martínez, and M. J. Telford, “Computational discovery of hidden breaks in 28S ribosomal RNAs across eukaryotes and consequences for RNA Integrity Numbers,” *Sci. Reports 2019 91*, vol. 9, no. 1, pp. 1–10, Dec. 2019, doi: 10.1038/s41598-019-55573-1.

[236] L. Moldovan, K. E. Batte, J. Trgovcich, J. Wisler, C. B. Marsh, and M. Piper, "Methodological challenges in utilizing miRNAs as circulating biomarkers," *J. Cell. Mol. Med.*, vol. 18, no. 3, p. 371, Mar. 2014, doi: 10.1111/JCMM.12236.

[237] M. T. Dorak, "Data analysis and reporting," *Real-time PCR*, pp. 65–88, Jan. 2007, doi: 10.4324/9780203967317-11.

[238] M. Nurjayadi *et al.*, "Detection of Salmonella typhimurium on artificially contaminated milk by real time PCR using STM4497 and fljB primers," *AIP Conf. Proc.*, vol. 2331, no. 1, p. 040028, Apr. 2021, doi: 10.1063/5.0041892.

[239] L. Yan *et al.*, "miR-21-5p induces cell proliferation by targeting TGFBI in non-small cell lung cancer cells," *Exp. Ther. Med.*, vol. 16, no. 6, p. 4655, Dec. 2018, doi: 10.3892/ETM.2018.6752.

[240] S. Gu, Y. Lai, H. Chen, Y. Liu, and Z. Zhang, "miR-155 mediates arsenic trioxide resistance by activating Nrf2 and suppressing apoptosis in lung cancer cells," *Sci. Reports 2017 71*, vol. 7, no. 1, pp. 1–13, Sep. 2017, doi: 10.1038/s41598-017-06061-x.

[241] L. Lv, X. An, H. Li, and L. Ma, "Effect of miR-155 knockdown on the reversal of doxorubicin resistance in human lung cancer A549/dox cells," *Oncol. Lett.*, vol. 11, no. 2, pp. 1161–1166, Feb. 2016, doi: 10.3892/OL.2015.3995.

[242] L. Lei, Y. Huang, and W. Gong, "Inhibition of miR-92b suppresses nonsmall cell lung cancer cells growth and motility by targeting RECK," *Mol. Cell. Biochem.*, vol. 387, no. 1–2, pp. 171–176, Feb. 2014, doi: 10.1007/s11010-013-1882-5.

[243] M. L. Salem, S. Okba, S. Morad, N. El-Desoky, and A. F. Barakat, "Altered expression of miRNA-155 and miRNA-21 and higher numbers of T cells in the peripheral blood of early diagnosed lung cancer patients," *Int. J. Cancer Biomed. Res.*, vol. 4, no. 1, pp. 19–25, Apr. 2020, doi: 10.21608/JCBR.2020.21668.1009.

[244] S. A. Azimi *et al.*, "Ectopic Expression of miRNA-21 and miRNA-205 in Non-Small Cell Lung Cancer," *Int. J. Cancer Manag. 2019 121*, vol. 12, no. 1, Jan. 2019, doi: 10.5812/IJCM.85456.

[245] H. Otsu, M. Watanabe, N. Inoue, R. Masutani, and Y. Iwatani, "Intraindividual variation of microRNA expression levels in plasma and peripheral blood mononuclear cells and the associations of these levels with the pathogenesis of autoimmune thyroid diseases,"

Clin Chem Lab Med, 2017, doi: 10.1515/cclm-2016-0449.

[246] X. Y. Sun *et al.*, “Aberrant microRNA expression in peripheral plasma and mononuclear cells as specific blood-based biomarkers in schizophrenia patients,” *J. Clin. Neurosci.*, vol. 22, no. 3, pp. 570–574, Mar. 2015, doi: 10.1016/J.JOCN.2014.08.018.

[247] M. P. Hunter *et al.*, “Detection of microRNA Expression in Human Peripheral Blood Microvesicles,” *PLoS One*, vol. 3, no. 11, p. e3694, Nov. 2008, doi: 10.1371/JOURNAL.PONE.0003694.

[248] X. L. Zeng, S. Y. Zhang, J. F. Zheng, H. Yuan, and Y. Wang, “Altered miR-143 and miR-150 expressions in peripheral blood mononuclear cells for diagnosis of non-small cell lung cancer,” *Chin. Med. J. (Engl).*, vol. 126, no. 23, pp. 4510–4516, 2013, doi: 10.3760/CMA.J.ISSN.0366-6999.20122931.

[249] W. Jiao *et al.*, “Different miR-21-3p isoforms and their different features in colorectal cancer,” *Int. J. Cancer*, vol. 141, no. 10, pp. 2103–2111, Nov. 2017, doi: 10.1002/IJC.30902.

[250] H. SX, J. X, M. JL, and Z. Q, “Molecular beacons: a novel optical diagnostic tool.,” *Arch. Immunol. Ther. Exp. (Warsz).*, vol. 61, no. 2, pp. 139–148, Jan. 2013, doi: 10.1007/S00005-012-0209-7.

[251] C. A. G. Haasnoot *et al.*, “Structure, Kinetics and Thermodynamics of DNA Hairpin Fragments in Solution,” *J. Biomol. Struct. Dyn.*, vol. 1, no. 1, pp. 115–129, 1983, doi: 10.1080/07391102.1983.10507429.

[252] A. A. Lomzov, Y. N. Vorobjev, and D. V. Pyshnyi, “Evaluation of the Gibbs Free Energy Changes and Melting Temperatures of DNA/DNA Duplexes Using Hybridization Enthalpy Calculated by Molecular Dynamics Simulation,” *J. Phys. Chem. B*, vol. 119, no. 49, pp. 15221–15234, Dec. 2015, doi: 10.1021/ACS.JPCB.5B09645.

[253] J.-L. Mergny and L. Lacroix, “UV Melting of G-Quadruplexes,” *Curr. Protoc. Nucleic Acid Chem*, vol. 37, doi: 10.1002/0471142700.nc1701s37.

[254] M. Ghosh, K. V. R. Chary, N. V. Kumar, and U. Varshney, “Structural characterisation of a uracil containing hairpin DNA by NMR and molecular dynamics,” *Nucleic Acids Res.*, vol. 27, no. 19, pp. 3938–3944, Oct. 1999, doi: 10.1093/NAR/27.19.3938.

[255] P. W. Davis, W. Thurmes, and lgnacio Tinoco, “Structure of a small RNA hairpin,” *Nucleic Acids Res.*, vol. 21, no. 3, pp. 537–545, Feb. 1993, doi: 10.1093/NAR/21.3.537.

[256] S. Chirayil, Q. Wu, C. Amezcua, and K. J. Luebke, “NMR Characterization of an Oligonucleotide Model of the MiR-21 Pre-Element,” *PLoS One*, vol. 9, no. 9, Sep. 2014, doi: 10.1371/JOURNAL.PONE.0108231.

[257] V. Ramesh, “NMR evidence for the RNA stem-loop structure involved in the transcription attenuation of E. coli trp operon.,” *Nucleic Acids Res.*, vol. 21, no. 23, p. 5485, Nov. 1993, doi: 10.1093/NAR/21.23.5485.

[258] D. Bhattacharyya, G. M. Arachchilage, and S. Basu, “Metal Cations in G-Quadruplex Folding and Stability,” *Front. Chem.*, vol. 4, no. SEP, p. 38, 2016, doi: 10.3389/FCHEM.2016.00038.

[259] S. Tyagi, S. A. E. Marras, J. A. M. Vet, and fred russell Kramer, “Molecular Beacons: Hybridization Probes for Detection of Nucleic Acids in Homogeneous Solutions,” *Nonradioactive Anal. Biomol.*, pp. 606–616, 2000, doi: 10.1007/978-3-642-57206-7_53.

[260] S. Mao, Y. Ying, R. Wu, and A. K. Chen, “Recent Advances in the Molecular Beacon Technology for Live-Cell Single-Molecule Imaging,” *iScience*, vol. 23, no. 12, p. 101801, Dec. 2020, doi: 10.1016/J.ISCI.2020.101801.

CHAPTER 7 – Attachments

7. Attachments

7.1 Attachment 1 - CHUCB Ethics Committee approval for study (ref. 35/2019) to blood sample collection

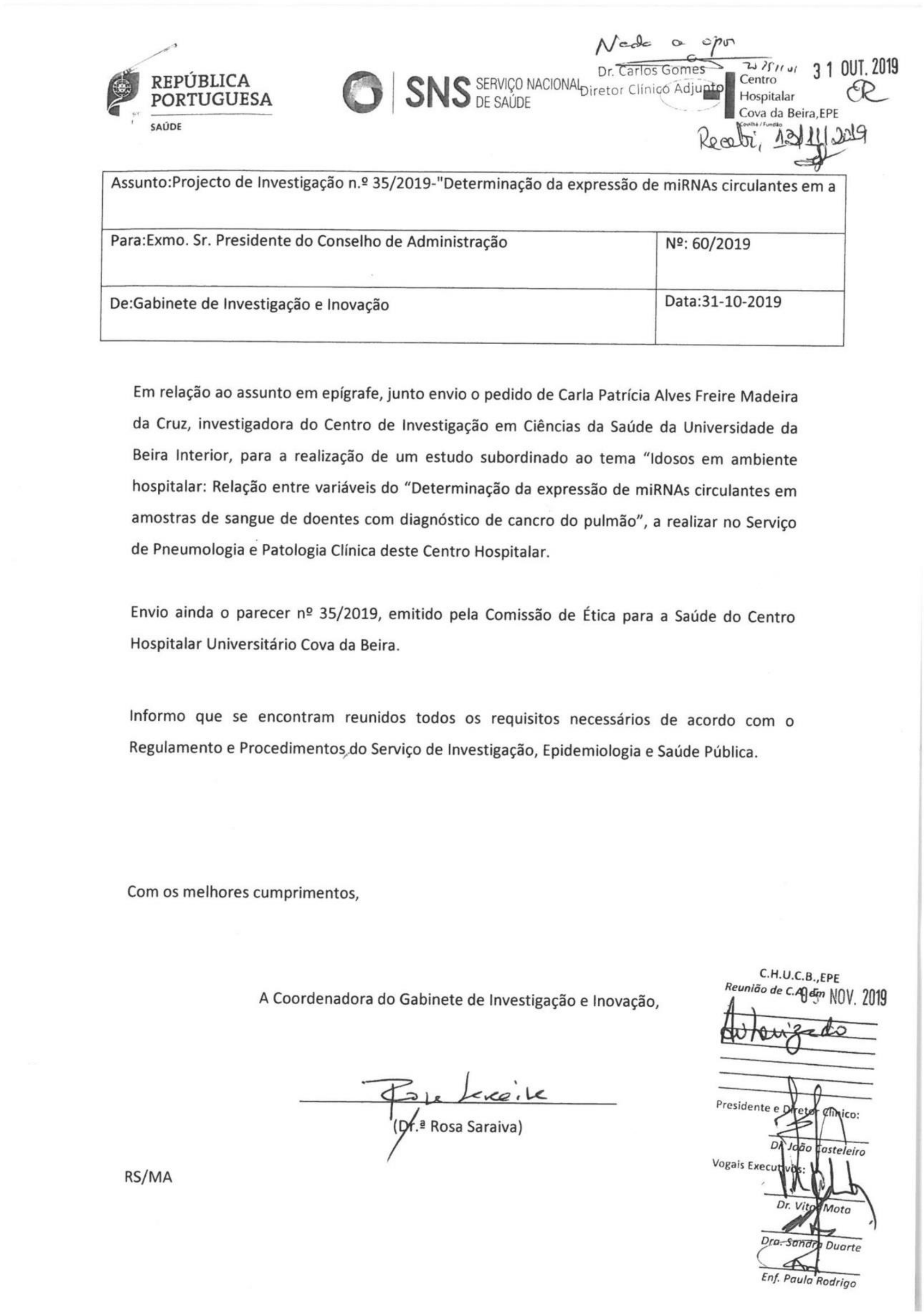

REPÚBLICA PORTUGUESA
SAÚDE

SNS SERVIÇO NACIONAL DE SAÚDE

Nada a opor
Dr. Carlos Gomes
Diretor Clínico Adjunto

31 OUT. 2019

Centro
Hospitalar
Cova da Beira, EPE
Covilhã / Fundão

Recebi, 13/11/2019

Assunto:Projecto de Investigação n.º 35/2019-"Determinação da expressão de miRNAs circulantes em a	
Para:Exmo. Sr. Presidente do Conselho de Administração	Nº: 60/2019
De:Gabinete de Investigação e Inovação	Data:31-10-2019

Em relação ao assunto em epígrafe, junto envio o pedido de Carla Patrícia Alves Freire Madeira da Cruz, investigadora do Centro de Investigação em Ciências da Saúde da Universidade da Beira Interior, para a realização de um estudo subordinado ao tema "Idosos em ambiente hospitalar: Relação entre variáveis do "Determinação da expressão de miRNAs circulantes em amostras de sangue de doentes com diagnóstico de cancro do pulmão", a realizar no Serviço de Pneumologia e Patologia Clínica deste Centro Hospitalar.

Envio ainda o parecer nº 35/2019, emitido pela Comissão de Ética para a Saúde do Centro Hospitalar Universitário Cova da Beira.

Informo que se encontram reunidos todos os requisitos necessários de acordo com o Regulamento e Procedimentos do Serviço de Investigação, Epidemiologia e Saúde Pública.

Com os melhores cumprimentos,

A Coordenadora do Gabinete de Investigação e Inovação,

(Dr.ª Rosa Saraiva)

RS/MA

C.H.U.C.B.,EPE
Reunião de C.A. em 05 NOV. 2019
Autorizado

Presidente e Diretor Clínico:
Dr. João Casteleiro
Vogais Executivos:
Dr. Vitor Moto
Dra. Sandra Duarte
Enf. Paula Rodrigo

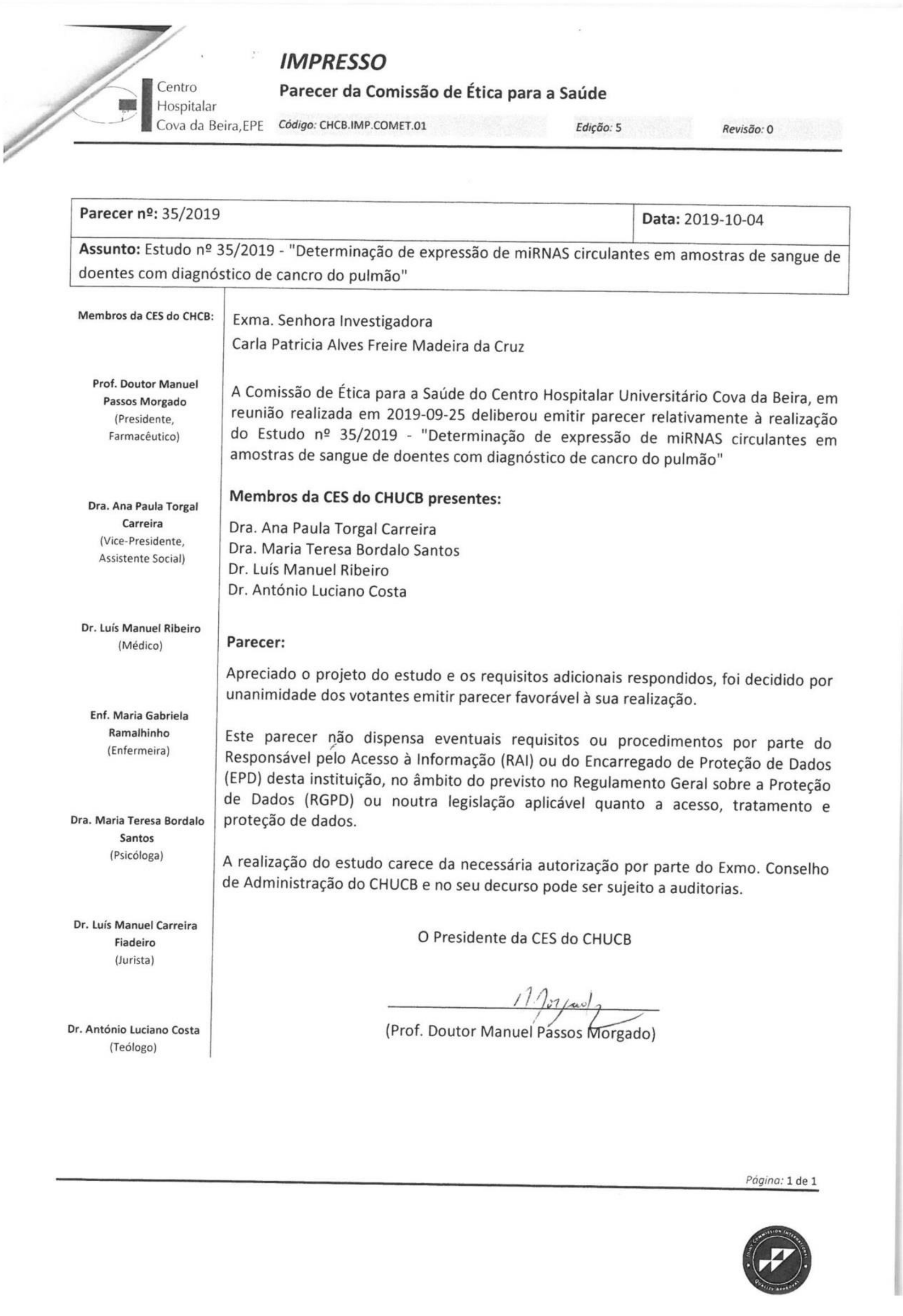

Centro
Hospitalar
Cova da Beira,EPE

IMPRESSO

Parecer da Comissão de Ética para a Saúde

Código: CHCB.IMP.COMET.01 *Edição:* 5 *Revisão:* 0

Parecer nº: 35/2019	**Data:** 2019-10-04
Assunto: Estudo nº 35/2019 - "Determinação de expressão de miRNAS circulantes em amostras de sangue de doentes com diagnóstico de cancro do pulmão"	

Exma. Senhora Investigadora
Carla Patricia Alves Freire Madeira da Cruz

A Comissão de Ética para a Saúde do Centro Hospitalar Universitário Cova da Beira, em reunião realizada em 2019-09-25 deliberou emitir parecer relativamente à realização do Estudo nº 35/2019 - "Determinação de expressão de miRNAS circulantes em amostras de sangue de doentes com diagnóstico de cancro do pulmão"

Membros da CES do CHUCB presentes:

Dra. Ana Paula Torgal Carreira
Dra. Maria Teresa Bordalo Santos
Dr. Luís Manuel Ribeiro
Dr. António Luciano Costa

Parecer:

Apreciado o projeto do estudo e os requisitos adicionais respondidos, foi decidido por unanimidade dos votantes emitir parecer favorável à sua realização.

Este parecer não dispensa eventuais requisitos ou procedimentos por parte do Responsável pelo Acesso à Informação (RAI) ou do Encarregado de Proteção de Dados (EPD) desta instituição, no âmbito do previsto no Regulamento Geral sobre a Proteção de Dados (RGPD) ou noutra legislação aplicável quanto a acesso, tratamento e proteção de dados.

A realização do estudo carece da necessária autorização por parte do Exmo. Conselho de Administração do CHUCB e no seu decurso pode ser sujeito a auditorias.

O Presidente da CES do CHUCB

(Prof. Doutor Manuel Passos Morgado)

Membros da CES do CHCB:

Prof. Doutor Manuel Passos Morgado
(Presidente, Farmacêutico)

Dra. Ana Paula Torgal Carreira
(Vice-Presidente, Assistente Social)

Dr. Luís Manuel Ribeiro
(Médico)

Enf. Maria Gabriela Ramalhinho
(Enfermeira)

Dra. Maria Teresa Bordalo Santos
(Psicóloga)

Dr. Luís Manuel Carreira Fiadeiro
(Jurista)

Dr. António Luciano Costa
(Teólogo)

Página: 1 de 1

7.2 Attachment 2 - XVI Annual CICS-UBI Symposium 2021 (Short communication)

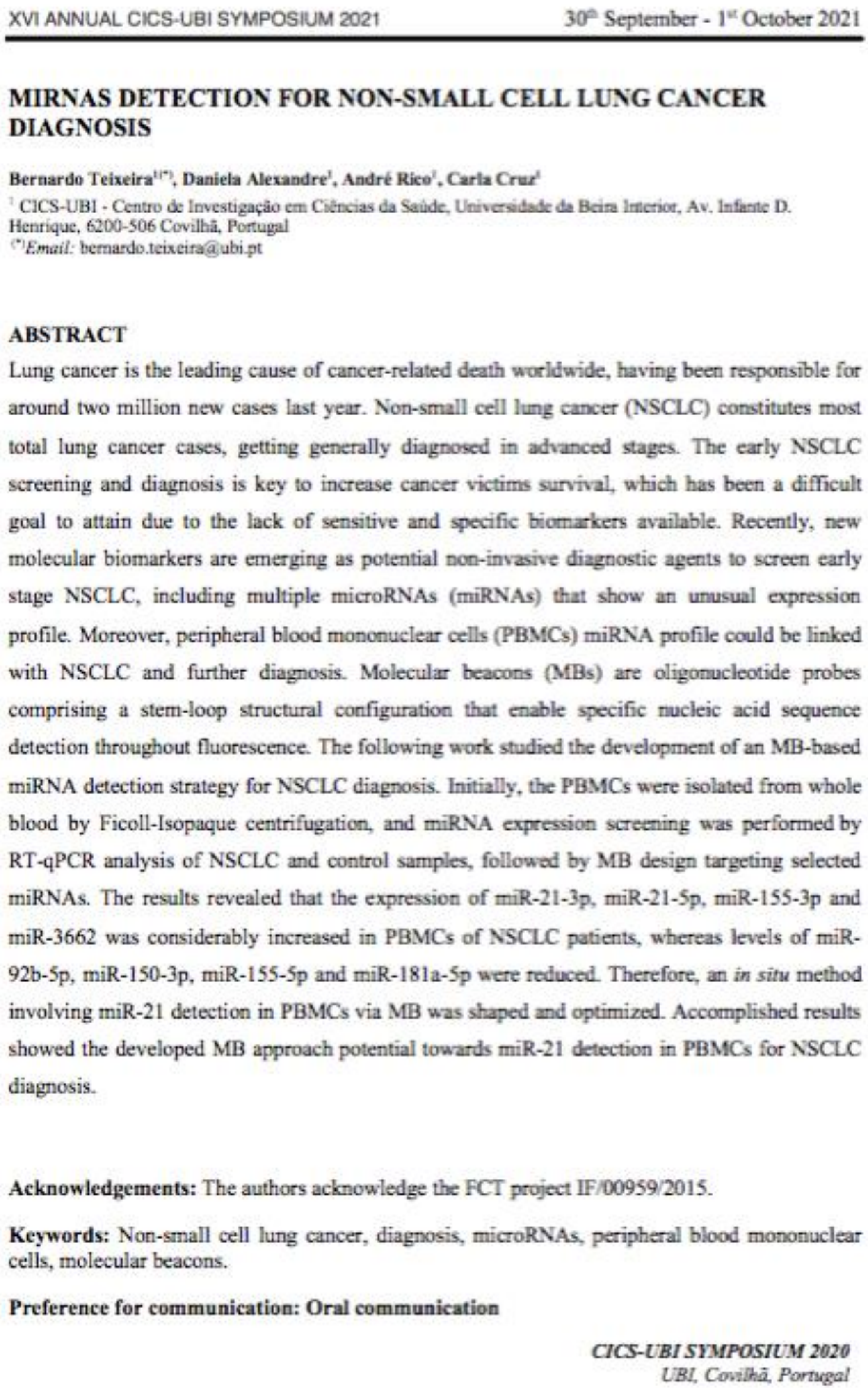

XVI ANNUAL CICS-UBI SYMPOSIUM 2021 30th September - 1st October 2021

MIRNAS DETECTION FOR NON-SMALL CELL LUNG CANCER DIAGNOSIS

Bernardo Teixeira[1(*)], Daniela Alexandre[1], André Rico[1], Carla Cruz[1]

[1] CICS-UBI - Centro de Investigação em Ciências da Saúde, Universidade da Beira Interior, Av. Infante D. Henrique, 6200-506 Covilhã, Portugal
(*)*Email:* bernardo.teixeira@ubi.pt

ABSTRACT

Lung cancer is the leading cause of cancer-related death worldwide, having been responsible for around two million new cases last year. Non-small cell lung cancer (NSCLC) constitutes most total lung cancer cases, getting generally diagnosed in advanced stages. The early NSCLC screening and diagnosis is key to increase cancer victims survival, which has been a difficult goal to attain due to the lack of sensitive and specific biomarkers available. Recently, new molecular biomarkers are emerging as potential non-invasive diagnostic agents to screen early stage NSCLC, including multiple microRNAs (miRNAs) that show an unusual expression profile. Moreover, peripheral blood mononuclear cells (PBMCs) miRNA profile could be linked with NSCLC and further diagnosis. Molecular beacons (MBs) are oligonucleotide probes comprising a stem-loop structural configuration that enable specific nucleic acid sequence detection throughout fluorescence. The following work studied the development of an MB-based miRNA detection strategy for NSCLC diagnosis. Initially, the PBMCs were isolated from whole blood by Ficoll-Isopaque centrifugation, and miRNA expression screening was performed by RT-qPCR analysis of NSCLC and control samples, followed by MB design targeting selected miRNAs. The results revealed that the expression of miR-21-3p, miR-21-5p, miR-155-3p and miR-3662 was considerably increased in PBMCs of NSCLC patients, whereas levels of miR-92b-5p, miR-150-3p, miR-155-5p and miR-181a-5p were reduced. Therefore, an *in situ* method involving miR-21 detection in PBMCs via MB was shaped and optimized. Accomplished results showed the developed MB approach potential towards miR-21 detection in PBMCs for NSCLC diagnosis.

Acknowledgements: The authors acknowledge the FCT project IF/00959/2015.

Keywords: Non-small cell lung cancer, diagnosis, microRNAs, peripheral blood mononuclear cells, molecular beacons.

Preference for communication: Oral communication